Title
SEARCH FOR RIGHT-HANDED CURRENTS BY MEANS OF MUON SPIN ROTATION

Author
Stoker, D.P.

Publication Date
1985-09-01

Lawrence Berkeley Laboratory
UNIVERSITY OF CALIFORNIA
Physics Division

SEARCH FOR RIGHT-HANDED CURRENTS BY MEANS OF MUON SPIN ROTATION

D.P. Stoker
(Ph.D. Thesis)

September 1985

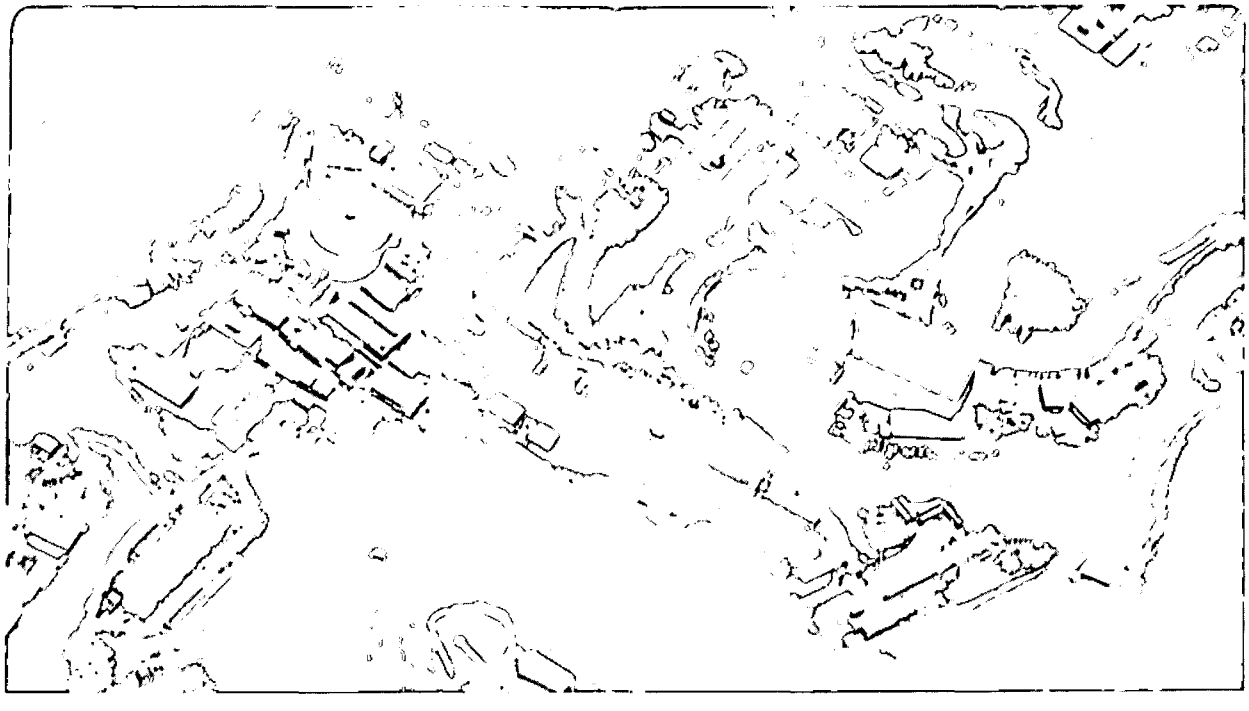

Prepared for the U.S. Department of Energy under Contract DE-AC03-76SF00098

DISCLAIMER

LBL-20324

Search for Right-Handed Currents by Means of Muon Spin Rotation

David Philip Stoker

Ph.D. Thesis

Lawrence Berkeley Laboratory
University of California
Berkeley, California 94720

September 1985

Search for Right-Handed Currents by Means of Muon Spin Rotation

David Philip Stoker

Abstract

A muon spin rotation (μSR) technique has been used to place limits on right-handed weak currents in μ^+ decay. A beam of almost 100% polarized 'surface' muons obtained from the TRIUMF M13 beamline was stopped in essentially non-depolarizing >99.99% pure metal foils. The μ^+ spins were precessed by 70-G or 110-G transverse fields. Decay e^+ emitted within 225 mrad of the beam direction and with momenta above 46 MeV/c were momentum-analyzed to 0.2%. Comparison of the μSR signal amplitude with that expected for (V-A) decay yields an endpoint asymmetry $\xi P_\mu \delta/\rho > 0.9951$ with 90% confidence. In the context of manifest left-right symmetric models with massless neutrinos the results imply the 90% confidence limits $M(W_2) > 381$ GeV/c^2 and $-0.057 < \zeta < 0.044$, where W_2 is a predominantly right-handed gauge boson and ζ is the left-right mixing angle. Limits on $M(W_2)$ for $M(\nu_{\mu R}) \neq 0$ are also presented. The endpoint asymmetry is used to deduce limits on the $\nu_{\mu L}$ mass and helicity in π^+ decay, non-(V-A) couplings in helicity projection form, and the mass scale of composite leptons.

Table of Contents

Acknowledgments

This thesis owes much to the efforts of the other collaboration members participating in TRIUMF experiments E185 and E247: Brian Balke, John Carr, George Gidal, Bruno Gobbi, Alex Jodidio, Chris Oram, Kirk Shinsky (deceased), Herb Steiner, Mark Strovink, and Bob Tripp. The technical assistance of C. Covey, R. Fuzesy, F. Goozen, P.Harding, M. Morrison, and P. Robrish at L.B.L. and the support of the TRIUMF staff contributed to the success of the experiments.

I would particularly like to thank my advisor Mark Strovink, who having advised me initially that a thesis could be completed in $2+\varepsilon$ years, continued to provide patient support and advice as ε grew to 2.7.

I would also like to thank Marjorie Olmstead for helpful discussions of relevant aspects of solid state physics.

The assistance of Pat Bronnenberg in typing much of this thesis and other material is greatly appreciated.

The research reported here was supported in part by the U.S. Department of Energy through Contracts No. DE-AC03-76SF00098 and AC02-ER02289.

Chapter 1

Introduction

In the course of more than a decade of remarkable agreement with experiment the Glashow-Weinberg-Salam model[1-3], based on the gauge group $SU(2)_L \times U(1)$, has become accepted as the 'standard model' of electroweak interactions. Despite its outstanding success the standard model does not explain the left-handed character of the charged current weak interactions such as β and μ decay. Instead the left-handedness is built in a priori by allowing only the left-handed components of fermions to couple to the charged gauge bosons. Shortly before Weinberg and Salam unified the weak and electromagnetic interactions, Lipmanov[4] asked

> "...whether the nonconservation of parity in weak interactions is not a manifestation of a violated (V±A) symmetry of these interactions, with (V-A) dominance... It is possible that the coupling between the weak interaction currents is mediated by intermediate vector bosons. Then one can imagine that there exist intermediate bosons of two kinds, $W^{(V-A)}$ and $W^{(V+A)}$, which mediate the (V-A) and (V+A) couplings, respectively. If the mass of the $W^{(V-A)}$ and $W^{(V+A)}$ were equal, there would be no experimental manifestation of parity non-conservation. However, the latter effect appears if there is a mass difference for the two intermediate bosons. The effective current-current Lagrangian for the weak interactions... has the form (for $q^2 << M^2$):

$$L_W = (G/\sqrt{2}) J^{(V-A)} J^{(V-A)*} + (G_1/\sqrt{2}) J^{(V+A)} J^{(V+A)*}$$

where $G/\sqrt{2} = 4\pi g^2/M^2_{(V-A)}$, $G_1/\sqrt{2} = 4\pi g^2/M^2_{(V+A)}$ "

Lipmanov went on to show that the electron emission asymmetry in muon decay provided an estimate $G_1 \leq 0.12G$, and that the μ^+ from π^+ decay would be partially depolarized, with longitudinal polarization $P_\mu = 1-2G_1^2/G^2$.

The more recent left-right symmetric theories[5,6], in which the standard electroweak gauge group is extended to $SU(2)_L \times SU(2)_R \times U(1)$, embody the spirit of the Lipmanov formulation. Although completely left-right symmetric at the Lagrangian level these theories admit asymmetric solutions through spontaneous symmetry breaking which violate parity[7]. In particular, the Higgs mechanism can impart a larger mass to W_R than to W_L, thereby suppressing the right-handed currents at low q^2 while retaining parity conservation for $q^2 >> M^2(W_R)$.

This thesis presents the results of a search for deviations from the (V-A) prediction for the e^+ asymmetry in polarized μ^+ decay at rest by means of a muon spin rotation (μSR) technique. The recent development[8] of 'surface' beams has provided muon beams with essentially the polarization intrinsic to pion decay at rest. Naturally, right-handed currents may contribute at each step of the $\pi \rightarrow \mu \rightarrow e$ decay chain thus enhancing the experimental sensitivity.

The experiment was operated in two modes, each sensitive to right-handed currents but with different major sources of possible systematic error. In each case the μ^+ beam was stopped in metal targets. In metals, unlike many other materials, the μ^+ are thermalized in a quasi-free state instead of as muonium (μ^+e^-) where hyperfine transitions rapidly reduce the muon polarization by 50%. In the first

mode[9] the spins of the stopped μ^+ were held in a 1.1-T field which quenches muon depolarization in any residual muonium through the Paschen-Back effect. Measurement of the momentum spectrum endpoint decay rate opposite to the μ^+ spin, which vanishes for a purely (V-A) interaction, allows limits to be set on any right-handed current admixture. In the second mode, which provided the data presented here, the μ^+ spins were instead precessed by 70-G or 110-G fields transverse to the beam direction. The time variation of the e^+ emission rate near the beam direction as the μ^+ spins precess constitute the μSR signal. Limits on right-handed currents are set by comparing the μSR signal amplitude with that expected for a (V-A) interaction.

The experiment was conceived in mid-1980 and most of the apparatus was constructed during 1981. The data presented in this thesis was accumulated during the three running periods of experiments E185 and E247 at the TRIUMF cyclotron during 1982-4.

Chapter 2

The Standard and Left-Right Symmetric Models

2.1 The Standard Model: A Brief Review

The gauge group of the standard electroweak model is $SU(2)_L \times U(1)_Y$ with coupling constants g and g' respectively. The leptons and quark weak eigenstates are assigned to left-handed SU(2) doublets

$$\begin{bmatrix}\nu_e\\ e^-\end{bmatrix}_L, \begin{bmatrix}\nu_\mu\\ \mu^-\end{bmatrix}_L, \ldots \qquad \begin{bmatrix}u\\ d'\end{bmatrix}_L, \begin{bmatrix}c\\ s'\end{bmatrix}_L, \ldots$$

and right-handed singlets.

The simplest Higgs assignment required to break down the symmetry to $U(1)_{em}$, thereby guaranteeing the masslessness of the photon, is the scalar $SU(2)_L$ doublet

$$\Phi = \begin{bmatrix}\phi^+\\ \phi^o\end{bmatrix}$$

Minimizing the Higgs potential yields a non-zero vacuum expectation value solution

$$\Phi = \begin{bmatrix}0\\ v\end{bmatrix}$$

which imparts masses to the W and Z bosons and the fermions. With the Weinberg angle θ_W defined by $\tan\theta_W = g'/g$ the gauge fields $\vec{W}=(W^1,W^2,W^3)$ and B, associated with $SU(2)_L$ and $U(1)_Y$ respectively, become the physical boson eigenstates

$$W^\pm = (W^1 \mp iW^2)/\sqrt{2} \qquad M_W^2 = g^2v^2/2$$

$$Z = W^3\cos\theta_W - B\sin\theta_W \qquad M_Z^2 = (g^2+g'^2)v^2/2$$

$$\gamma = W^3\sin\theta_W + B\cos\theta_W \qquad M_\gamma = 0$$

Comparison of single W exchange in the low-energy limit with the corresponding four-fermion contact interaction gives $g^2/8M_W^2 = G_F/\sqrt{2}$ where G_F is the Fermi coupling constant. In addition, the form of the electromagnetic current allows the electronic charge $e = \sqrt{(4\pi\alpha)}$ to be related to g and g' by $e = g\sin\theta_W = g'\cos\theta_W$. Then to lowest order and ignoring radiative corrections the standard model predicts

$$M_W = \frac{1}{\sin\theta_W}\left[\frac{\pi\alpha}{G_F\sqrt{2}}\right]^{1/2} = \frac{37.3}{\sin\theta_W}\ \text{GeV}$$

and

$$M_Z = \frac{M_W}{\cos\theta_W} = \frac{74.6}{\cos 2\theta_W}\ \text{GeV}$$

Table (2.1) shows the experimental masses from the UA-1[10] and UA-2[11] collaborations at CERN together with the standard model predictions of Marciano and Sirlin[12]. The theoretical predictions use $\sin^2\theta_W$=0.217±0.014 obtained from deep inelastic ν_μ scattering and the e-D scattering asymmetry after applying radiative corrections.

	UA-1	UA-2	Standard Model
M_W (GeV)	80.9±1.5±2.4	81.0±2.5±1.3	$83.0^{+2.9}_{-2.7}$
M_Z (GeV)	95.6±1.5±2.9	91.9±1.3±1.4	$93.8^{+2.4}_{-2.2}$

Table (2.1)

The minimal standard model has one as yet unobserved physical

neutral scalar Higgs with a mass M_H not predicted by the theory. However, stability of the physical vacuum requires $M_H > 7$ GeV and the weak interactions are predicted to become strong at high energies unless $M_H < 1$ TeV.

2.2 Left-Right Symmetric Model: An Introduction

The gauge group of left-right symmetric models is $SU(2)_L \times SU(2)_R \times U(1)_{B-L}$ with coupling constants g_L, g_R, and g' respectively. Only manifest left-right symmetric models, for which $g_L = g_R = g$, are considered here. Compared to the standard model, the left-right symmetric model requires an extra set of gauge bosons and a more complex Higgs structure to produce the fermion and gauge boson masses. The left- and right-handed fermion components are assigned to isospin doublets $\psi_{L,R}$ with the indicated quantum numbers $(T_L, T_R, B\text{-}L)$:

$$\begin{bmatrix}\nu_e\\ e^-\end{bmatrix}_L, \begin{bmatrix}\nu_\mu\\ \mu^-\end{bmatrix}_L, \ldots \quad \begin{bmatrix}\nu_e\\ e^-\end{bmatrix}_R, \begin{bmatrix}\nu_\mu\\ \mu^-\end{bmatrix}_R, \ldots \quad \begin{bmatrix}u\\ d'\end{bmatrix}_L, \begin{bmatrix}c\\ s'\end{bmatrix}_L, \ldots \quad \begin{bmatrix}u\\ d'\end{bmatrix}_R, \begin{bmatrix}c\\ s'\end{bmatrix}_R, \ldots$$

$$(1/2,0,-1) \qquad (0,1/2,-1) \qquad (1/2,0,1/3) \qquad (0,1/2,1/3)$$

The generation of Dirac masses, $\propto(\psi_R\psi_L + \psi_L\psi_R)$, for the fermions requires Yukawa couplings to Higgs multiplets with quantum numbers $(1/2,1/2^*,0)$ since the mass terms in the Lagrangian must be Lorentz scalars. The required multiplets of complex scalar fields are

$$\Phi = \begin{bmatrix}\phi_1^0 & \phi_1^+\\ \phi_2^- & \phi_2^0\end{bmatrix} \qquad \tilde{\Phi} \equiv \tau_2 \Phi^* \tau_2$$

Additional Higgs multiplets are needed to complete the symmetry breakdown to $U(1)_{em}$. The simplest choice is the doublets

$$X_L = \begin{bmatrix} X_L^+ \\ X_L^o \end{bmatrix} \qquad X_R = \begin{bmatrix} X_R^+ \\ X_R^o \end{bmatrix}$$

with quantum numbers (1/2,0,1) and (0,1/2,1) respectively. Although the classical Higgs potential is symmetric under $X_L \leftrightarrow X_R$, Senjanovic[13] has shown that for a range of coefficients an asymmetric solution

$$\langle X_L \rangle = 0, \qquad \langle X_R \rangle = \begin{bmatrix} 0 \\ v \end{bmatrix}, \qquad \langle \Phi \rangle = \begin{bmatrix} k & 0 \\ 0 & k' \end{bmatrix}$$

emerges as the absolute minimum of the potential.

The gauge fields $\vec{W}_L$, $\vec{W}_R$, and B associated with $SU(2)_L$, $SU(2)_R$, and $U(1)_{B-L}$ respectively, combine to form the mass eigenstates $W_1^{\pm}$, $W_2^{\pm}$, Z_1, Z_2 and γ. In general, the Higgs mechanism which gives masses to the gauge bosons also produces a left-right mixing. The physical charged bosons are

$$\begin{bmatrix} W_1 \\ W_2 \end{bmatrix}^{\pm} = \begin{bmatrix} \cos\zeta & \sin\zeta \\ -\sin\zeta & \cos\zeta \end{bmatrix} \begin{bmatrix} W_L \\ W_R \end{bmatrix}^{\pm}$$

where $W_{L,R}^{\pm} = (W_{L,R}^1 \mp i W_{L,R}^2)/\sqrt{2}$ and $\tan 2\zeta = -4kk'/v^2$. The experimental constraints that ζ is small and $M(W_2) >> M(W_1)$ [section (2.5)] imply $v >> k,k'$, and then

$$M^2(W_1) \approx g^2(k^2+k'^2)/2$$

$$M^2(W_2) \approx g^2(v^2+k^2+k'^2)/2$$

With θ_W', the analog of the Weinberg angle, defined by $\sin^2\theta_W' = g'^2/(g^2+g'^2)$ the physical neutral bosons are

$$\gamma = (W_L^3 + W_R^3)\sin\theta_W' + B\sqrt{(\cos 2\theta_W')}$$

$$Z_1 \approx W_L^3\cos\theta_W' - W_R^3\sin\theta_W'\tan\theta_W' - B\tan\theta_W'\sqrt{(\cos 2\theta_W')}$$

$$Z_2 \approx W_R^3\sqrt{(\cos 2\theta_W')}/\cos\theta_W' - B\tan\theta_W'$$

with masses $M(\gamma) = 0$

$$M(Z_1) \approx M(W_1)/\cos\theta_W'$$

$$M(Z_2) \approx M(W_2)\cos\theta_W'/\sqrt{(\cos 2\theta_W')}$$

In addition, for the above choice of Higgs multiplets, there remain six neutral and four charged physical Higgs scalars. In the model of Senjanovic[13] one neutral Higgs has a mass $\sim(M(W_1))$ and the rest have masses $\sim(M(W_2))$.

In the limit $M(W_2) \to \infty$ the predictions of the left-right symmetric model are identical to those of the standard model for both the charged and neutral currents. Also, in the limit $\zeta \to 0$ but with $M(W_2)$ finite both models make identical predictions for the parity violating neutral currents.

2.3 Neutrinos: Dirac or Majorana?

The ν_L of the standard electroweak model may be either Dirac or Majorana particles. In the Dirac case ν_L and ν_R are different helicity states of the same particle, and ν_R is assigned to an SU(2) singlet. However, for Majorana neutrinos ν_L and ν_R are different particles, and ν_R is absent from the standard model.

The situation is more complex in the left-right symmetric model where, depending on the choice of Higgs structure, the neutrinos may

acquire both Majorana and Dirac masses. As will be seen below this provides an explanation, first proposed by Gell-Mann, Ramond and Slansky[14], for the smallness of the ν_L mass. It also has a major impact on the observability of right-handed currents in low-energy processes [section (2.4)].

The Dirac and Majorana mass terms have the structures and $(T_L, T_R, B-L)$ quantum numbers:

Dirac:	$(\bar{\nu}_R \nu_L + \bar{\nu}_L \nu_R)$	(1/2,1/2,0)
Majorana:	$(\bar{\nu}^c_L \nu_L + \bar{\nu}_L \nu^c_L)$ and $(\bar{\nu}^c_R \nu_R + \bar{\nu}_R \nu^c_R)$	(1,0,-2) and (0,1,-2)

Only Dirac mass terms, through Yukawa couplings to the multiplet Φ, are possible for the Higgs assignment of section (2.2).

Mohapatra and Senjanovic[15] have proposed a model in which two Majorana neutrinos ν and N are assigned to the lepton doublets

$$\begin{bmatrix} \nu_{eL} \\ e^-_L \end{bmatrix}, \ldots \qquad \begin{bmatrix} N_{eR} \\ e^-_R \end{bmatrix}, \ldots$$

prior to spontaneous symmetry breaking, and the Higgs multiplets $X_{L,R}$ are replaced by $\Delta_L(1,0,2)$ and $\Delta_R(0,1,2)$ which generate the additional Majorana mass terms. The new Higgs structure is somewhat more complicated with

$$\Delta_{L,R} = \begin{bmatrix} \delta^+/\sqrt{2} & \delta^{++} \\ \delta^0 & -\delta^+/\sqrt{2} \end{bmatrix}_{L,R}$$

With an analogous pattern of vacuum expectation values, $\langle \Delta_L \rangle = 0$ and

$\langle\Delta_R^0\rangle=v$, the Majorana mass term for ν_L vanishes while that for N_R is $\sim M(W_2)$. The off-diagonal Dirac mass terms ($\sim M_\ell$ for $\ell=e,\mu,\tau$) cause a slight left-right mixing so that the mass eigenstates ν_1 and ν_2 are

$$\begin{bmatrix}\nu_1\\ \nu_2\end{bmatrix} = \begin{bmatrix}\cos\delta & \sin\delta\\ -\sin\delta & \cos\delta\end{bmatrix}\begin{bmatrix}\nu_L\\ N_R\end{bmatrix}$$

with masses $$M(\nu_{\ell_1}) \approx M_\ell^2/M(W_2)$$

$$M(\nu_{\ell_2}) \approx M(W_2)$$

and mixing angle $$\delta \sim M_\ell/M(W_2)$$

Here the small mass of the predominantly left-handed neutrino ν_1 is clearly related to the suppression of the right-handed currents through the asymmetric vacuum expectation values $\langle\Delta_L\rangle=0$ and $\langle\Delta_R^0\rangle=v$.

2.4 The Low-Energy Hamiltonian

In the case of Dirac neutrinos $m(\nu_R)=m(\nu_L)$, which is known experimentally to be small. The effective low-energy Hamiltonian for charged current processes is then

$$H_{eff} = \frac{g^2}{2M^2(W_1)}\{J_LJ_L^\dagger(\cos^2\zeta + \varepsilon\sin^2\zeta) - J_RJ_R^\dagger(\sin^2\zeta + \varepsilon\cos^2\zeta) + (J_LJ_L^\dagger + J_RJ_L^\dagger)(1-\varepsilon)\sin\zeta\cos\zeta\} \tag{2.1}$$

where the mass-squared ratio $\varepsilon \equiv M^2(W_1)/M^2(W_2)$ and the left-right mixing angle ζ are small. Retaining only the leading order terms

$$H_{eff} \approx \frac{g^2}{2M^2(W_1)}\{J_LJ_L^\dagger + \varepsilon J_RJ_R^\dagger + \zeta(J_LJ_R^\dagger + J_RJ_L^\dagger)\}$$

In the Majorana case described in section (2.3) the predominantly right-handed ν_2 is too massive to be produced in low-energy processes. The effective Hamiltonian is now different for leptonic and semileptonic processes since right-handed currents are suppressed by a factor of $\sin\delta$ at the leptonic vertices:

Semileptonic:

$$H_{eff} = \frac{g^2}{2M^2(W_1)} \{J_L J_L^\dagger \cos\delta(\cos^2\zeta + \varepsilon\sin^2\zeta) - J_R J_R^\dagger \sin\delta(\sin^2\zeta + \varepsilon\cos^2\zeta) + (J_R J_L^\dagger \cos\delta - J_L J_R^\dagger \sin\delta)(1-\varepsilon)\sin\zeta\cos\zeta\}$$

Leptonic:

$$H_{eff} = \frac{g^2}{2M^2(W_1)} \{J_L J_L^\dagger \cos^2\delta(\cos^2\zeta + \varepsilon\sin^2\zeta) + J_R J_R^\dagger \sin^2\delta(\sin^2\zeta + \varepsilon\cos^2\zeta) - (J_R J_L^\dagger + J_L J_R^\dagger)(1-\varepsilon)\sin\delta\cos\delta\sin\zeta\cos\zeta\}$$

Then to leading order in ε and ζ, but neglecting terms in δ:

Semileptonic: $$H_{eff} \approx \frac{g^2}{2M^2(W_1)} \{J_L J_L^\dagger + \zeta J_R J_R^\dagger\}$$

where the right-handed current is purely hadronic.

Leptonic: $$H_{eff} \approx \frac{g^2}{2M^2(W_1)} J_L J_L^\dagger$$

Thus if the ν_2 are sufficiently massive, purely leptonic low-energy processes such as muon decay give no information on ε and ζ regardless of $M(W_2)$, while semileptonic processes still yield information on ζ. The non-leptonic low-energy Hamiltonian is unchanged from equation (2.1).

2.5 Limits on Right-Handed Currents

The already exisitng experimental 90% confidence limits on the mass-squared ratio ε and the mixing angle ζ are displayed in Figure (2.1). The allowed regions are those which include $\varepsilon=\zeta=0$, i.e. the (V-A) limit. Only the limits from the y distributions in νN and $\bar{\nu}N$ scattering (double lines, Ref. 16) are valid irrespective of the ν_R mass. The other limits assume massless or very light ν_R. Muon decay contours are derived from decay-rate measurements opposite the μ^+ spin direction at the spectrum endpoint (bold curve, spin-held data from the present experiment, Ref. 9); the product of the asymmetry parameter and the μ^+ polarization, ξP_μ (dotted curve, Ref. 17); and the Michel parameter ρ (solid curve, Ref. 18). Nuclear β decay contours are obtained from the Gamow-Teller β polarization (dot-dashed curves, Ref. 19); the comparison of Gamow-Teller and Fermi β polarizations (long-dashed curves, Ref. 20); and the ^{19}Ne asymmetry A(0) and ft ratio, with the assumption of conserved vector current (short-dashed curves, Refs. 21 and 22).

Additional model dependent limits, independent of the ν_R mass but assuming the same left- and right-handed quark mixing angles, are set by semileptonic decays[23] $[|\zeta|(1-\varepsilon)<0.005]$, current algebra analysis of non-leptonic $\Delta S=1$ weak decays[24] $[|\zeta|(1-\varepsilon)<0.004$, and $M(W_2)>300$ GeV if $\zeta=0]$, and the K_L-K_S mass difference[25,26] $[M(W_2)>1.6$ TeV]. Without the quark mixing angle assumption the K_L-K_S mass difference provides a general limit[27] $M(W_2)>300$ GeV.

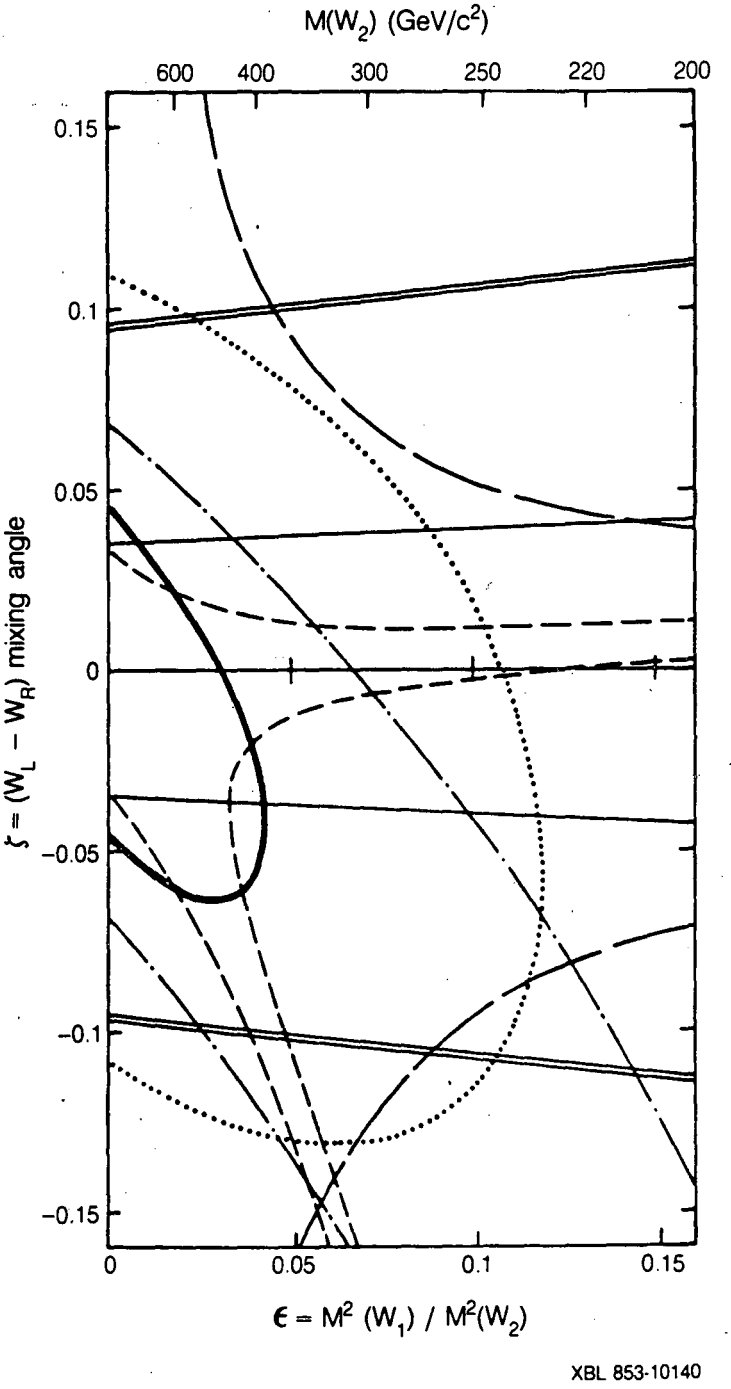

FIGURE (2.1). Experimental 90% confidence limits on the $W_{1,2}$ mass-squared ratio ε and the left-right mixing angle ζ. The allowed regions are those which include $\varepsilon=\zeta=0$. The sources of the limits are described in the text.

Chapter 3

Muon Decay

3.1 Four-Fermion Contact Interaction

The muon differential decay rate for an interaction mediated by a heavy vector boson, W, differs from that for the corresponding four-fermion contact interaction by terms[28] of order $(m_\mu/M_W)^2$. These terms are $\sim 10^{-6}$ for $M_W \approx 80$ GeV/c^2 and are negligible at the present level of experimental precision. Consequently it is legitimate to treat muon decay as a contact interaction.

The μ^+ decay probability, integrated over e^+ spin directions, for the most general four-fermion contact interaction with massless neutrinos and in the absence of radiative corrections is[29,30]

$$\frac{d^2\Gamma}{dx\,d(\cos\theta)} \propto (x^2-x_o^2)^{1/2}\{9x(1-x) + 2\rho(4x^2-3x-x_o^2) + 9\eta x_o(1-x) + \xi\cos\theta(x^2-x_o^2)^{1/2}[3(1-x) + 2\delta(4x-3-m_e x_o/m_\mu)]\} \tag{3.1}$$

Here θ is the angle between the μ^+ spin direction and the e^+ momentum direction in the μ^+ rest frame, x is the standard reduced energy variable $x \equiv E_e/E_e(\max)$ where $E_e(\max) = (m_\mu^2-m_e^2)/2m_\mu = 52.831$ MeV, and $x_o = m_e/E_e(\max)$. The values of the muon decay parameters[29,30] ρ, η, ξ, and δ depend on the relative strengths of the scalar, pseudoscalar, vector, axial-vector and tensor interactions allowed by Lorentz invariance. Table (3.1) shows the (V-A) and (V+A) values of the decay parameters, together with their already existing experimental values[31]. The values assumed by the parameters for more general forms of the interaction are discussed in section (3.5).

Decay Parameter	(V-A) Value	(V+A) Value	Experimental Value
ρ	3/4	3/4	0.7517 ± 0.0026
η	0	0	0.06 ± 0.15
ξ	1	-1	ξP_μ: 0.972 ± 0.14 *
			$\xi P_\mu \delta/\rho$: >0.9959 (90% C.L.)
δ	3/4	3/4	0.7551 ± 0.0085

* P_μ is the muon longitudinal polarization from π^+ decay at rest.

Table (3.1)

3.2 Muon Decay Asymmetry

In this section the muon decay asymmetry for arbitrary values of the decay parameters is compared to the (V-A) prediction and is then related to the parameters ε and ζ which characterize the left-right symmetric model.

From here on the term involving η is assumed to be negligible. In addition to η being small experimentally [Table (3.1)], the term is suppressed by the factor $x_0 \approx 0.01$ and vanishes at the momentum spectrum endpoint. To simplify the discussion further the approximation $m_e=0$ is made temporarily, yielding

$$\frac{d^2\Gamma}{dx\,d(\cos\theta)} \propto x^2\{9(1-x) + 2\rho(4x-3) + \xi\cos\theta[3(1-x) + 2\delta(4x-3)]\} \qquad (3.2)$$

If the μ^+ spin direction is precessed in a magnetic field the rate at which e^+ are emitted in a fixed direction becomes time-dependent through the time-dependence of $\cos\theta$. The instantaneous decay rate,

normalized to the time-averaged ($\cos\theta=0$) rate, is

$$R[x,\theta(t)] = 1 + \frac{3(1-x) + 2\delta(4x-3)}{9(1-x) + 2\rho(4x-3)} \xi\cos\theta(t)$$

The corresponding normalized rate for a purely (V-A) interaction ($\rho=\delta=3/4$, $\xi=1$) is

$$R[x,\theta(t)]_{(V-A)} = 1 + \frac{2x-1}{3-2x} \cos\theta(t)$$

The maximum time variation of the rate, and hence the greatest experimental sensitivity to the degree of parity violation, is attained at $x=1$ and for maximal variations of $\cos\theta(t)$. The spin-precessing magnetic field should therefore be perpendicular to the μ^+ spin direction. The decays of most interest are those in which the e^+ is emitted with x near 1 in a direction close to the μ^+ spin precession plane.

The amplitude of the resulting μSR signal, normalized to that expected for pure V-A muon decay, is

$$A(x) = \frac{R[x,\theta(t)] - 1}{R[x,\theta(t)]_{(V-A)} - 1}$$

and with the definitions $\tilde{x} = 1-x$, $\tilde{\delta} = 1-4\delta/3$ and $\tilde{\rho} = 1-4\rho/3$

$$A(\tilde{x}) \approx (\xi\delta/\rho)\{1 + 2\tilde{x}[\tilde{\delta}/(1-2\tilde{x}) - 3\tilde{\rho}/(1+2\tilde{x})]\} \qquad (3.3)$$

In the (V$\pm$A) limits $A(\tilde{x}) = \mp 1$. For small $\tilde{x}$ the (V-A) values of ρ and δ may be inserted into equation (3.2) provided ξ is then replaced by $A(\tilde{x})$.

An additional modification to equation (3.2) is required because the incoming μ^+ spin direction cannot be observed experimentally. However, in the (V-A) limit with massless neutrinos angular momentum

conservation requires the μ^+ from π^+ decay at rest to be emitted with their spin and momentum directions anti-parallel. Deviations from this limit can only reduce the longitudinal polarization P_μ. With θ redefined to be the angle between the observed μ^+ and e^+ momenta, equation (3.2) becomes

$$\frac{d^2\Gamma}{dxd(\cos\theta)} \propto x^2\{3-2x + P_\mu A(\tilde{x})\cos\theta(1-2x)\} \qquad (3.4)$$

The quantity $P_\mu A(\tilde{x})$ is the amplitude of the μSR signal normalized to that expected for (V-A) decay of μ^+ with $P_\mu=1$. In the context of left-right symmetric theories values of $P_\mu A(\tilde{x})<1$ imply the existence of right-handed currents or $m(\nu_\mu)>0$.

The remainder of this section is devoted to relating $P_\mu A(\tilde{x})$ to the mass-squared ratio $\varepsilon = M^2(W_1)/M^2(W_2)$ and mixing angle ζ of the left-right symmetric model. Following Beg et al.[32], the effective low-energy Lagrangian may be written as

$$L_{eff} = -(G/\sqrt{2})[V_\lambda{}^\dagger V^\lambda + \eta_{aa} A_\lambda{}^\dagger A^\lambda + \eta_{av}(V_\lambda{}^\dagger A^\lambda + A_\lambda{}^\dagger V^\lambda)]$$

where V and A are the vector and axial-vector parts of J_L and J_R. With $M_1 = M(W_1)$, and $M_2 = M(W_2)$:

$$G/\sqrt{2} = (g^2/8M_1^2)(\cos\zeta-\sin\zeta)^2 + (g^2/8M_2^2)(\cos\zeta+\sin\zeta)^2$$
$$\eta_{aa} = (\kappa^2 M_2^2 + M_1^2)/(\kappa^2 M_1^2 + M_2^2)$$
$$\eta_{av} = -\kappa(M_2^2 - M_1^2)/(\kappa^2 M_1^2 + M_2^2)$$
$$\kappa = (1+\tan\zeta)/(1-\tan\zeta)$$

The muon decay parameters are now:

$$\rho = (3/8)[(1+\eta_{aa})^2+4\eta_{av}^2]/[1+\eta_{aa}^2+2\eta_{av}^2]$$

$$\eta = 0$$

$$\xi = -2\eta_{av}(1+\eta_{aa})/[1+\eta_{aa}^2+2\eta_{av}^2]$$

$$\delta = 3/4$$

and to leading order $\xi\delta/\rho = 1-2\varepsilon^2$

$$\tilde{\rho} = 2\zeta^2$$

The μ^+ from π^+ decay at rest have the polarization characteristic of Gamow-Teller β decay:

$$P_\mu = -2(\eta_{aa}/\eta_{av})/[1+(\eta_{aa}/\eta_{av})^2] \approx 1-2(\varepsilon+\zeta)^2$$

Equation (3.3) may now be rewritten in terms of ε and ζ:

$$P_\mu A(\tilde{x}) \approx 1 - 2\{2\varepsilon^2 + 2\varepsilon\zeta + \zeta^2[1 + 6\tilde{x}/(1+2\tilde{x})]\} \qquad (3.5)$$

Each value of $P_\mu A(\tilde{x})<1$ is associated with an elliptical contour in the real ε-ζ plane. Thus measurement of $P_\mu A(\tilde{x})$ constrains both ε and ζ.

3.3 Radiative Corrections

Radiative corrections to muon decay have been evaluated in detail only to order α. The first-order corrections are given by the virtual photon diagrams in Figure (3.1)(a)-(c) and the inner bremsstrahlung diagrams (d) and (e) corresponding to the radiative decay $\mu \to e\nu\bar{\nu}\gamma$. Fischer and Scheck[33] have calculated the radiative corrections for (V-A) decay in the case where the electron polarization is not summed over. The corrections independent of electron spin direction are unchanged if the (V-A) interaction is replaced by a more general vector and axial-vector interaction in charge retention form. Florescu and

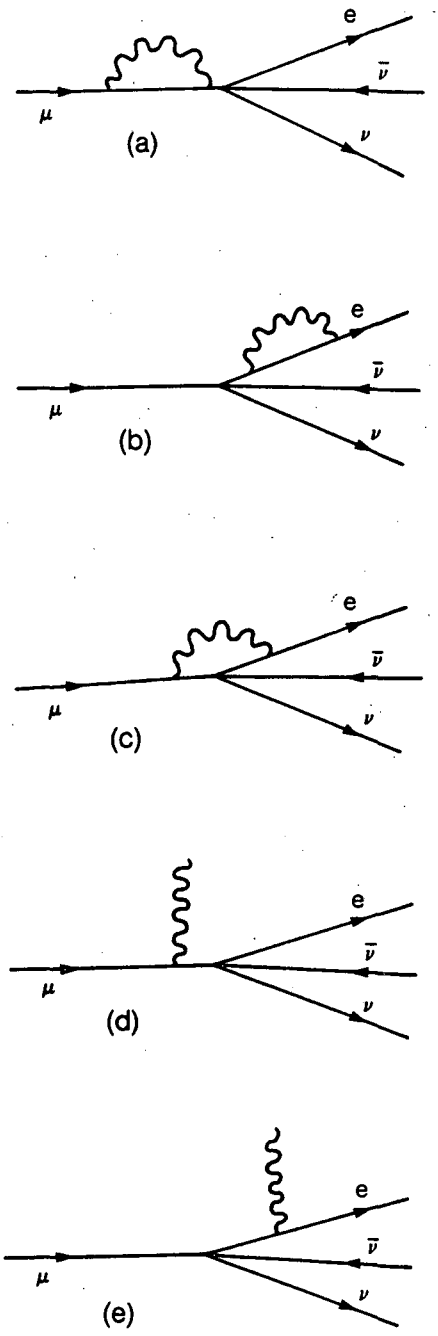

FIGURE (3.1). First-order radiative corrections to muon decay from virtual photon diagrams (a)-(c), and internal bremsstrahlung diagrams (d) and (e).

Kamei[34] have calculated radiative corrections for a general Fermi interaction. Including order α radiative corrections for (V-A) decay and finite electron mass equation (3.4) becomes[29,30]

$$\frac{d^2\Gamma}{dx\,d(\cos\theta)} \propto (1-x_0^2/x^2)^{1/2}\{[x^2(3-2x-x_0^2/x) + f_c(x)] + P_\mu A(\tilde{x})(1-x_0^2/x^2)^{1/2}[x^2(1-2x+m_e x_0/m_\mu) + f_\theta(x)]\cos\theta\} \tag{3.6}$$

where

$$f_c(x) = (\alpha/2\pi)x^2\{2(3-2x-x_0^2/x)R(x) - 3\ell nx + [(1-x)/3x^2][(5+17x-34x^2)\ell n(m_\mu x/m_e) + 2x(17x-11)]\} \tag{3.7}$$

$$f_\theta(x) = (\alpha/2\pi)x^2\{2(1-2x+m_e x_0/m_\mu)R(x) - \ell nx - [(1-x)/3x^2][(1+x+34x^2)\ell n(m_\mu x/m_e)+3-7x-32x^2+4(1-x)^2\ell n(1-x)/x]\} \tag{3.8}$$

$$R(x) = [\ell n(m_\mu x/m_e)-1][2\ell n(x^{-1}-1)+3/2] + \ell n(1-x)[\ell nx+1-x^{-1}] - \ell nx + 2L_2(x) - \pi^2/3 - 1/2 \tag{3.9}$$

and the Spence function $L_2(x) = -\int_0^x t^{-1}\ell n(1-t)dt$.

It should be noted that R(x), and hence $f_c(x)$ and $f_\theta(x)$, diverge logarithmically as $x\to1$. Qualitatively, the infrared divergences in the virtual photon diagrams are no longer compensated by those of the inner bremsstrahlung diagrams since the phase space for radiative decay vanishes as $x\to1$. These divergences may be eliminated by including multiple soft-photon emission. The main effect near $x=1$ is to replace $1+(2\alpha/\pi)[\ell n(m_\mu/m_e)-1]\ell n(1-x)$ in R(x) [equation (3.9)] by[30]

$$\exp[(2\alpha/\pi)[\ell n(m_\mu/m_e)-1]\ell n(1-x) = (1-x)^{(2\alpha/\pi)[\ell n(m_\mu/m_e)-1]}$$

which vanishes as $x\to1$ instead of diverging. It follows that an approximate correction of order α^2 may be made near $x=1$ by replacing

R(x) with

$$R_2(x) = R(x) + (2\alpha/\pi)\{\ell n(1-x)[\ell n(m_\mu/m_e)-1]\}^2 \qquad (3.10)$$

although, of course, $R_2(x)$ still diverges as $x \to 1$.

The data analysis uses equation (3.6) together with the radiative corrections of equations (3.7) through (3.10) to represent the μ^+ differential decay rate. Figure (3.2) shows the resulting e^+ momentum spectra parallel and anti-parallel to the μ^+ spin. The radiative corrections are clearly not negligible.

3.4 Effects of Intermediate Vector Bosons

As noted in section (3.1) the μ^+ differential decay rates for the (V-A) contact interaction and the W_L-mediated interaction differ by terms of order $(m_\mu/M_W)^2$. The effect may be approximated by modifying the decay parameters as[28]

$$\xi_W = 1 + 3m_\mu^2/5M_W^2$$

$$\rho_W = 3/4 + m_\mu^2/3M_W^2$$

and the decay rate as $\tau_W^{-1} = \tau^{-1}(1 + 3m_\mu^2/5M_W^2)$

In addition the order α radiative corrections contain extra terms[35] of order $\alpha(m_\mu/M_W)^2$. These effects are all negligible in the present experiment.

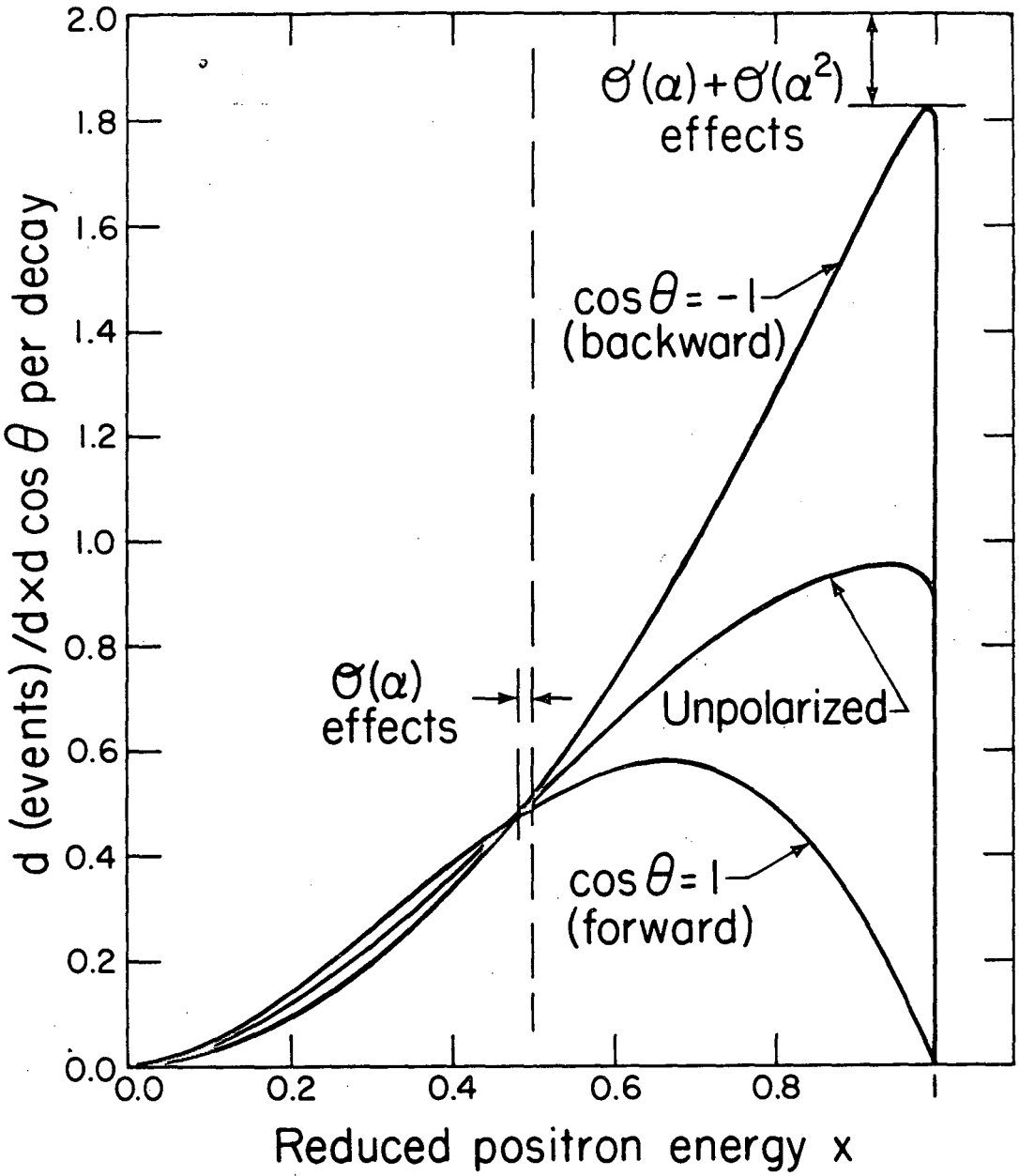

FIGURE (3.2). The (V-A) μ^+ differential decay rate parallel (backward) and anti-parallel (forward) to the μ^+ spin direction, and for unpolarized μ^+. The effects of radiative corrections are also indicated.

3.5 Lorentz Structure

Mursula and Scheck[36] have recently obtained limits on non-(V-A) couplings using a helicity projection form of the muon decay flavor retention contact interaction:

$$\begin{aligned} H = (G_0/\sqrt{2})\{&h_{11}(s+p)_{e\nu_e}(s+p)_{\nu_\mu\mu} + h_{12}(s+p)(s-p) + h_{21}(s-p)(s+p) \\ &+ h_{22}(s-p)(s-p) + g_{11}(v^\alpha+a^\alpha)(v_\alpha+a_\alpha) + g_{12}(v^\alpha+a^\alpha)(v_\alpha-a_\alpha) \\ &+ g_{21}(v^\alpha-a^\alpha)(v_\alpha+a_\alpha) + g_{22}(v^\alpha-a^\alpha)(v_\alpha-a_\alpha) \\ &+ f_{11}(t^{\alpha\beta}+t'^{\alpha\beta})(t_{\alpha\beta}+t'_{\alpha\beta}) + f_{22}(t^{\alpha\beta}-t'^{\alpha\beta})(t_{\alpha\beta}-t'_{\alpha\beta}) + \text{h.c.}\} \end{aligned} \tag{3.11}$$

where $s_{ik} = \bar{\psi}_i 1 \psi_k$, $p_{ik} = \bar{\psi}_i \gamma_5 \psi_k$, $v^\alpha_{ik} = \bar{\psi}_i \gamma^\alpha \psi_k$, $a^\alpha_{ik} = \bar{\psi}_i \gamma^\alpha \gamma_5 \psi_k$, $t^{\alpha\beta}_{ik} = \bar{\psi}_i (\sigma^{\alpha\beta}/\sqrt{2})\psi_k$, $t'^{\alpha\beta}_{ik} = \bar{\psi}_i (\sigma^{\alpha\beta}\gamma_5/\sqrt{2})\psi_k$ and the particle indices are as indicated in the h_{11} term.

The pure (V-A) interaction is very simple in this form: only $g_{22}\neq 0$. The combinations of covariants in each term project onto states of definite helicity in the limit of massless particles, and eliminate interference terms except between (scalar ± pseudoscalar) and tensor interactions.

The deviations of the muon decay parameters from their (V-A) values are

$$\rho - 3/4 = -(12/A)\{|g_{12}|^2+|g_{21}|^2+2|f_{11}|^2+2|f_{22}|^2+\text{Re}(h_{11}f_{11}^*+h_{22}f_{22}^*)\}$$

$$\delta - 3/4 = (36/A\xi)\{|g_{12}|^2-|g_{21}|^2-2|f_{11}|^2+2|f_{22}|^2-\text{Re}(h_{11}f_{11}^*-h_{22}f_{22}^*)\}$$

$$\xi - 1 = -(8/A)\{4(|g_{11}|^2+2|g_{12}|^2-|g_{21}|^2)+|h_{11}|^2+|h_{21}|^2-4|f_{11}|^2+16|f_{22}|^2 - 8\text{Re}(h_{11}f_{11}^*-h_{22}f_{22}^*)\}$$

$$\eta = (8/A)\text{Re}[g_{21}(h_{22}^*+6f_{22}^*)+g_{12}(h_{11}^*+6f_{11}^*)+g_{22}h_{21}^*+g_{11}h_{12}^*]$$

where $$A = 4\{4(|g_{22}|^2+|g_{11}|^2+|g_{12}|^2+|g_{21}|^2)+|h_{11}|^2+|h_{12}|^2+|h_{21}|^2+|h_{22}|^2 + 12(|f_{11}|^2+|f_{22}|^2)\}$$

The couplings are related to equation (3.3) by equation (3.12):

$$A(0) = \xi\delta/\rho = 1 - \frac{8|g_{11}|^2+2|h_{21}|^2+2|h_{11}-2f_{11}|^2}{4(|g_{11}|^2+|g_{22}|^2)+|h_{12}|^2+|h_{21}|^2+|h_{11}-2f_{11}|^2+|h_{22}-2f_{22}|^2}$$

Measurement of $P_\mu A(0) \leq A(0)$ therefore allows limits to be set on the couplings g_{11}, h_{11}, h_{21}, and f_{11}. Limits from the present experiment are presented in section (9.6).

Several constraints are imposed on the couplings if it is assumed that (i) the charged weak interactions are mediated by heavy bosons with spin 0, 1, or 2, (ii) the vector and tensor boson couplings are e-μ universal, and (iii) the scalar boson coupling may instead be proportional to the lepton mass (weak universality):

h_{12}, h_{21} real, positive semi-definite

$h_{22}=h_{11}^*$ with $|h_{11}|^2=h_{12}h_{21}$

g_{11}, g_{22} real, positive semi-definite

$g_{21}=g_{12}^*$ with $|g_{12}|^2=g_{11}g_{22}$

$f_{22}=f_{11}^*$

Limits on g_{11}, h_{11}, h_{21}, and f_{11} therefore constrain other couplings. It should also be noted that any deviation of δ from 3/4 would indicate a violation of e-μ universality.

Two special cases are of interest:

1) In the standard electroweak model where the charged weak interaction is mediated by a single heavy vector boson $W^\pm$ which couples universally

$$A(0) = 1 - 2|g_{11}|^2/(|g_{11}|^2+|g_{22}|^2)$$

and more significantly $\quad P_\mu = (g_{22}-g_{11})/(g_{22}+g_{11})$

so that $$P_\mu A(0) \approx 1 - 2g_{11}/g_{22}$$

2) In the context of the left-right symmetric model g_{11} and g_{12} provide measures of ε and ζ.

Chapter 4

Muons in Matter

4.1 Muon Deceleration and Thermalization

The deceleration and thermalization of μ^+ in matter has been reviewed by Brewer et al.[37] The main energy-loss processes depend on the μ^+ energy. For kinetic energies E>2-3 keV the energy loss is by scattering with electrons. The μ^+ beam is partially depolarized through spin exchange with the unpolarized electrons of the medium[38]. The calculation in section (4.2) shows the depolarization to be 7×10^{-4} for surface muons. In addition, multiple Coulomb scattering from nuclei, which is non-relativistically spin conserving, misaligns the μ^+ spin and momentum directions. At E≈2-3 keV the μ^+ velocity is comparable to that of the valence electrons of the medium. The μ^+ then begin to capture and lose electrons rapidly, forming a succession of short-lived muonium (μ^+e^-) states. Again energy is lost in collisions with electrons. Below E≈200 eV stable muonium is formed, and the energy loss is due to collisions of muonium with atoms and molecules. The time spent by the decelerating μ^+ in muonium states is too short for the hyperfine transitions to cause any appreciable depolarization.

In many non-metals the μ^+ are thermalized as muonium. In others, muonium with E≈1-20 eV participates in 'hot atom' reactions where the μ^+ become incorporated into molecules. The stopping targets in the present work were either metals or liquid helium. The μ^+ are thermalized in metals in a quasi-free state because the high conduction electron concentration effectively screens the μ^+ from interactions with individual electrons. In liquid He the energetically favored final

state is the molecular ion $He\mu^+$ with binding energies[39] of 1.9 eV for the ground state and 1.2 eV for the first vibrational state. Muonium is strongly disfavored in the final state due to the large difference between the ionization potentials of helium (24.6 eV) and muonium (13.5 eV). However, if any muons are thermalized as muonium they may survive in this form for a considerable time because of the improbability of encountering a He^+ ion with which to recombine as $He^+ + \mu^+e^- \rightarrow He\mu^+$.

4.2 Muon Depolarization in Scattering from Unpolarized Electrons

Ford and Mullin[38] have shown that when non-relativistic μ^+, with velocity β in the laboratory frame, scatter with unpolarized e^- through a center of mass angle θ the probability that the final μ^+ spin direction is parallel ($\varepsilon=1$) or anti-parallel ($\varepsilon=-1$) to the initial spin direction is:

$$Q(\varepsilon,\theta) = \frac{1+\varepsilon}{2} - \varepsilon \frac{m^2}{\mu^2} \beta^4[\sin^2(\theta/2) - \sin^4(\theta/2) + \sin^6(\theta/2)]$$

where $m=m_e$ and $\mu=m_\mu$.

If the muons are initially fully polarized the final polarization after one scatter through θ is

$$P_\mu = 1 - 2 \frac{m^2}{\mu^2} \beta^4[\sin^2(\theta/2) - \sin^4(\theta/2) + \sin^6(\theta/2)]$$

The corresponding fractional energy loss is

$$w = \frac{m}{\mu} \beta^2 \sin^2(\theta/2).$$

With $\Delta P_\mu = 1-P_\mu$ the 'depolarizing power' of a given fractional energy loss is

$$\frac{\Delta P_\mu}{w} = 2\frac{m}{\mu}\beta^2[1 - \sin^2(\theta/2) + \sin^4(\theta/2)]$$

and

$$\frac{d}{d[\sin^2(\theta/2)]}\frac{\Delta P_\mu}{w} = 2\frac{m}{\mu}\beta^2[-1 + 2\sin^2(\theta/2)]$$

The depolarization per unit energy loss is maximized for $\theta\to 0$ and π, and is reduced by 25% at the $\theta=\pi/2$ minimum. In the non-relativistic limit the scattering cross section $\sigma \sim \mathrm{cosec}^4(\theta/2)$. Then considering only small angle scattering the polarization after one scatter is

$$P_\mu \approx 1 - 2\frac{m^2}{\mu^2}\beta^4\sin^2(\theta/2)$$

with corresponding energy-loss

$$dE = -Ew = -\mu(\gamma-1)w \approx -m(\gamma-1)\beta^2\sin^2(\theta/2)$$

The number of such scatters resulting in an energy loss δE such that $dE \ll \delta E \ll E$ is

$$N = \frac{\delta E}{dE} = \frac{\delta E}{m(\gamma-1)\beta^2\sin^2(\theta/2)}$$

and the polarization is then

$$P_\mu(\delta E) = [1 - 2\frac{m^2}{\mu^2}\beta^4\sin^2(\theta/2)]^N$$

$$\simeq 1 - 2\frac{m^2}{\mu^2}\frac{\beta^2}{\gamma-1}\delta E$$

$$= 1 - 2\frac{m}{\mu^2}\frac{\gamma+1}{\gamma^2}\delta E$$

The depolarization of non-relativistic ($\gamma \approx 1$) muons is therefore almost independent of their energy and proportional to their energy loss. Surface muons initially have E=4.1 MeV and γ=1.04. Using ΔE=4.1Mev and γ=1.02 the depolarization when the μ^+ are (almost) brought to rest is

$$1 - P_\mu = 2 \frac{m}{\mu^2} \frac{\gamma+1}{\gamma^2} \Delta E = 7.3 \times 10^{-4}$$

4.3 Spin-Lattice Relaxation

In order to obtain the most precise value of the measured muon mean-life τ_μ to use in fitting the μSR data one would like to include information from the spin-held mode of the experiment. However, muon spin-lattice relaxation in the spin-held mode conspires with parity violation to change the measured τ_μ from its true value.

It should first be pointed out that while the 1.1-T spin-holding field is sufficient to quench μ^+ depolarization in muonium, it cannot 'hold' the spins of quasi-free muons in the metal targets. The energy difference between states where the muon spin is parallel and anti-parallel to the 1.1-T field is only $\Delta E = 6.2 \times 10^{-7}$ eV, whereas the room temperature thermal energy is $kT = 2.6 \times 10^{-2}$ eV. Relaxation of the muon spins toward the equilibrium situation, where the numbers of spins anti-parallel and parallel to the applied field are almost equal, requires the presence of oscillating magnetic fields with frequency $\omega = 9 \times 10^8$ s^{-1}. Such fields are provided by the nuclear magnetic dipole moments and the lattice vibrations associated with low frequency acoustic phonons. The stopped muon polarization decays exponentially toward thermal equilibrium with the characteristic spin-lattice

relaxation time constant T_1.

Now consider a μ^+ with its spin anti-parallel to the beam direction. According to (V-A) theory the probabilty that the decay e^+ is emitted along the beam direction is enhanced by a factor of

$$E(x) = 1/2(1-x)$$

if the muon spin direction is reversed. The decay time spectrum becomes

$$N(x,t) = N_0 \exp(-t/\tau_\mu)\{\exp(-t/T_1) + E(x)[1-\exp(-t/T_1)]\}$$

If T_1 is much longer than the observation time the decay spectrum appears almost exponential with an effective measured muon mean-life τ_μ' given by:

$$\tau_\mu' = \frac{\tau_\mu T_1}{T_1 - [E(x)-1]\tau_\mu} \qquad (4.1)$$

Thus $\tau_\mu' > \tau_\mu$ for $x>1/2$, and the effect increases rapidly as $x \to 1$.

The spin-held data from the second running period ('Run 2') with $x>0.88$ is shown in Figure (4.1). The fitted muon mean-life is $\tau_\mu' = 2.214 \pm 0.004(\text{stat})$ μs and the fitted background of 1.2 ± 9.8 per time bin is consistent with zero.

Figure (4.2) shows the τ_μ' of the spin-held data fitted as a function of the decay e^+ momentum. The background, which was found to be consistent with zero throughout the x range, was fixed to zero. The Run 2 and Run 3 aluminum target data has been combined. Different μ^+ lifetime clocks were used in each of the three running periods, and the lower statistics Run 1 data has been omitted since it covered a shorter x range than the Run 2 and Run 3 data. The curves are fits to equation (4.1) with finite angular acceptance effects included in E(x) and

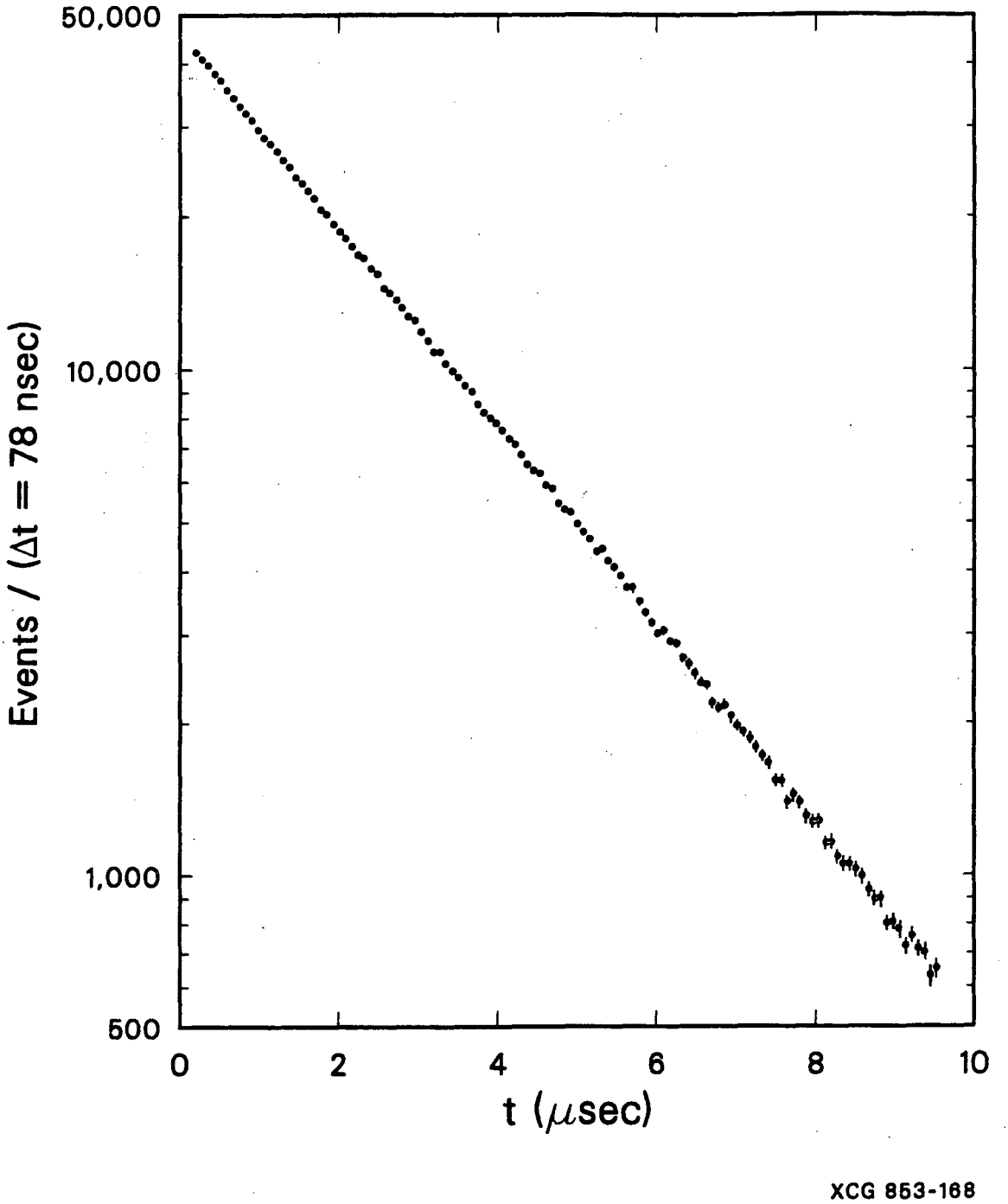

FIGURE (4.1). Time spectrum of the spin-held data from Run 2. The fitted muon mean-life is τ_μ=2.214±0.004(stat.) μs with a fitted background of 1.2±9.8 per time bin.

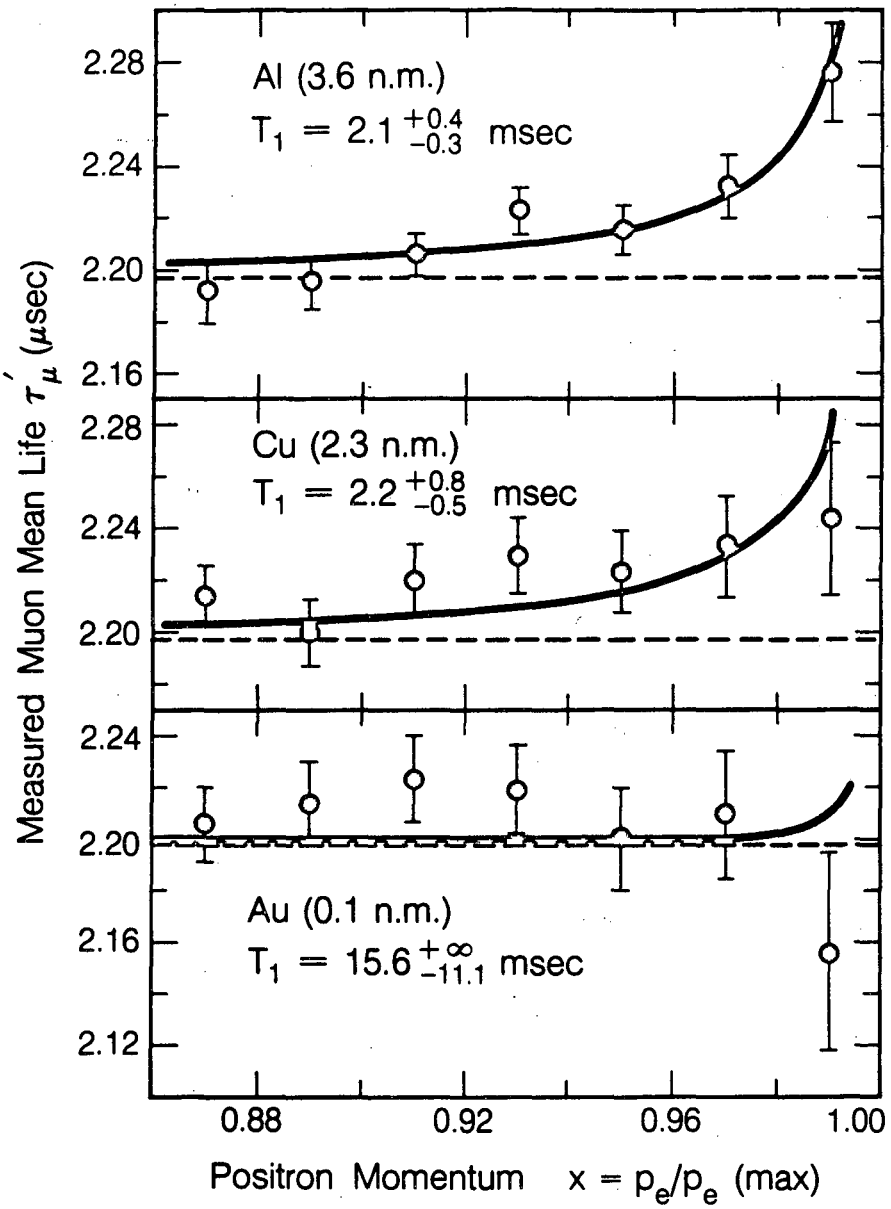

FIGURE (4.2). Fitted muon mean-life τ_μ' versus decay positron momentum for spin-held data from aluminum, copper, and gold targets. The target material nuclear magnetic moment in units of nuclear magnetons (n.m.) is indicated. The correlation between the putative spin-lattice relaxation times T_1 and the nuclear magnetic moments suggests a real spin-lattice relaxation effect.

assuming the true muon mean-life τ_μ=2.197 μs. The best fit spin-lattice relaxation time constants of $T_1=2.1^{+0.4}_{-0.3}$ ms for Al, $T_1=2.2^{+0.8}_{-0.5}$ ms for Cu, and $T_1=15.6^{+\infty}_{-11.1}$ ms for Au correlate with their respective nuclear dipole moments of 3.6, 2.3, and 0.1 nuclear magnetons. This correlation suggests the effect is due to spin-lattice relaxation rather than some residual background problem. In principle the foregoing method provides a means of measuring μ^+ spin-lattice relaxation time constants $T_1 \sim 10^3 \tau_\mu$.

In conclusion no spin-held data muon lifetime information is used in fitting the μSR data, which is time-average unpolarized, since the two data sets do not necessarily have the same apparent τ_μ.

4.4 Spin-Spin Relaxation: μSR Signal Damping

The spins of muons stopped in the target material precess under the combined influence of the external transverse magnetic field and the randomly oriented internal local fields produced mainly by the nuclear magnetic dipole moments. The muon spins therefore precess with slightly different Larmor frequencies resulting in a loss of phase coherence.

The decay of the spin phase coherence is observed experimentally as a damping, G(t), of the μSR signal amplitude. This is seen in Figure (4.3) which displays data from the second run period. Although the μSR signal damping can yield much information about the environment in which the μ^+ are brought to rest, it is clearly an unwelcome nuisance in an experiment where one would like to measure a μSR signal amplitude determined solely by the weak interaction. If the exact form of G(t) were known the desired amplitude would, in principle, be simply the time t=0 amplitude obtained from a fit to the μSR data. Unfortunately,

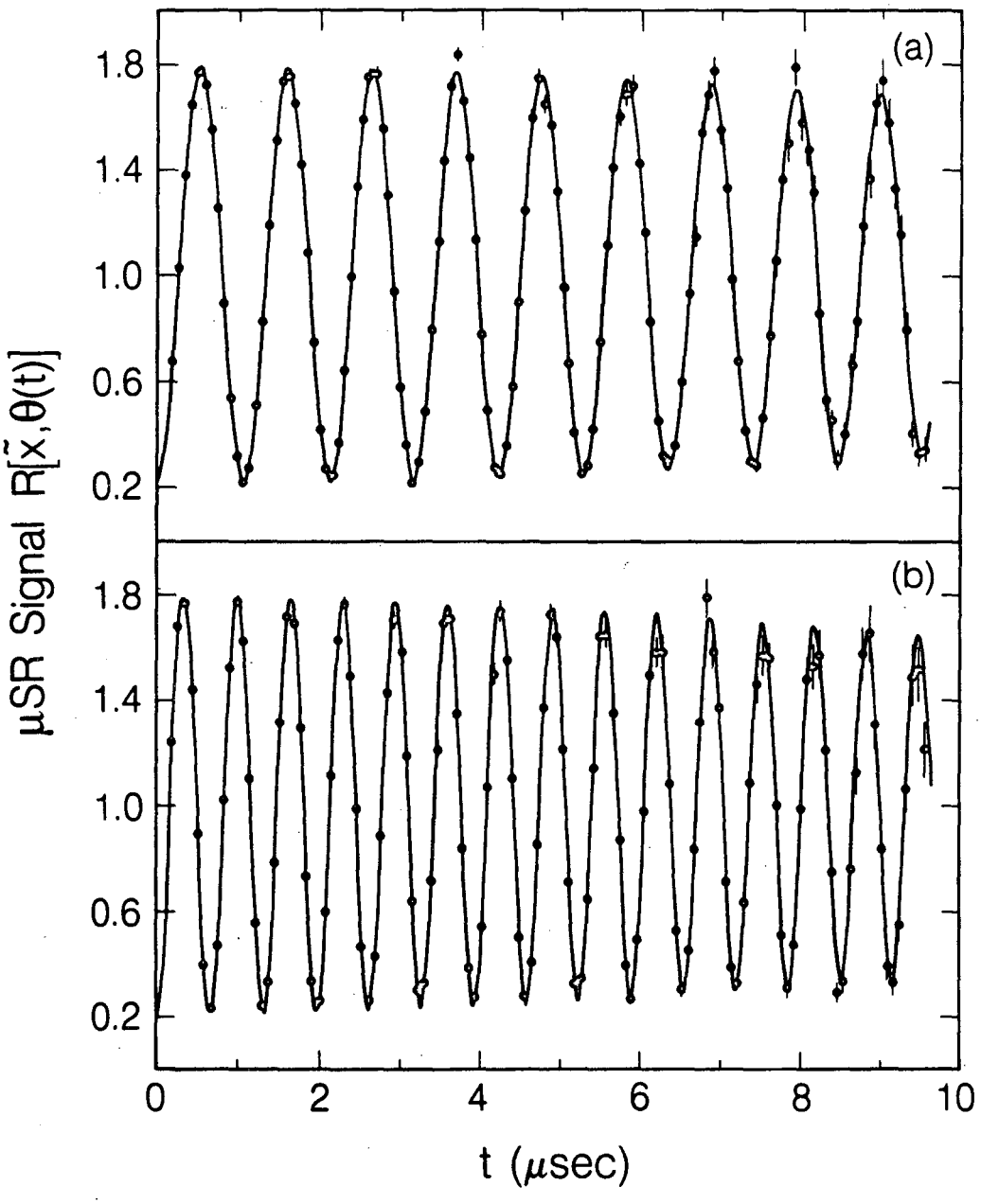

FIGURE (4.3). The μSR data from Run 2, contributing 73% of the total data base for the final results, with spin-precessing fields (a) B_T=70-G, and (b) B_T=110-G. The exponential decay with muon lifetime has been factored out. Spin-spin relaxation causes a damping of the μSR signal amplitude.

there is no 'magic formula' for G(t) which describes exactly the signal damping observed in real, i.e. imperfect, materials such as metals which contain, to some degree, impurities and lattice defects. However, it will be seen in the following discussion that approximate expressions for G(t) can be obtained if certain simplifying assumptions are made.

A wealth of general information about spin depolarization in μSR experiments can be found in the proceedings of recent topical conferences[40]. The recent review of transport mechanisms of light interstitials in metals by Richter[41] summarizes much useful information.

In metals with large nuclear dipole moments such as copper and aluminum the local dipole fields are a few Gauss at the interstitial lattice sites occupied by the muons. The μ^+ spin phase coherence decays according to the ensemble average

$$G(t)\exp(i\omega_0 t) = \langle \exp[i\int_0^t \omega(t')dt'] \rangle$$

where $\omega(t) = \omega_0 + \omega'(t)$ with ω_0 the Larmor frequency in the external field alone and $\omega'(t)$ the frequency shift due to dipolar interactions. An approximate analytic expression for G(t) can be obtained by assuming (i) that the frequency modulation $\omega'(t)$ is random, (ii) that it is a Gaussian random process so that only the second-order cumulant, or correlation function of $\omega'(t)$ with $\omega'(0)$, need be considered and (iii) that the correlation function decays exponentially with a correlation time τ_c characteristic of the time a μ^+ resides at a lattice site before diffusing to another. The correlation function becomes

$$\langle\omega'(t)\omega(0)\rangle = \langle\omega'(0)^2\rangle\exp(-t/\tau_c) = 2\sigma^2\exp(-t/\tau_c)$$

and then $$G(t) = \exp\{-2\sigma^2\tau_c^2[\exp(-t/\tau_c)-1+t/\tau_c]\} \qquad (4.2)$$

Equation (4.2) is the Kubo-Tomita[42] or motional-narrowing form of the spin relaxation function.

In the limiting case of immobile μ^+ $G(t,\tau_c\to\infty) = \exp(-\sigma^2t^2)$, while for extremely mobile μ^+ the local field fluctuations are averaged and motional-narrowing occurs: $G(t,\tau_c\to 0) = \exp(-2\sigma^2\tau_c t)$. For intermediate values of τ_c equation (4.2) provides a useful interpolation between the Gaussian and exponential limits.

The static linewidth σ^2 is related to the random local dipole fields ΔB by

$$\sigma^2 = \gamma_\mu^2\langle\Delta B^2\rangle/2 \qquad (4.3)$$

where $\gamma_\mu = 8.5\times10^4$ radians/sec-G, and is given by the van Vleck formula[43]

$$\sigma^2 = (\hbar^2/6)\gamma_\mu^2\gamma_I^2 I(I+1)\sum_j(1-3\cos^2\theta_j)^2/r_j^6 \qquad (4.4)$$

where r_j is the distance of the μ^+ from the nuclear spin I_j, θ_j is the angle between $\hat{r}_j$ and the external field direction, and γ_μ and γ_I are the gyromagnetic ratios for the μ^+ and nuclei, respectively. Acccording to equation (4.4) σ^2 depends markedly on the crystal lattice orientation relative to the external field. However, for the small external fields used in the present experiment (≈100 G) the orientation dependence is reduced strongly by additional interactions between the nuclear quadrupole moments and the electric field gradient produced by

the muon.

The main shortcomings in the assumptions used to obtain G(t) in equation (4.2) are now considered. Kehr et al.[44] have shown that inclusion of only the second-order cumulant leads to a more rapid damping than that exhibited by their more general Markovian-random walk formulation. Although the precession frequency shifts ω' are different at each interstitial site there are correlations between the ω' at neighboring sites because the μ^+ is subject to some of the same nuclear spins. This effect can be treated approximately by using a correlation time τ_c longer than the mean μ^+ residence time at each site. In addition, since the μ^+ has been regarded as a classical particle localized at specific sites, possible delocalization effects have been neglected.

The preceding discussion has also ignored the possibility that μ^+ become trapped at lattice defects. The defects may be impurities such as oxygen or nitrogen atoms which trap μ^+ below about 80 K, lattice vacancies or dislocations which trap μ^+ up to about room temperature, or larger voids in which the surface electric dipole layer and image force can produce a deep trapping well[45]. Kehr et al.[44] have also constructed a Markovian-random walk theory of spin depolarization for diffusion in the presence of traps. They consider a two state model in which the μ^+ is either trapped for an average time τ_0 during which $G(t)=\exp(-\sigma_0^2 t^2)$, which is the simplest approximation corresponding to muons at fixed sites in the traps, or is untrapped for an average time τ_1 during which G(t) is taken to be their result in the absence of traps. The contributing random walk processes are summed in integral equations which are solved by Laplace transform and inverted

numerically to yield G(t). It should be noted that the initial conditions are not equilibrium conditions since the μ^+ are stopped at random sites. If the concentration of traps is c then at time t=0 the fraction of μ^+ in traps is c, while under equilibrium conditions the fraction is $\tau_0/(\tau_0+\tau_1)$. At room temperature equilibrium should be established in times short compared to the mean μ^+ lifetime.

The observed μSR signal damping, in principle, has a small spin-lattice relaxation component. Any non-uniformities in the applied spin-precessing field B_T also contribute.

It should now be clear that the G(t) of equation (4.2) can provide only an approximation to the true form of the μSR signal damping. Therefore fitting the μSR data assuming equation (4.2) to be valid may lead to a fitted time t=0 amplitude either smaller or larger than the true amplitude. The approach taken in the data analysis discussed in Chapter 7 is to use the Gaussian limit of equation (4.2) and then try to show that this underestimates the true time t=0 amplitude. This procedure yields more conservative limits on right-handed currents.

Chapter 5

The Beamline and Apparatus

5.1 The Beamline

The TRIUMF M13 beamline[46] shown in Figure (5.1) is a low momentum (20-130 MeV/c) pion and muon channel viewing the 1AT1 production target at 135° with respect to the primary proton beam. The secondary beam is transported through two 60° bends, the first right and the second left, to a final focus (F3) nominally 9.4 m downstream of the production target. The symmetric quadrupole triplet (Q3-Q5) produces a relative inversion of the images at the intermediate foci F1 and F2, thereby yielding an achromatic focus at F3. The symmetric configuration of the beamline elements also suppresses second order effects and produces a magnification of unity at F3. The beam phase space is governed by the setting of the horizontal and vertical jaws (J) upstream of the first dipole (B1). The momentum bite is restricted by the horizontal components of slits SL1 and SL2 at the intermediate foci F1 and F2. With the exception of B1 in Run 1, the dipoles were NMR-monitored.

Figure (5.2) shows the positive particle fluxes obtained in the beam tuning studies of ref. (46). For data collection in the present experiment the beamline was tuned to 29.5 MeV/c, i.e. 1% below the 29.8 MeV/c surface muon edge. This allowed a 2% $\Delta p/p$ momentum bite during occasional periods of low primary proton flux, although a 1% $\Delta p/p$ was normally used. Under normal running conditions 100 μA of 500 MeV protons incident on a 2 mm thick carbon production target yielded 1.8×10^4 μ^+/sec at the stopping target. The μ^+ beam spot rms spatial and angular dimensions were typically 6 mm and 35 mrad

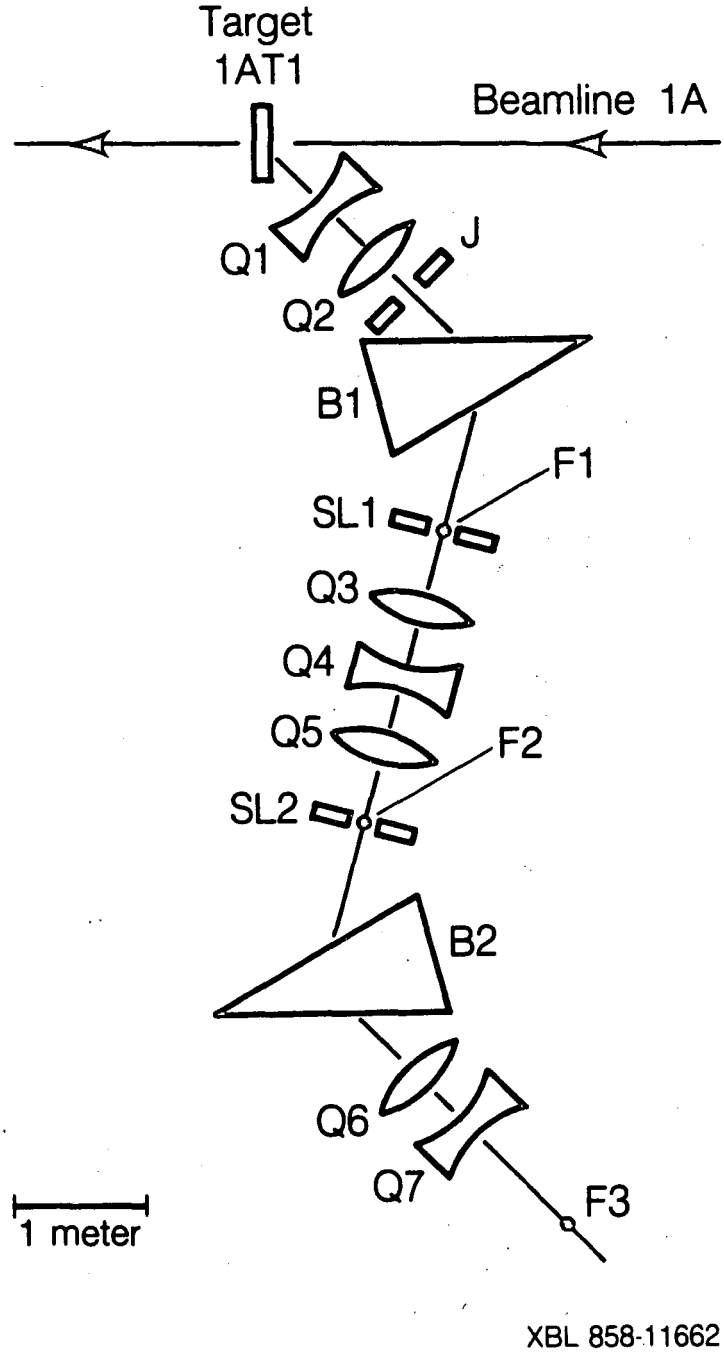

FIGURE (5.1). The TRIUMF M13 beamline. B1 and B2 are dipoles; Q1-Q7 are quadrupoles; F1-F3 are foci; the slits SL1 and SL2, and the jaws J have both horizontal and vertical components.

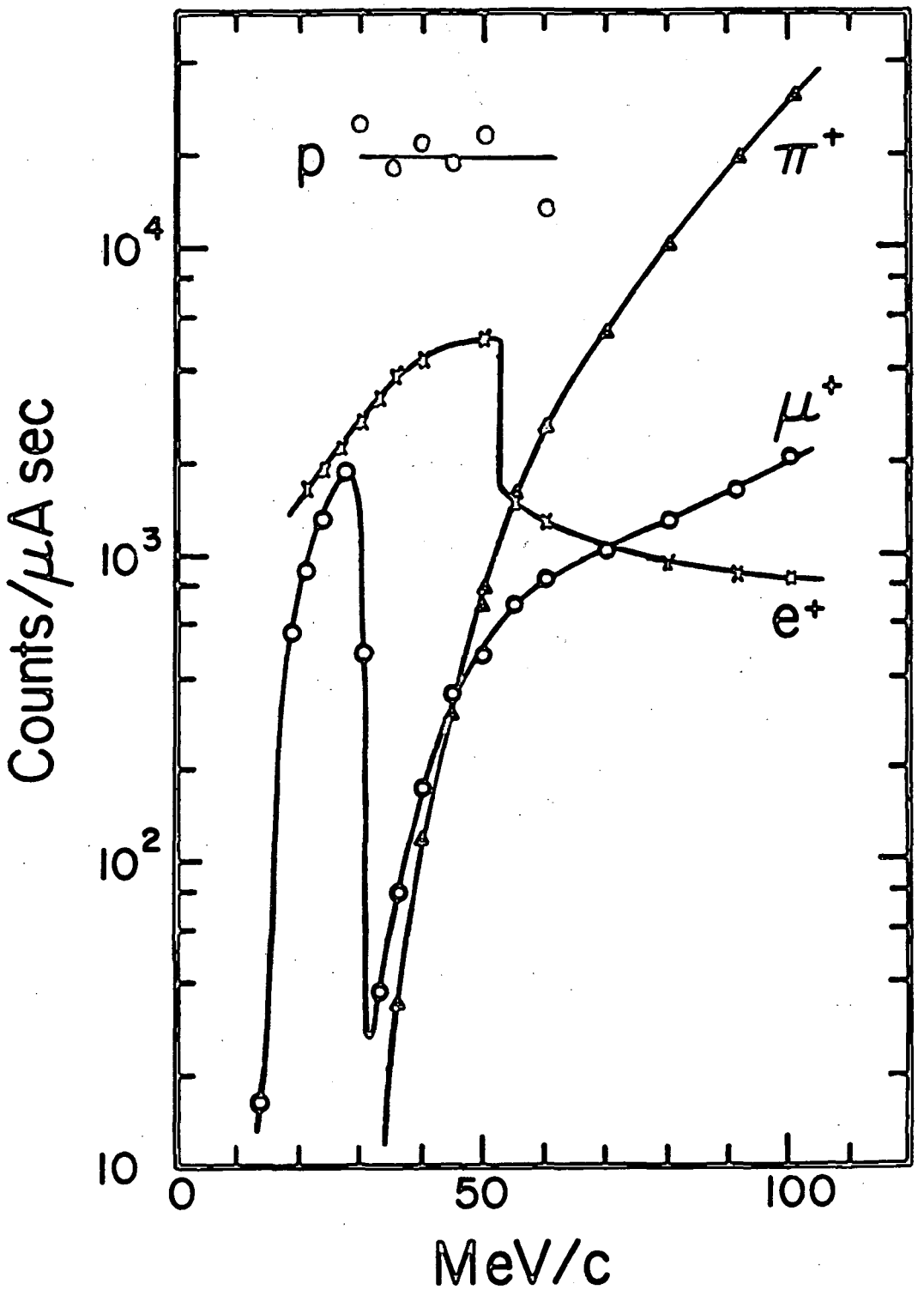

FIGURE (5.2). Particle fluxes versus beamline momentum setting (taken from ref. 46).

horizontally, and 5 mm and 70 mrad vertically.

Beam e^+ pass through the stopping target and do not satisfy the trigger requirements. Beam protons are stopped far upstream, mostly in the beamline vacuum window. The pulsed nature of the primary proton beam allows prompt π^+ and μ^+ from π^+ decay in flight to be eliminated by timing cuts relative to the cyclotron rf cycle.

Approximately 2% of the μ^+ flux originates from π^+ decay in flight. These 'cloud' μ^+ are, on average, far less polarized than the surface muons. As an extreme example, the (V-A) backward decay of an 81.0 MeV/c π^+ yields a forward moving 29.5 MeV/c μ^+ with parallel spin and momentum directions, thereby mimicking a (V+A)-produced surface muon. However, efficient transport of cloud muons to the stopping target beam spot (F3) requires the in-flight π^+ decays to occur close to the production target, i.e. to be prompt. The primary protons arrive at the production target in bursts of 2-5 nsec duration 43 nsec apart. In Figure (5.3)(a) the exponential decay of π^+ at rest (τ_π=23 nsec) underlies the time distribution, relative to the cyclotron rf cycle, of 29.5 MeV/c μ^+ arriving at the stopping target. The residual cloud μ^+ and prompt π^+ peaks are clearly visible in the Figure (5.3)(b) arrival times of 30.5 MeV/c beam particles. Events with beam particle arrival times in the shaded regions of Figure (5.3), which contain 98% of the cloud μ^+, are rejected in the data analysis.

5.2 The Apparatus: An Overview

After traversing the beamline the beam passed through a 2 mil mylar vacuum window and entered the apparatus shown in Figure (5.4). Beam μ^+ were stopped in either a metal foil or liquid helium target positioned

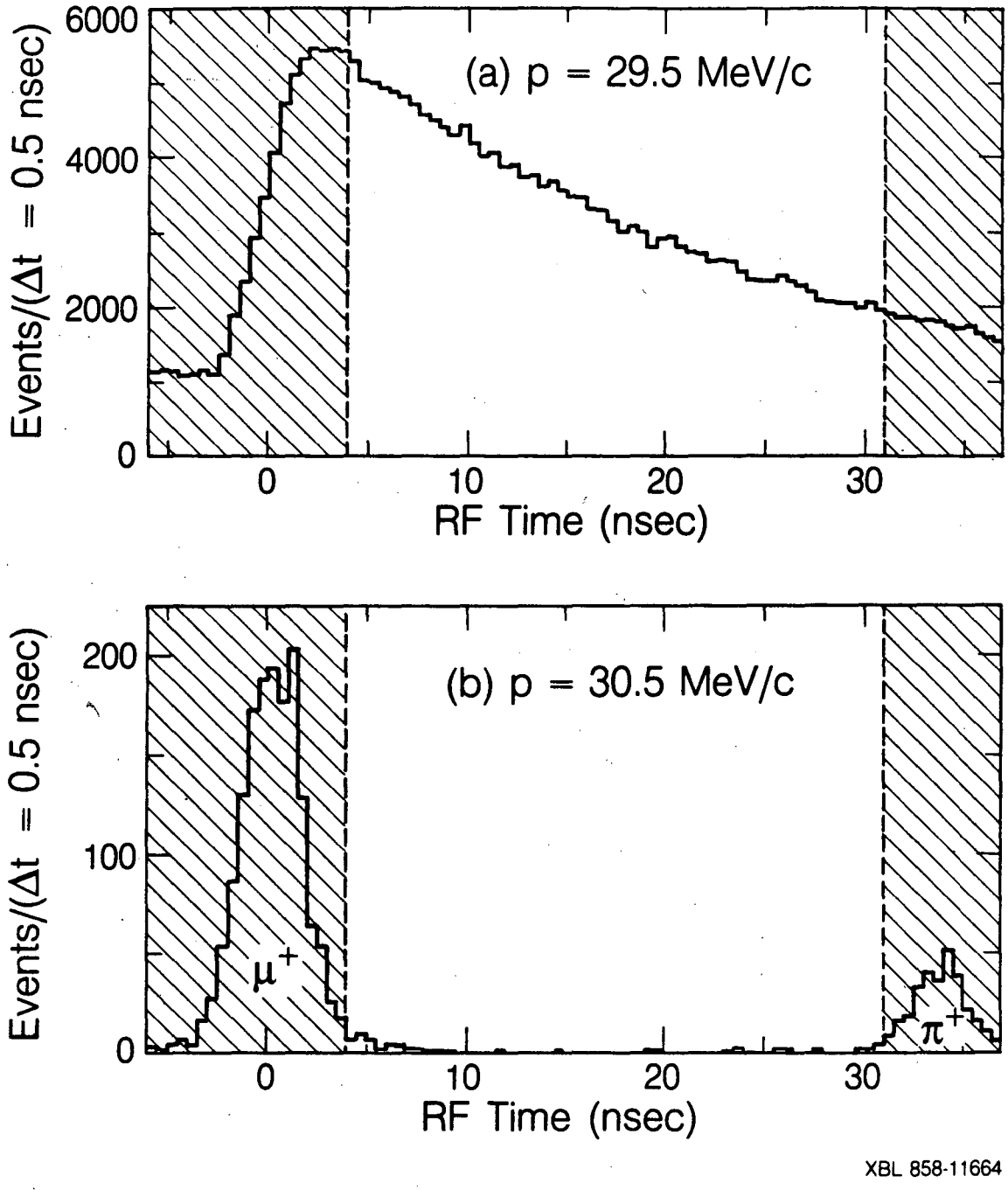

FIGURE (5.3). Beam particle arrival times with respect to the 43 ns cyclotron rf cycle at (a) 29.5 MeV/c and (b) 30.5 MeV/c. The shaded regions contain almost all of the cloud μ^+ and prompt π^+ contaminations and are rejected.

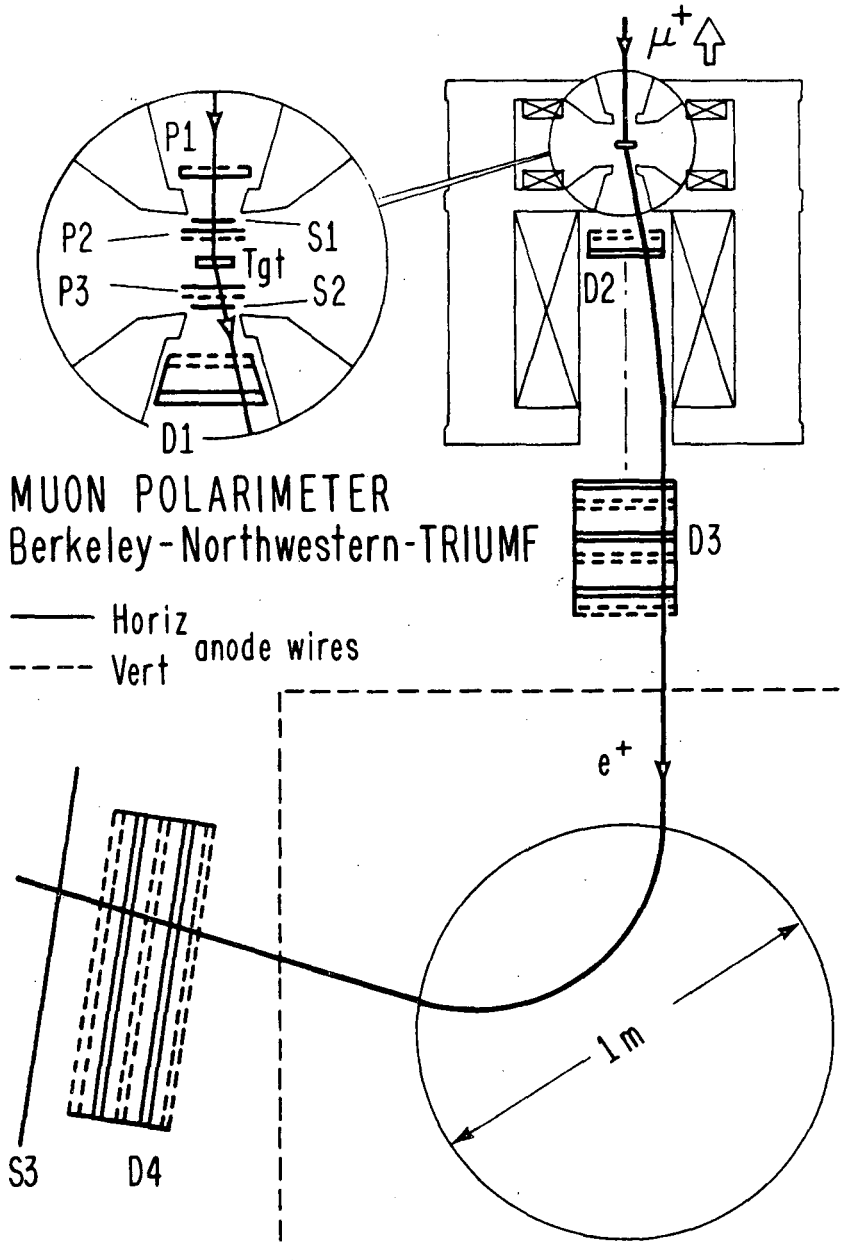

XBL 834-147

FIGURE (5.4). The apparatus. P1-P3 are proportional chambers; S1-S3 are scintillators; D1-D4 are drift chambers. Muons entering the solenoid are stopped in the target (Tgt). Decay e^+ emitted near the beam direction are focused by the solenoid into the spectrometer.

at the center of the upstream section of the solenoid. The amount of material upstream of the stopping target was estimated to be 50 mg/cm^2 in Run 1, 54 mg/cm^2 in Run 2, and 55 mg/cm^2 in Run 3.

Decay e^+ emitted within 270 mrad of the beam direction were focused by the downstream section of the solenoid into a horizontally focusing cylindrical dipole spectrometer for momentum analysis. Multiwire proportional chambers and drift chambers in the target region measured the incoming beam μ^+ and outgoing decay e^+ trajectories. Tracks recorded by drift chambers located near the conjugate foci of the spectrometer allowed reconstruction of the decay e^+ momentum. The amount of material downstream of the stopping target and upstream of the spectrometer was estimated to be 186 mg/cm^2 in Run 1, 193 mg/cm^2 in Run 2, and 216 mg/cm^2 in Run 3.

5.2.1 The Solenoid

The solenoid consists of two co-axial sections essentially decoupled by the intervening septum. The two water-cooled coils of the upstream section produce the longitudinal field for the spin-held mode of the experiment. They have inner diameter 6", outer diameter 10", length 2", 29 turns/coil, and a center-to-center separation of 7". The pole faces and coil separation were designed to minimize radial field components over the target region. Computer simulations using the program POISSON indicated that within a radius of 1" and within ±0.25" longitudinally of the nominal target position the field direction is axial to within 2 mrad.

The vertical transverse field used in the μSR mode was produced by

an additional water-cooled coil. The μSR coil consisted of a single turn of 0.125" × 0.5" copper having four horizontal sections transverse to the beam direction with centers 1.125" above and below the beam axis and 1.94" upstream and downstream of the nominal target position. Studies using the program POISSON indicated that within ±1" of the beam axis and within ±0.7" longitudinally of the target position the longitudinal field component did not exceed 1.0% of the transverse field. Field measurements made with the coil outside the solenoid indicated field strength uniformity of ±0.4% within 0.75" of the beam axis at the nominal target position. Transverse fields of 70-G and 110-G were obtained with coil currents of 475-A and 750-A, respectively.

A residual longitudinal field of about 40-G remaining at the target position after the upstream longitudinal field coils were turned off was nulled to within 2-G by applying a small reverse current to the coils. The null condition was indicated by a maximal ratio of events to stopped μ^+ in Run 1, and by field measurements in Runs 2 and 3.

The downstream section of the solenoid has three coils each with inner diameter 4.5", outer diameter 10", length 6.25" and 120 turns/coil.

Table (5.1) shows the on-axis longitudinal fields calculated by POISSON for the spin-held (B_L) and μSR (B_T) modes. The stopping target position is at zero, with downstream positions being positive. The field values assume 1.31×10^5 A-turns/coil downstream, and 5.45×10^4 A-turns/coil upstream for B_L. For $z>11.25$" $B_{Lz}\approx B_{Tz}$.

z (inch)	$B_{Lz}(z)$ (Gauss)	$B_{Tz}(z)$ (Gauss)	z (inch)	$B_{Lz}(z)$ (Gauss)	$B_{Tz}(z)$ (Gauss)	z (inch)	$B_{Tz}(z)$ (Gauss)
-4.25	283		6.50	5439	5412	22.25	8828
-4.00	388		6.75	6034	6011	22.50	8730
-3.75	528		7.00	6569	6550	22.75	8600
-3.50	719		7.25	7081	7064	23.00	8454
-3.25	1028		7.50	7522	7507	23.25	8291
-3.00	1538		7.75	7894	7881	23.50	8110
-2.75	2385		8.00	8217	8205	23.75	7910
-2.50	3627		8.25	8491	8480	24.00	7691
-2.25	5429		8.50	8721	8711	24.25	7451
-2.00	7358		8.75	8913	8903	24.50	7191
-1.75	9035		9.00	9073	9064	24.75	6912
-1.50	10268		9.25	9204	9195	25.00	6611
-1.25	11014		9.50	9315	9307	25.25	6293
-0.75	11654		9.75	9406	9399	25.50	5956
-0.50	11754		10.00	9480	9473	25.75	5610
-0.25	11801		10.25	9533	9526	26.00	5256
0.00	11811	0	10.50	9580	9573	26.25	4895
0.25	11805	1	10.75	9617	9611	26.50	4527
0.50	11763	2	11.00	9648	9642	26.75	4168
0.75	11668	3	11.25	9674	9668	27.00	3821
1.00	11450	6	11.50		9690	27.25	3483
1.25	11038	11	12.00		9728	27.50	3159
1.50	10300	21	12.50		9755	27.75	2847
1.75	9079	34	13.00		9771	28.00	2559
2.00	7421	56	13.50		9788	28.25	2295
2.25	5523	89	14.00		9794	28.50	2048
2.50	3765	138	14.50		9794	28.75	1819
2.75	2587	206	15.00		9788	29.00	1613
3.00	1821	290	15.50		9782	29.25	1428
3.25	1406	387	16.00		9770	29.50	1260
3.50	1214	505	16.50		9758	29.75	1109
3.75	1170	654	17.00		9738	30.00	974
4.00	1208	831	17.50		9712	30.25	855
4.25	1323	1050	18.00		9676	30.50	749
4.50	1525	1321	18.50		9637	30.75	656
4.75	1803	1649	19.00		9588	31.00	572
5.00	2146	2030	19.50		9531	31.50	435
5.25	2564	2475	20.00		9458	32.00	333
5.50	3059	2990	20.50		9367	32.50	259
5.75	3596	3542	21.00		9251	33.00	220
6.00	4184	4142	21.50		9110	33.50	174
6.25	4805	4772	22.00		8932	34.00	139
						36.00	65

Table (5.1)

5.2.2 The Spectrometer

The spectrometer consisted of an NMR-monitored horizontally focusing cylindrical dipole magnet with drift chambers located near its conjugate foci. The magnet was originally used by Sagane et al.[47] in measurements of the muon decay ρ parameter. The flat pole faces have a diameter of 37" and were separated by a gap of 14.5". When operated at 125-A the water-cooled coils produced a central field of 0.32-T, a 98° bend angle for x=1 decay e^+, and a momentum dispersion of 1.07%/cm. Enclosing the particle trajectories by a vacuum box with 5 mil mylar vacuum windows positioned close to the conjugate focal planes minimized momentum resolution loss due to multiple Coulomb scattering. Drift chambers D3 and D4 [Figure (5.4)] were mounted to the vacuum box immediately upstream and downstream of the vacuum windows, repectively.

5.2.3 Proportional Chambers

The proportional chambers P1, P2, and P3 each had one horizontal and one vertical wire plane separated by a grounded 0.5 mil double-side aluminized mylar sheet. The anode wires were 0.5 mil diameter gold-plated tungsten with 2 mm spacing. Cathode signals obtained from the 0.5 mil single-side aluminized mylar chamber windows were used in the trigger.

Chamber P1 had circular aperture and 32 wires per plane. The windows and ground plane were 4 mm from the wire planes. Chambers P2 and P3 were of identical construction with square aperture and 30 wires per plane. The windows and ground plane were 2 mm from the wire planes.

In Runs 1 and 3 the proportional chamber gas was 92% methane/8%

methylal, and in Run 2 magic gas: 69.7% argon, 30.0% isobutane and 0.3% freon.

The operating voltages, applied to the wires, were 3500 V for P1 and 2500 V for P2 and P3 when using methane/methylal; and 2950 V for P1 and 2050 V for P2 and P3 when using magic gas. Amplifiers for the wire and cathode signals were positioned close to the chambers. The mean efficiency of the wire planes was >99.5% per plane.

An additional chamber, denoted 'A' and identical to P2 and P3, was positioned between P1 and P2 in Run 3 in preparation for a measurement of the decay parameter δ where the extended data momentum range (20-53 MeV/c) made highly efficient rejection of 'straight-through' beam e^+ events essential.

5.2.4 Drift Chambers

The planar drift chambers D1-D4 [Figure (5.4)] were composed of sub-units each containing two planes of horizontal or vertical sense wires. The sense planes were staggered by a half cell width to resolve left-right ambiguities. The cell geometries used in D1, D2 and D3, and D4 are shown in Figure (5.5). The sense wires were 0.5 mil diameter gold-plated tungsten and the field wires were 3 mil diameter berylium-copper.

D1 was of conical geometry. The wire spacing within each plane was 0.400" and the spacing between planes was 0.35". In downstream order the two vertical and two horizontal sense planes contained 3, 4, 4 and 5 wires. The chamber windows were 0.5 mil aluminum.

D2 was cylindrical with a 7" diameter aperture. Each wire plane

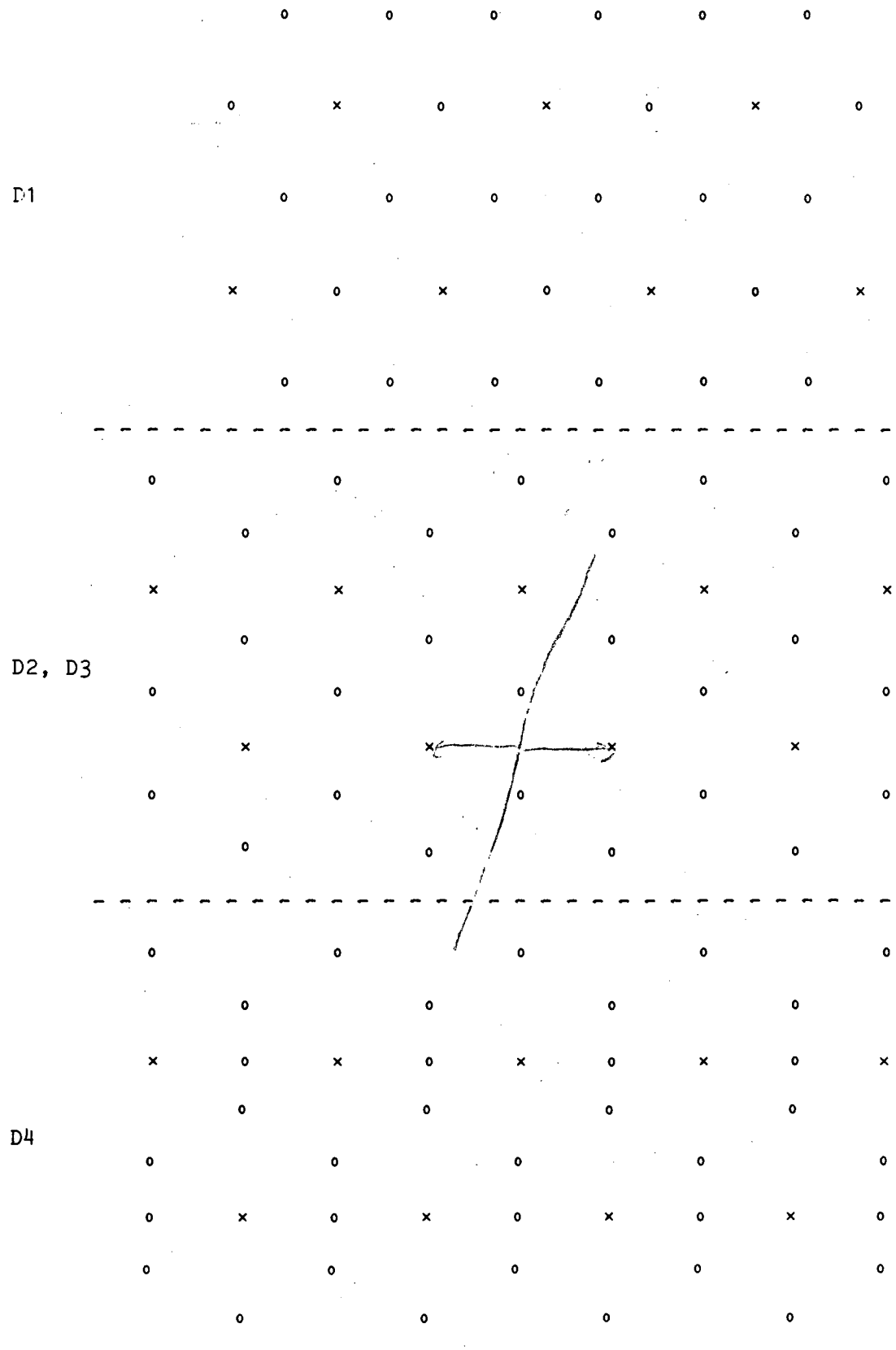

FIGURE (5.5). Drift-chamber cell geometries: × sense, ∘ field.

contained 8 wires spaced by 0.875". The separation between planes was 0.250". The shortest, and potentially least efficient, edge wire in each sense plane was 3 mil berylium-copper to render it completely inactive. The chamber windows were 0.5 mil aluminized mylar.

D3, located at the spectrometer entrance, consisted of 3 cylindrical chambers similar to D2 except that the aperture diameter was 11" and there were 12 wires per plane. D3 thus had a total of 6 vertical and 6 horizontal sense planes. The three chambers were separated, except for a narrow outer annulus, by 0.25 mil aluminized mylar windows.

D4, located at the spectrometer exit, had a rectangular aperture and contained a total of 6 planes of 32 vertical sense wires and 4 planes of 24 horizontal sense wires. The sense wire spacing was 24 mm.

The drift chamber gas was 92% methane/8% methylal. The chamber high voltage was applied to the sense wires of D1, and to the field wires of D2, D3 and D4. The operating voltages were +2900 V for D1, -2900 V for D3, and -3000 V for D2 and D4. The efficiencies of the sense planes was equalized by applying +260 V to the sense planes closest to the chamber windows of D2, D3, and D4.

Chamber signals above a 250 μV threshold were amplified by shielded LeCroy Model 4292 amplifier/discriminator cards mounted close to the chambers. Each chamber had a mean efficiency of at least 97% per plane except in Run 1, where D1 and D2 had mean efficiencies of 77% and 83% per plane respectively.

5.2.5 Scintillators

Scintillators S1 and S2 were 5 mil and 10 mil NE102A, respectively. Just upstream of S1 and downstream of S2 were veto scintillators V1 and V2 each of thickness 0.125" and inner diameter 1.5".

Scintillator S3, which covered the downstream area of drift chamber D4 consisted of 3 horizontal strips 39" long × 8" high × 0.375" thick.

S1, S2, V1, V2 and each strip of S3 were viewed from left and right by photomultipliers.

5.2.6 Stopping Targets

The muons were stopped in metal foils of >99.99% purity or in liquid He. Because foils of optimum thickness were unavailable the stopping targets were composite, consisting either of two back-to-back foils or a single foil preceded and followed by 1 mil aluminum foils.

The stopping target thicknesses are tabulated in Table (5.2). The compositions of targets having 1 mil Al foils are listed in upstream to downstream order. The target material calculated to be encountered by decay e^+ emitted by a mean range μ^+ is listed as 'residual thickness.' The residual thickness is also tabulated in terms of calculated μ^+ rms range straggling lengths. The effect of the 1% $\Delta p/p$ momentum bite has been included. Column (a) gives the number of straggling lengths to the downstream surface of the target. Column (b) gives the number of straggling lengths to the closest interface between foils, the + (-) sign indicating that mean range μ^+ stop beyond (before) the interface. Comparison of the calculated ranges with an experimental range curve taken in Run 2 indicates that the error on the number of straggling

Target	Run	Thickness (mg/cm^2)	Residual Thickness (mg/cm^2)	Residual Straggling Lengths (a)	(b)
Ag	1	2× 136.5 Total 273	96	8.1	3.4^+
Al	1,2,3	150	35	4.6	3.7^-
Al*	2	2× 142.5 Total 285	171	22.6	3.6^+
Au	1,2	6× 6.6 Al 193 Au 6.6 Al Total 239	53 Au 6.6 Al Total 60	4.1	3.4^-
Cu	2	6× 6.6 Al 110 Cu 6.6 Al Total 156	16 Cu 6.6 Al Total 23	2.5	1.6^-
Cu*	1,2	2× 111 Total 222	81	8.3	3.1^+
He	1	38 Al 150 He 38 He Total 226	86 He 38 Al Total 124	17.2	

Table (5.2)

lengths is unlikely to exceed ±0.5. The Ag and He targets were used only in Run 1. The residual thicknesses and straggling lengths for the other targets apply to Run 2. The change of proportional chamber gas from methane/methylal to magic gas for Run 2 and the presence of an additional proportional chamber upstream of the target in Run 3 alter the residual thicknesses. In particular for the Al, Au and Cu* targets in Run 1 the number of residual straggling lengths in column (a) should be reduced by 0.5, and reduced (increased) in column (b) for a - (+)

sign. For Run 3 the number of residual straggling lengths for the Al target should be increased by 0.1 in both columns (a) and (b).

Muons stopping in the air between or beyond the foils, or in the foils' oxidized surface layers are likely to form muonium and depolarize. Column (b) indicates that the Cu target is too thin. The other targets most likely to have thickness problems are Cu^* in Run 2 and Au in Run 1.

5.3 The Trigger

The essential features of the trigger logic as it existed in Run 1 are shown in Figure (5.6). Changes made to the logic in Runs 2 and 3 are described later in this section.

The inputs to the trigger logic were signals from the proportional chamber (P1-P3) cathodes, scintillators (S1-S3) and scintillator vetos (V1,V2) described in the preceding sections and shown in Figure (5.4). The notation P1U, P1V etc. denotes the cathodes associated with the wire planes measuring the horizontal and vertical track positions respectively. S1L and S1R etc. denotes photomultipliers viewing the scintillators from left and right repectively. The three horizontal scintillator strips of S3 were viewed from left and right, and in top to bottom order, by photomultipliers denoted by (G1,G4), (G2,G5), and (G3,G6).

Three triggers were used: the straight-through trigger for spectrometer momentum calibration with beam e^+; the μ-decay trigger for normal data taking; and the pulser trigger for online diagnostics such as checking ADC pedestals and searching for 'hot' or oscillating

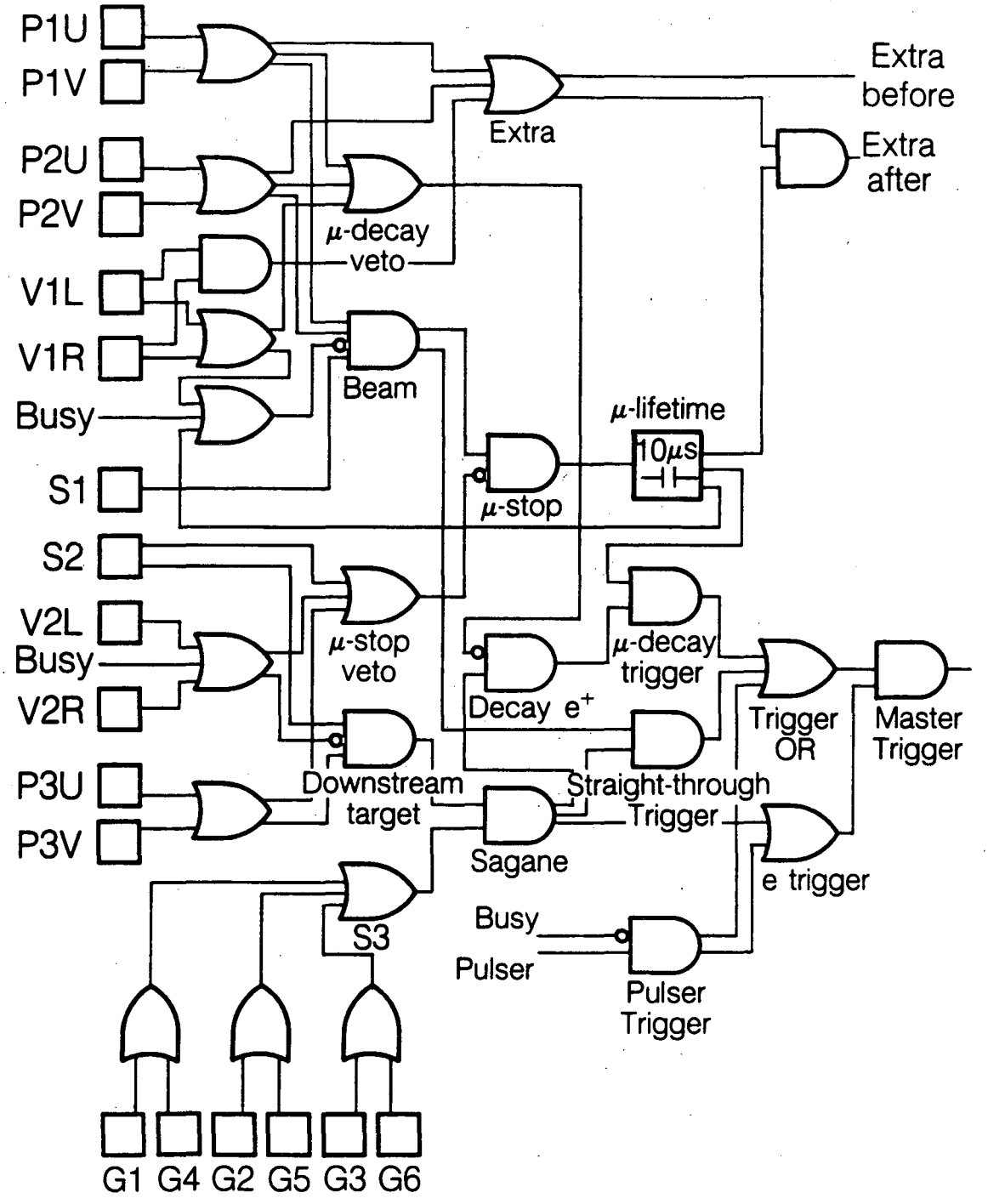

FIGURE (5.6). Essential features of the trigger logic during Run 1. Subsequent minor changes are described in the text.

wire-chamber channels.

Beam particles reaching the stopping target region have the signature

$$\text{Beam} = P1.P2.S1.\overline{V1}$$

Particles leaving the stopping target region and traversing the Sagane spectrometer have the signature

$$\text{Sagane} = P3.S2.S3.\overline{V2}$$

The straight—through trigger seeks to identify single beam particles which traverse the whole apparatus, and thus requires a coincidence between Beam and Sagane:

$$\text{Straight-through} = \text{Beam.Sagane}$$

The μ-decay trigger requires the signature of a μ-stop in delayed (0.1-10 μs) coincidence with that of a decay e^+. The μ-stop requirement that the beam particle stops in the stopping target is

$$\mu\text{-stop} = \text{Beam}.\overline{\mu\text{-stop veto}}$$

where $\overline{\mu\text{-stop veto}} = \overline{P3}.\overline{S2}.\overline{V2}$

The decay e^+ requirement that the outgoing downstream particle originates in the stopping target is

$$\text{Decay } e^+ = \text{Sagane}.\overline{\mu\text{-decay veto}}$$

where $\overline{\mu\text{-decay veto}} = \overline{P1}.\overline{P2}.\overline{V1}$

In Runs 2 and 3 P1 and P2 were removed from μ-decay veto and were replaced by the ability to make software cuts on events with P1 or P2

signals near the μ-decay time. The μ-stop time was provided by S1 and the μ-decay time by S2.

An important feature of the logic is the ability to tag, and later reject in software, almost all events where the decay e^+ could have originated from extra μ^+ rather than the μ-stop muon. This is crucial in the μSR mode of the experiment since extra μ^+ arriving at random times have correspondingly random precessed spin directions with respect to those of the μ-stop muons. They are therefore equivalent to an admixture of unpolarized muons and thus mimic right-handed current effects. The arrival of each beam particle sets a 10 μs latch. If a μ-stop occurs within the 10 μs latch the event is tagged as an 'extra-before'. In addition the arrival times of 'extra-after' beam particles arriving in the 10 μs following the μ-stop were recorded. A high incidence of false extra-after signals due to P1 and P2 after-pulsing following the μ-stop were largely eliminated by inserting dead-time notches in 'extra-after'. The resulting 'extra-after-1' and 'extra-after-2' were active from 0.6-10 μs and 0.85-10 μs in Run 1, and from 0.3-10 μs and 0.5-10 μs in Runs 2 and 3 respectively. The 1/4 OR of P1 and P2 cathode signals in Extra was replaced in Run 2 by either a 2/4 or a 3/4 coincidence, the choice depending on the proportional chamber cathode efficiencies. In Run 3 the role of P1 and P2 in Extra was assumed instead by the additional proportional chamber A between P1 and P2.

5.4 Data Acquisition

Event data was read from the CAMAC electronics into a circular buffer of a PDP-11/34 computer using the data acquisition program DA. The data was written to tape after several events were accumulated in the buffer. The program DA also supplied event information to the online analysis program MULTI.

Drift chamber time information was obtained using a LeCroy System 4290. The TDCs were operated in the common-stop mode, with the stop being provided by the trigger. Digitized time information was transferred to the memory unit which then sent a LAM signal to the PDP-11/34. In addition the PDP-11/34 read TDC and ADC information from the proportional chambers and scintillators; TDC information on the μ^+ arrival time relative to the cyclotron rf cycle, μ^+ lifetime, and extra-after times; latches set by proportional chamber wire signals and trigger logic elements; event scalers; and NMR-monitored fields in the beamline dipoles and spectrometer.

The CAMAC electronics were gated-off for 5 ms (reduced to 200 μs during Run 2) while the PDP-11/34 read the event and cleared the CAMAC electronics. In addition a computer 'busy' signal gated-off the trigger logic to prevent another trigger being received until the CAMAC electronics were cleared. It should be noted however that the extra-before latch remained operational during computer 'busy'.

Online information provided by MULTI included histograms of wire-chamber plane illuminations and multiplicities, the beam spot and angular distributions, the event time spectrum, scintillator and proportional chamber TDC and ADC distributions, and the proportion of events with extra-before and extra-after beam particles.

Typical event rates with 100 μA of protons incident on the production target were 60-70 Hz in the μSR mode and 25-30 Hz in the spin-held mode. The μSR data presented here were obtained from 1.5×10^7 raw triggers. The cuts described in Chapter 6 retained 5.6% of the events.

Chapter 6

Event Reconstruction

6.1 Wire Chamber Alignment

The relative positions of the wire chamber planes transverse to the beam direction were determined from the mean residuals of reconstructed beam e^+ tracks. Straight track segments were fitted to hits in the horizontal and vertical wire planes of the chamber groups P1, P2, P3, D1 and D2; D3; and D4 [Figure (5.4)] with the solenoid off and no stopping target between P2 and P3. Alignment of wire-chambers P1-D2 as a single unit ensured that the μ^+ and e^+ polar angles θ_μ and θ_e were measured relative to a common axis. The chamber planes were thereby aligned to within 50 μm, while the rms residuals were typically 300 μm in the drift chambers.

6.2 Muon Track Reconstruction

Straight muon tracks were fitted to hits in proportional chambers P1 and P2. A valid hit was defined to be a signal from at least one, but no more than three, adjacent wires in the same plane. The track was assumed to pass through the center of the hit pattern. One and only one hit was permitted in each plane of P1. One plane of P2 was also required to have one and only one hit, while either one or two hits were allowed in the other plane. The correct muon track was assumed to be the one agreeing most closely with the outgoing positron track in stopping target position. Events with reconstructed $\cos\theta_\mu<0.99$ with respect to the beam direction were rejected in the analysis.

6.3 Positron Track Reconstruction

Straight e^+ track segments were fitted separately to hits in the horizontal and vertical projections of the wire-chamber plane groups: P3, D1, D2; D3; and D4. Resolution of the left-right ambiguity associated with each drift chamber hit relied on the staggered cells of adjacent sense planes. The first sought track segments of acceptable straightness and slope were those with a hit in each of the constituent wire-chamber sense planes. In segments where such tracks were not found the number of sense planes required to have a hit on the track was progressively decreased. If more than one track was found with hits in the same number of planes the track with the best chi-square was accepted. Tracks in all six segments were found in 99% of the triggers.

To guard against fake tracks from spurious hits, cuts were made on the total number of hits in the wire chamber groups. The number of hits in the 10 planes of P3-D2 and in the 10 planes of D4 were each required to be ≤ 18; and in the 12 planes of D3 to be ≤ 22. Furthermore, the horizontal and vertical track projections in P3-D2 were each required to have hits in at least 3 of the 5 constituent planes; in D3 to have hits in at least 4 of the 6 planes horizontally and 3 of the 6 planes vertically; and in D4 to have hits in at least 4 of the 6 planes horizontally and 3 of the 4 planes vertically. In addition only one hit, as defined in section (6.2), was permitted in each plane of P3.

The e^+ tracks through P3-D2 are not straight because of the longitudinal field in the downstream section of the solenoid. The P3-D2 track space points were refitted to a curved track based on the first-order optics of cylindrically symmetric fields described in Appendix A. The best fit tracks were obtained using field values 95% of

those in Table (5.1).

Approximate space:time relations were obtained by integrating the drift-time distributions of cells almost uniformly illuminated by decay e^+ in μSR runs with the downstream solenoid off. The e^+ curved track residuals were used to dynamically fine-tune the space:time relation for each drift chamber plane in each run. The space:time relations for the various planes were stored as arrays of drift distances for each of 512 1-nsec wide drift-time bins. The first 3000 events on each data tape, typically containing 1.2×10^5 events, were used for the fine-tuning after which the tape was rewound and the analysis restarted. If for the i'th drift-time bin a residual r was obtained, the drift distances for the i-8 to i+8 time bins were changed by

$$\Delta(i\pm k) = (\text{sign})rW[9-\max(k,1)]/200$$

for $0 \leq i\pm k \leq 512$ where $0 \leq k \leq 8$,

$$W = \begin{cases} 1.0 \text{ if } |r| < 0.1 \text{ cm} \\ 0.5 \text{ if } 0.1 \text{ cm} < |r| < 0.2 \text{ cm} \\ 0 \text{ if } |r| > 0.2 \text{ cm} \end{cases}$$

and

$$\text{sign} = \begin{cases} +1 \text{ if track coordinate} > \text{wire coordinate} \\ -1 \text{ if track coordinate} < \text{wire coordinate} \end{cases}$$

The changes are therefore largest for the i'th and i±1'th drift-time bins and then decrease linearly away from the i'th bin. The procedure converges after about 1500 events.

The drift-chamber rms residuals are shown in Table (6.1). The larger rms residual in the D1 vertical projection is not well understood. The 3% of events with e^+ tracks in P3-D2 with reduced $\chi^2>20$ were rejected.

Drift Chamber	RMS Residual (μm)
D1 (horizontal)	325
(vertical)	600
D2	325
D3	250
D4	250

Table (6.1)

The e^+ track segments fitted in P3-D2; D3; and D4 were required to satisfy several continuity criteria. First-order optics (Appendix A) extrapolations of the tracks in P3-D2 and D3 into the solenoid bore were required to have both radial agreement, ΔR, and azimuthal agreement, $R\Delta\phi$, <2 cm. Extrapolations of the tracks in D3 and D4 into the spectrometer were required to agree to within 4 cm in both vertical position and impact parameter with respect to the magnet axis, and to agree to within 0.08 in vertical slope. The horizontal position of the e^+ track determined by the S3 scintillator pair time difference was required to agree with the extrapolated D4 track to within 10 cm. Events in which more than one of the three S3 scintillator pairs fired were rejected.

Aperture cuts were made in the solenoid and spectrometer. Events with e^+ emitted from the stopping target at radii >1.8 cm or with $\cos\theta_e<0.975$ were rejected. The e^+ track radial position at the exit of D2 (aperture radius 8.86 cm) was required to be <8.5 cm. The maximum track radial position in the solenoid bore (aperture radius 11.1 cm)

was required to be <10 cm. The presence of gas lines (Runs 2 and 3) and a helium bag (Run 2) in addition to D2 signal cables within the solenoid bore made necessary tighter radial cuts of 8.5 cm in Run 2 and 9.5 cm in Run 3. The vertical position of the track at the spectrometer exit (vertical aperture ±16.8 cm) was required to be within ±15.5 cm of the median plane. Additional vertical cuts were made at ±(6.4-9.4) cm around two horizontal ribs supporting the vacuum window between the spectrometer and D4.

6.4 Extra Muons

Most e^+ originating not from the decay of the observed stopped μ^+, but from the decay of another μ^+ were eliminated by rejecting events with 'extra-before' or 'extra-after-1' [section (5.3)] beam particles. The small fraction of events with e^+ originating from untagged extra μ^+ was reduced by requiring continuity between the e^+ and μ^+ tracks at the stopping target. Requiring track separations <4.5 mm rejected 78% of uncorrelated μ^+-e^+ events and 14% of correlated μ^+-e^+ events.

Positrons from extra μ^+ with random arrival times constitute a flat background to the observed μ^+ decay time spectrum. A comparison of the background levels before and after the cuts described above therefore provides a measure of the efficiency of those cuts. Figure (4.1) shows the Run 2 spin-held data time spectrum after the cuts were made. The fitted background of 1.3±9.8 per time bin corresponds to $(3\pm22)\times10^{-5}$ of the time t=0 rate. Before making the cuts a spectrum with a similar number of events at early times had a background of about 1600 per time bin, or 3.6×10^{-2} of the t=0 rate.

6.5 Momentum Reconstruction

The momenta of e^+ passing through the horizontally focusing cylindrical dipole spectrometer were obtained to first order from the sum of the horizontal coordinates at the conjugate foci. A nominal x=1 calibration point was provided by the sharp edge at the endpoint of the μSR data. The spectrometer momentum dispersion was measured to be approximately 1.07%/cm using e^+ beams obtained at several settings of the beamline elements.

Empirical ad hoc corrections were introduced to make the reconstructed μSR data endpoint independent of impact parameter with respect to the magnet axis, mean squared (vertical) deviation from the median plane, and vertical position at the spectrometer exit. This procedure was repeated at several spectrometer settings to obtain corrections appropriate for x=1 at the standard spectrometer setting. An additional correction eliminated a residual correlation between $\cos\theta_e$ and the reconstructed endpoint, which amounted to $\Delta x=0.001$ between the $\cos\theta_e=0.975$ and $\cos\theta_e=1$ endpoints. The resulting momentum resolution was better than 0.2% rms.

The spectrometer was re-calibrated with e^+ beams obtained at many beamline settings. In Run 3 two sets of calibration data were taken with the spectrometer at 42%, 50%, 60%, 72%, 86%, and 100% of its standard setting, while in Runs 1 and 2 only the standard setting was used. After allowing for a most probable e^+ energy loss of 1.75 MeV-cm^2/g in the material upstream of the spectrometer, the e^+ momentum was assumed to be proportional to the beamline dipole settings. Any apparent non-linearities or offsets were attributed to the spectrometer. With the coefficients of the linear and quadratic

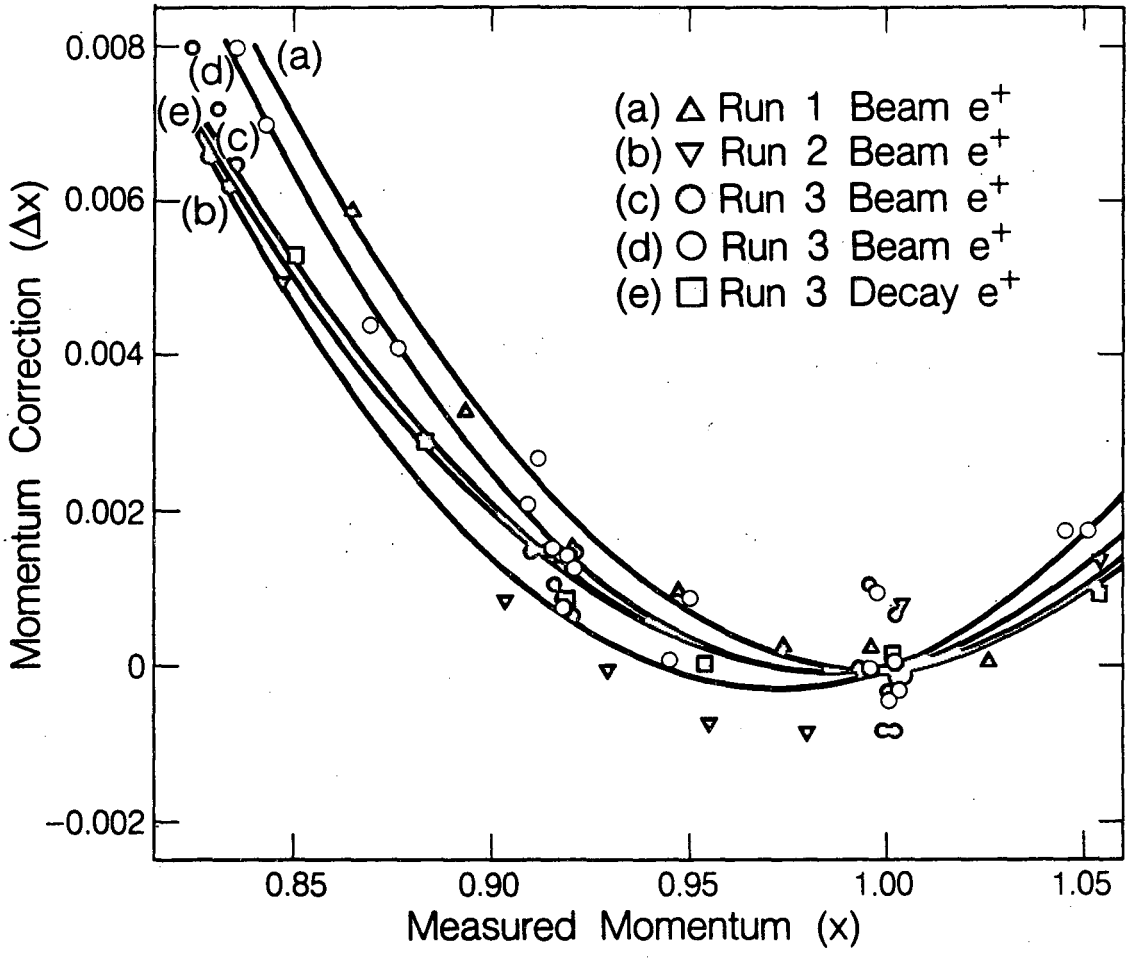

XBL 858-11672

FIGURE (6.1). Momentum correction versus nominal measured momentum required to yield linear momentum scale with x=1 unchanged. The curves are quadratic fits to the points. Additional points with x>1.05 in calibrations (c)-(e) were included when determining curves (c)-(e).

dispersion terms allowed to vary linearly with spectrometer setting it was found that:

(i) the effective field integral for particles with a 98° bend angle at the various spectrometer settings increased (0.22±0.02)% more rapidly than indicated by the NMR probe in the central field region;

(ii) the linear dispersion increased by (1.1±0.2)% between the spectrometer 42% and 100% settings;

(iii) the quadratic dispersion was consistent with being constant.

An independent calibration, incorporating the above spectrometer behavior, was performed using the reconstructed μSR data endpoints at several spectrometer settings. The result was consistent with the beamline calibrations, thereby indicating that the beamline did not deviate appreciably from the assumed linear behavior.

The calibration data displayed in Figure (6.1) shows the correction required at the standard spectrometer setting to convert the original momentum scale to a linear momentum scale leaving the nominal x=1 point unchanged. The mean of the five curves in Figure (6.1) was taken to be the required momentum correction.

Conversion of the linear momentum scale to an absolute momentum scale is illustrated by the following exmaple. The endpoint of the Run 3 Al target data was at x=1.0030 on the linear momentum scale. Allowing for uniform energy-loss in the material upstream of the spectrometer the expected endpoint is at x=0.9916 on the absolute momentum scale. Thus a factor of 0.9886 converts the linear momentum scale to the absolute scale. For data fitting, uniform energy-loss was added back on to superimpose the data on the energy-loss straggled theoretical spectra (Appendix B). Since the calibration beam e^+ and the decay e^+

traverse similar amounts of material, the likely error in estimating the uniform energy-loss has negligible effect on the momentum ultimately attributed to the decay e^+.

The 1σ possible systematic error in the momentum calibration was taken to be the standard deviation of the corrections given by the five curves in Figure (6.1). They are shown in Table (6.2) for the centers of the momentum bins used in the data analysis.

Momentum x	Standard Deviation in Correction Δx
0.89	0.00066
0.91	0.00053
0.93	0.00040
0.95	0.00029
0.97	0.00017
0.99	0.00006

Table (6.2)

The above momentum calibration systematic errors are to be added in quadrature with a likely error of ± 0.0001 in determining the μSR data endpoint.

Events with $x<0.88$ ($x<0.92$ in Run 1), which have lower statistical power and larger possible systematic errors in momentum reconstruction, were rejected in the analysis.

Chapter 7

Data Analysis

7.1 Overview

The μSR data in 0.04 μs time bins and six 0.02 wide x bins were fitted to

$$N(t) = N_0[\int C(x)dx + P_\mu A(\tilde{x})G(t)\langle\cos\theta\rangle_t \int D(x)dx]\exp(-t/\tau_\mu) \qquad (7.1)$$

Here C(x) and D(x) are the angle independent and dependent parts respectively of the radiatively corrected (V-A) differential decay rate [section (3.3)] smeared by the e^+ energy-loss straggling (Appendix B) and by a sum of Gaussian momentum resolution functions.

The fit parameters common to all x bins were the μ^+ mean-life τ_μ, the μ^+ spin precession frequency ω and the initial time t_0 incorporated into $\langle\cos\theta\rangle_t$, and the two (one) parameters of the Kubo-Tomita (Gaussian) spin relaxation function G(t) [section (4.4)]. The other fit parameters were the normalizations N_0 and the asymmetries $P_\mu A(\tilde{x})$ relative to the (V-A) prediction for each of the six x bins.

Both the spin-held [Figure (4.1)] and μSR data [Figure (4.3)] are consistent with zero background. Since any fitted positive background would increase the apparent decay asymmetry and thus strengthen the limits on right-handed currents, the μSR data background was fixed to zero. It was checked that the spin-held data exhibited a consistent exponential decay rate over the time range used in the μSR fits.

The maximum likelihood poisson statistics χ^2, defined by

$$\chi^2 = 2\sum_i [e_i - o_i + o_i \ell n(o_i/e_i)]$$

where o_i and e_i are the observed and expected number of events respectively in the i'th bin, was minimized using a double precision version of the MINUIT minimization program.

7.2 Positron Momentum Spectra

Positrons leaving the stopping target and traversing the other material ($\approx$200 mg/cm^2) upstream of the spectrometer are energy-loss straggled to lower momenta where the unstraggled decay asymmetry is less. The e^+ energy-loss straggling therefore increases the apparent asymmetry below the endpoint. Figure (7.1) shows the μSR data momentum spectra for the Al and Al* targets. The greater energy-loss straggling is apparent in the more rounded shoulder in the thicker Al* target data.

The radiatively corrected (V-A) μ^+ differential decay rate [section (3.3)] was evaluated for $\cos\theta$=-1,0,1 at momentum intervals of Δx=0.0004. These three momentum spectra were energy-loss straggled for both ionization and bremsstrahlung using the formalism of Tsai[49] as described in Appendix B.

The three straggled momentum spectra were then smeared by a sum of three Gaussian momentum resolution functions with standard deviations σ, 2σ, and 3σ determined by fitting the time-average μSR data to a straggled unpolarized ($\cos\theta$=0) momentum spectrum.

The integral of C(x) [equation (7.1)] for each x bin was evaluated by summing the appropriate smeared and straggled decay rate points of the $\cos\theta$=0 spectrum. Similarly the integral of D(x) for each x bin was evaluated by subtracting the sum of the $\cos\theta$=-1 decay rate points from the sum of the $\cos\theta$=1 decay rate points and then dividing by 2.

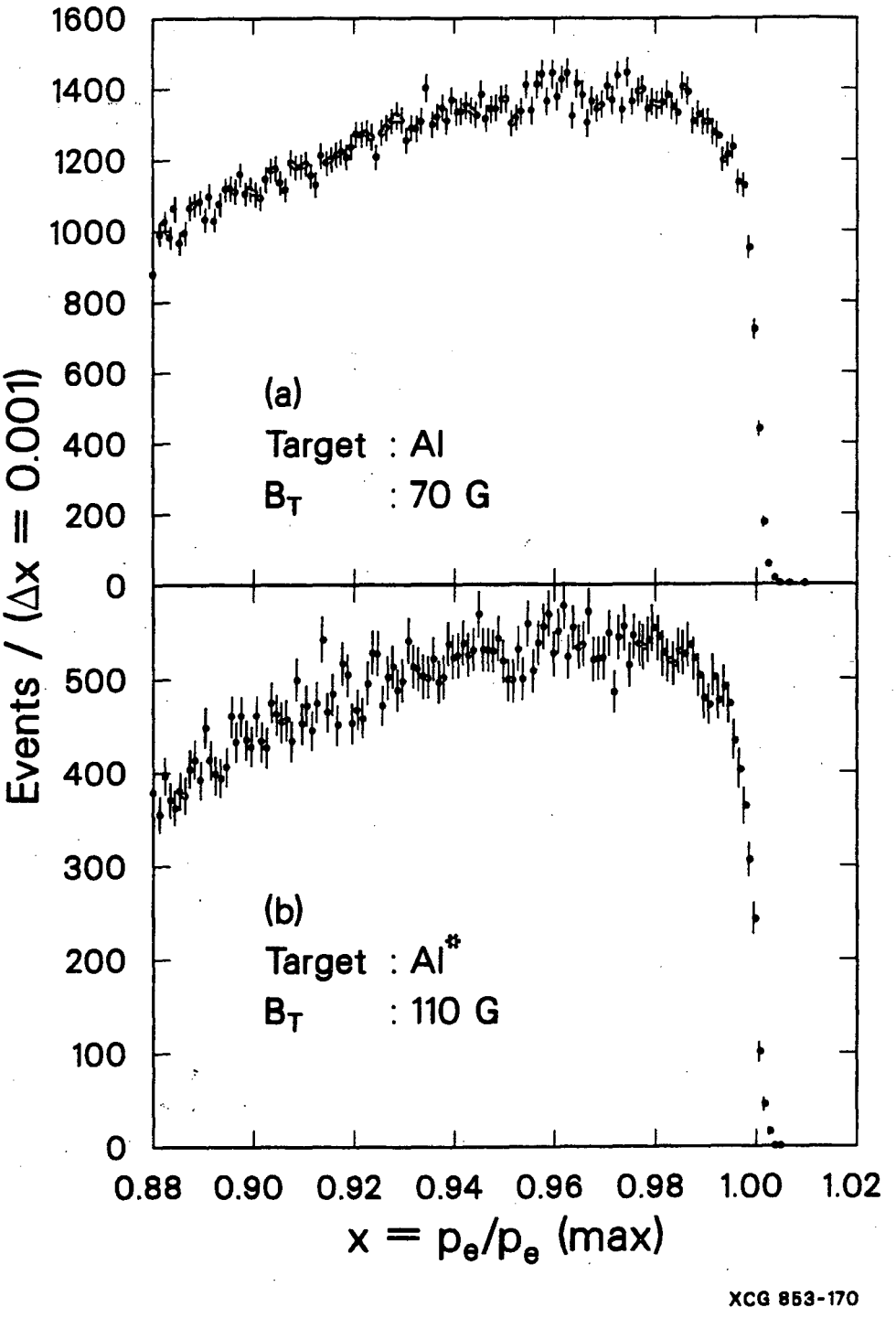

FIGURE (7.1). Momentum spectra of μSR data with (a) Al target and (b) Al^* target. Greater energy-loss straggling in the thicker Al^* target results in a less sharp edge.

7.3 The Positron Angular Acceptance

The angular acceptance of the apparatus for decay e^+ in each x bin is given by the observed $\hat{p}_e$ distribution observed in time-average isotropic μSR data. In practice one selects a time window which maximizes the number of decay e^+ originating from μ^+ with precessed spin directions averaging to zero polarization. The μ^+ polarization directions $\hat{P}_\mu$, assumed to lie along $-\hat{p}_\mu$ initially, precess with frequency $\omega=g_\mu eB_T/2m_\mu c$. The $\langle\cos\theta\rangle_t$ of equation (7.1) is given at any time t by the mean $\cos\theta$ between the $\hat{p}_e$ and precessing $\hat{P}_\mu$ distributions. If the distributions contain N events

$$\langle\cos\theta\rangle_t = (1/N^2)\sum_{ij}\sum\cos\theta_{ij}(t) \qquad (7.2)$$

where $\cos\theta_{ij}(t) = (\sin\theta_\mu\cos\phi_\mu)_i(\sin\theta_e\cos\phi_e)_j$

$$+[(\cos\theta_\mu)_i\sin\omega t + (\sin\theta_\mu\sin\phi_\mu)_i\cos\omega t](\sin\theta_e\sin\phi_e)_j$$

$$+[(\cos\theta_\mu)_i\cos\omega t - (\sin\theta_\mu\sin\phi_\mu)_i\sin\omega t](\cos\theta_e)_j$$

Note that if azimuthal symmetry is present equation (7.2) reduces to

$$\langle\cos\theta\rangle_t = \langle\cos\theta_\mu\rangle\langle\cos\theta_e\rangle\cos\omega t \qquad (7.3)$$

Since the precise precession frequency is unknown until the fit is complete, $\langle\cos\theta\rangle_\psi$ is pre-calculated instead for 1° steps of the precession angle $\psi=\omega t$ using equation (7.2). As the fit proceeds variation of the parameters ω and t_o causes the time bins to correspond to different ranges of the 1° precession angle steps. The $\langle\cos\theta\rangle_t$ for a given time bin is then the mean $\langle\cos\theta\rangle_\psi$, weighted for μ^+ decay within the bin, of the precession angle steps or fractions thereof corresponding to that time bin. It should be noted that the time-zero

parameter t_o is well-defined because the observed $\hat{p}_\mu$, and hence $\hat{P}_\mu$, distribution defines the time-zero phase of the μSR signal.

Since the procedure described above is applied to the data in each fit the analysis should be immune to any acceptance changes due, for example, to variations in the μ^+ beam phase space or detector efficiencies provided the reconstructed quantities for any given event are independent of detector efficiency.

7.4 Positron Momentum Acceptance

The e^+ momentum acceptance is a maximum near x=1 and decreases to about 60% of maximum at x=0.88. Approximating the momentum acceptance changes as linear within each of the six x bins allows simple acceptance corrections to be made.

For each x bin the mean x of time-average P_μ=0 μSR data [section (7.3)] is calculated and compared with the corresponding mean x of the theoretical smeared and straggled unpolarized ($\cos\theta$=0) momentum spectrum of section (7.2). If the data mean x lies $\langle\Delta x_d\rangle$ from the bin center while the theoretical mean x is at $\langle\Delta x_t\rangle$, the acceptance correction factor multiplying the theoretical spectra Δx from the bin center is $f(\Delta x) = 1+k\Delta x$ where $k = 3\times10^4(\langle\Delta x_d\rangle-\langle\Delta x_t\rangle)$. After applying such corrections to each x bin of the smeared and straggled $\cos\theta$=-1,0,1 momentum spectra the integrals of C(x) and D(x) are calculated as described in section (7.2).

7.5 Monte Carlo Tests

The data fitting method described in the preceding sections was tested using a simple Monte Carlo event generator to produce (V-A) 'events' according to the radiatively corrected decay rate of section (3.3). The fitted asymmetry normalized to that expected for (V-A) decay, $P_\mu A(\tilde{x})$, should be consistent with unity.

Two 'data' sets were generated with different input $\cos\theta_\mu$, $\cos\theta_e$, and momentum acceptance distributions. Each 'data' set contained 2.0×10^6 'events' compared to 0.59×10^6 real events contributing to the final experimental results. The first 'data' set had constant input $\cos\theta_\mu$ (0.99-1.00), $\cos\theta_e$ (0.975-1.000) and x (0.88-1.00) acceptance distributions, and a μ^+ spin precession frequency corresponding to B_T=70-G. For the second 'data' set, generated for B_T=110-G, the input $\cos\theta_\mu$ distribution decreased linearly to zero at $\cos\theta_\mu$=0.99; the $\cos\theta_e$ distribution decreased linearly by 50% from $\cos\theta_e$=1→0.975; and the x acceptance decreased linearly by 40% from x=1→0.88. In both cases the input Gaussian spin relaxation function G(t) reduced the μSR signal amplitude at t=10 μs to 70% of its t=0 value, which was the largest damping observed in the metal target data. No 'events' were generated for t<0.12 μs, again imitating the real data. No apparatus effects were included other than those implicit in the input $\cos\theta_\mu$, $\cos\theta_e$, and x acceptance distributions. The integrals of C(x) and D(x) in equation (7.1) were therefore determined from the momentum spectra of section (3.3) without the energy-loss straggling and smearing described in section (7.2).

The fitted $P_\mu A(\tilde{x})$ averaged over x bins for the two 'data' sets were 0.9996±0.0010 and 0.9998±0.0009. The relative consistency of these

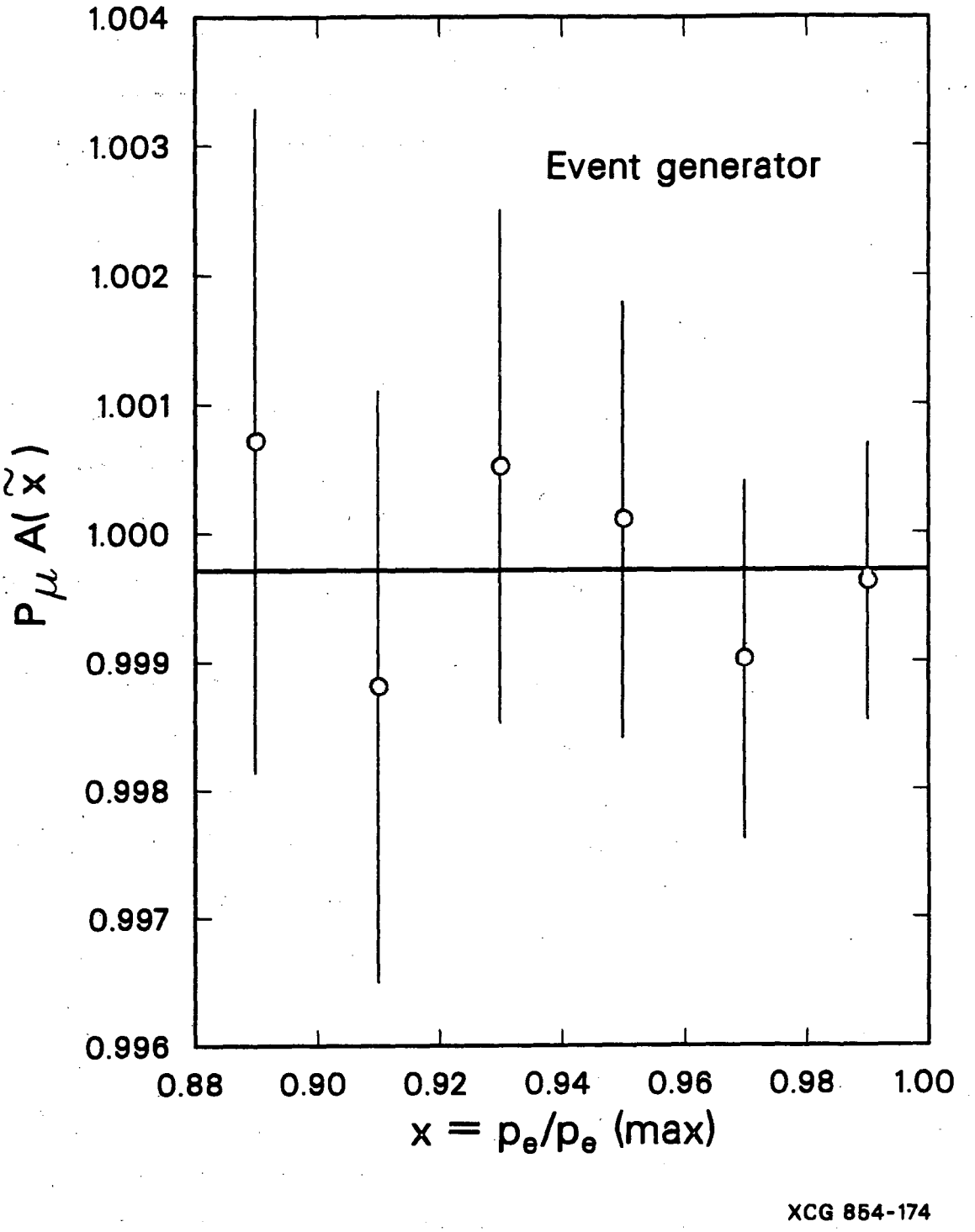

FIGURE (7.2). Fitted $P_\mu A(\tilde{x})$ for 4.0×10^6 Monte Carlo events generated with $P_\mu A(\tilde{x})=1$. The weighted mean fitted $P_\mu A(\tilde{x})=0.9997\pm0.0007$.

values, and of the combined value 0.9997±0.0007 with the input $P_\mu A(\tilde{x})$ of unity at a statistical level 6.7 times that of the real data gives confidence in the fitting procedure. The combined fitted $P_\mu A(\tilde{x})$ for each x bin are plotted in Figure (7.2).

7.6 Data Fitting Results

The results of the various fits described in this section are tabulated in Tables (C.1) and (C.2) of Appendix C. All runs except those with some known deficiency were included in the fits. For example, several runs were rejected because of partial deflation of the helium bag (present only in Run 2) between drift-chambers D2 and D3.

The final results are based on the normalized asymmetries $P_\mu A(\tilde{x})$ fitted to each x bin for the various stopping targets and B_T settings. The results of these fits are shown in Table (C.1) for both Gaussian and Kubo-Tomita μ^+ spin relaxation functions G(t). The fitted initial depolarization (12.4±0.9%) in liquid He may be due to μ^+-e^- spin exchange processes during or shortly after μ^+ thermalization. The fitted $P_\mu A(\tilde{x})$ averaged over x bins for each metal target data set are displayed in Figure (7.3). The Run 2 Cu and Cu* target data exhibits significantly smaller $P_\mu A(\tilde{x})$ [4.8σ for Gaussian G(t)] than the other metal target data. Muon range-straggling calculations [Table (5.2)] show that the 156 mg/cm^2 Cu target was too thin to stop the μ^+ well within the target, while the 222 mg/cm^2 Cu* target, composed of two foils, may have suffered from μ^+ stopping between the foils.

The $P_\mu A(\tilde{x})$ for all x bins and targets should be consistent if the momentum calibration is correct, if the decay parameters ρ and δ have

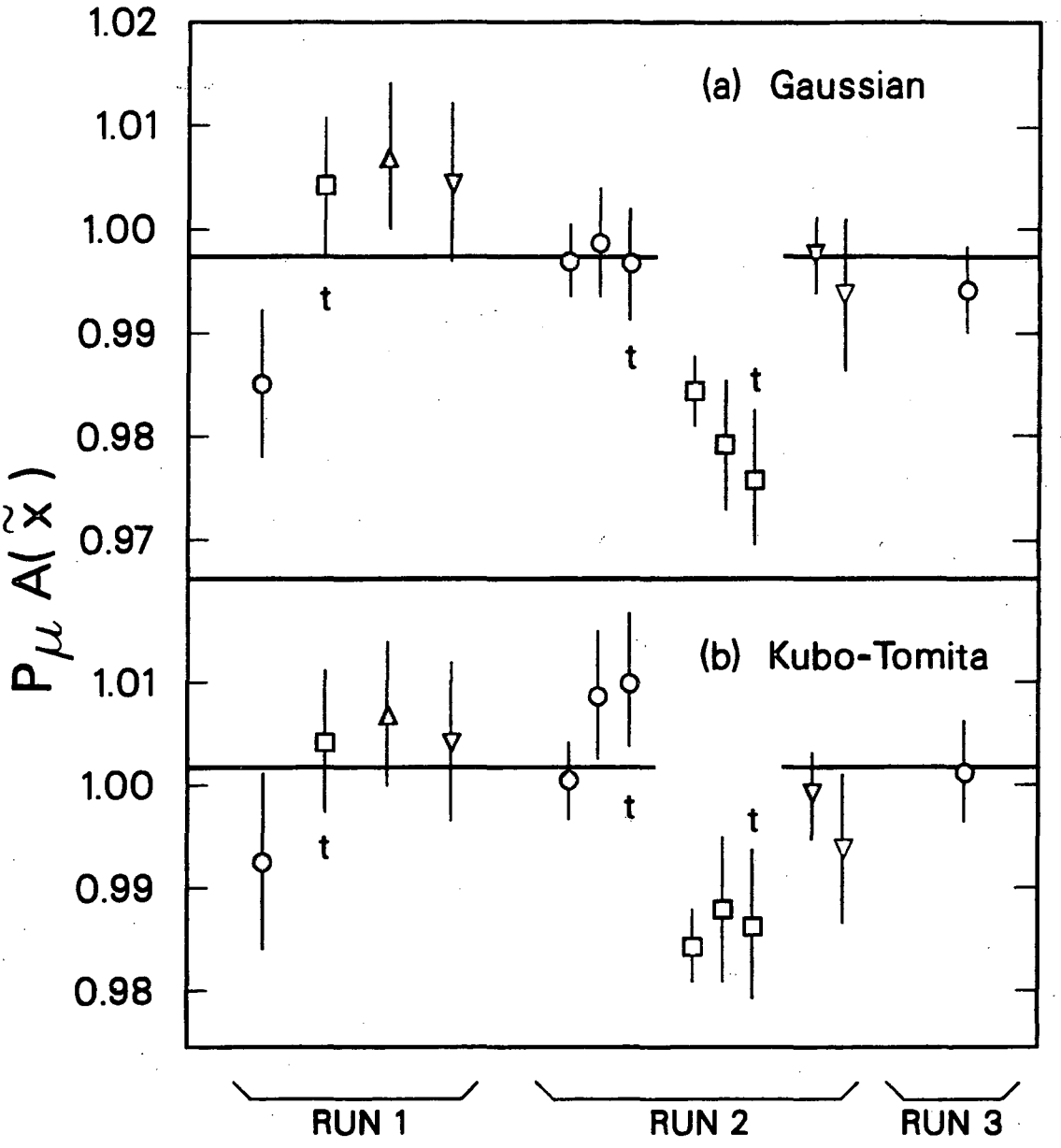

FIGURE (7.3). Weighted mean fitted $P_\mu A(\tilde{x})$ for the metal target data sets with (a) Gaussian and (b) Kubo-Tomita μ^+ spin relaxation forms. Targets are Al (circles), Cu (squares), Ag (triangles) and Au (inverted triangles). Thick targets Al* and Cu* are marked "t". Spin precessing fields are B_T=70-G (closed symbols) and B_T=110-G (open symbols).

their (V±A) values [see equation (3.3)], and if the targets do not produce differing initial μ^+ depolarizations. Excluding the He and Run 2 Cu and Cu* data, the remaining 52 $P_\mu A(\tilde{x})$ values for Gaussian G(t) have a mean of 0.9973±0.0016 with χ^2_{51}=63.5 (C.L.=11%). Inclusion of Run 2 Cu and Cu* yields a mean $P_\mu A(\tilde{x})$ = 0.9934±0.0014 with χ^2_{69}=106.7 (C.L.=0.2%). The final result is based on the metal target data sets excluding Run 2 Cu and Cu*. The Run 1 Cu* data set was retained because there the μ^+ stopped 0.5 rms straggling lengths deeper in the second foil due to the proportional chamber gas being methane/methylal instead of magic gas. The x bin averaged $P_\mu A(\tilde{x})$ in Figure (7.3) for the ten remaining data sets are statistically consistent with χ^2_9=8.4 (C.L.=49%). Figure (7.4) shows the $P_\mu A(\tilde{x})$, averaged over the remaining metal targets, for each x bin with the 1σ possible momentum calibration systematic error added in quadrature to the statistical error. With only the statistical errors the points have χ^2_5=7.5 (C.L.=19%). The line is the best fit using the world average δ and ρ values [section (9.4)].

Table (C.1) shows that for Run 1 Ag, Au, and Cu*, and for Run 2 Au (70-G and 110-G) the Kubo-Tomita G(t) fits did not have χ^2 less than the Gaussian G(t) fits. Since for these data sets the Kubo-Tomita G(t) closely approaches its Gaussian limit the true $P_\mu A(\tilde{x})$ may be less than that obtained with Gaussian G(t). Refitting with a form $G(t)=\exp(-\alpha t^\beta)$ yielded β>2, lower χ^2, and lower $P_\mu A(\tilde{x})$ for Run 1 Ag, Au, and Cu* but not for Run 2 Au. For the 10 metal targets and Kubo-Tomita G(t) the mean $P_\mu A(\tilde{x})$=1.0020±0.0018. When the lower values for Run 1 Ag, Au, and Cu* are used instead the mean $P_\mu A(\tilde{x})$=1.0013±0.0018, which is still significantly larger than the Gaussian G(t) mean $P_\mu A(\tilde{x})$=0.9973±0.0016. Thus the global use of Gaussian G(t) appears to have provided a lower

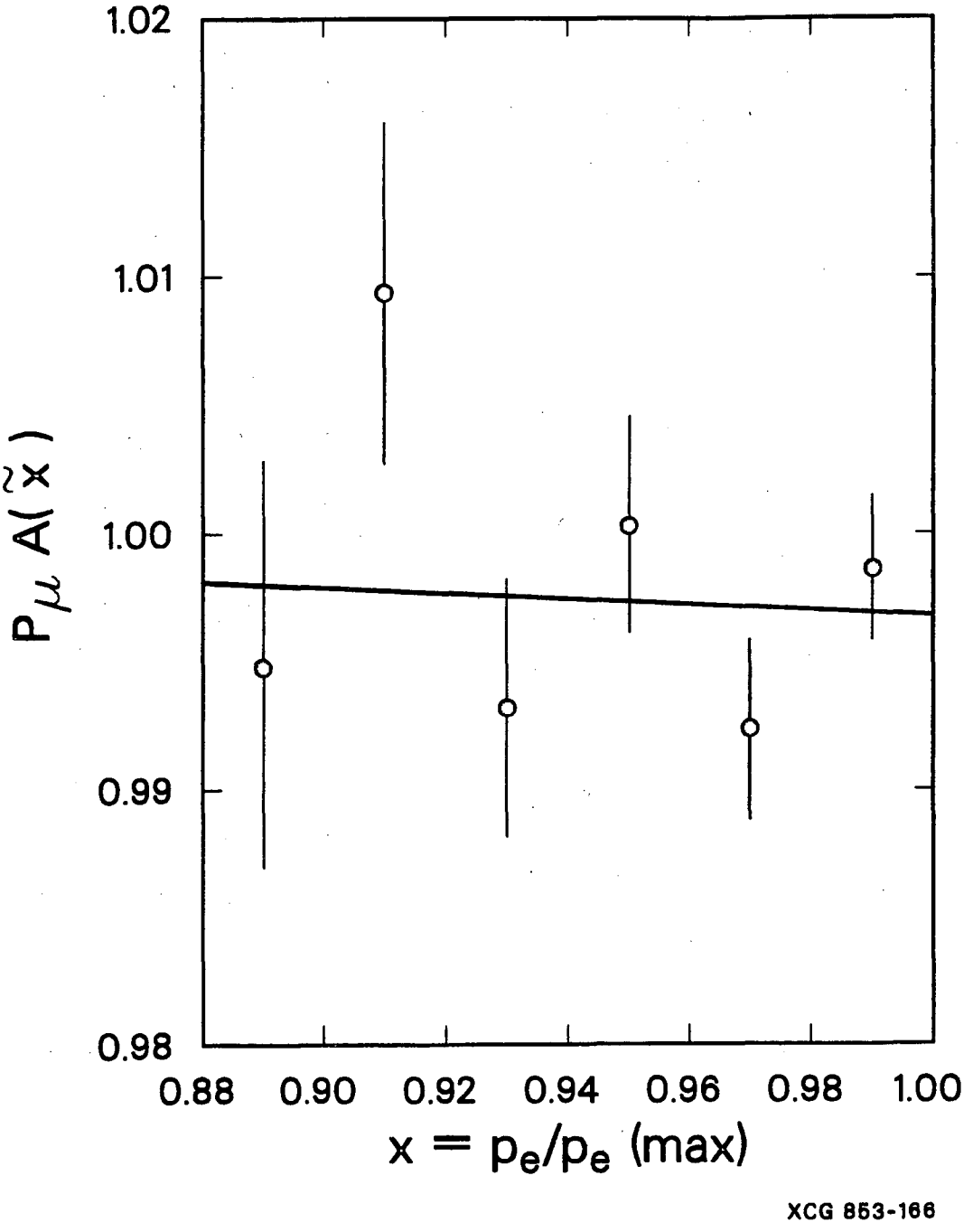

FIGURE (7.4). Weighted mean fitted $P_\mu A(\tilde{x})$ in each x bin for metal targets excluding Run 2 Cu and Cu*. Error bars are statistical errors added in quadrature to the possible momentum calibration systematic error. The fitted line assumes the world average values of δ and ρ.

bound on $P_\mu A(\tilde{x})$.

Three auxiliary fits were made to each data set. Firstly, with G(t) fixed to unity a common $P_\mu A(\tilde{x})G(t)$ was fitted to the x bins for each μ^+ spin precession period. The fitted $P_\mu A(\tilde{x})G(t)$ tabulated in Table (C.1) and plotted in Figure (7.5) versus the time-range midpoint indicate the actual form of G(t). The curves in Figure (7.5) correspond to the Gaussian G(t) obtained in the primary fits. The aluminum target data, which has a significantly better χ^2 for Kubo-Tomita G(t) is seen to exhibit an actual G(t) far closer to Gaussian than exponential. The μSR signal damping in Al is much larger than observed in other experiments, and may be due to μ^+ trapping in cracks or other defects in the cold-rolled Al foils.

Secondly, for each data set a common $P_\mu A(\tilde{x})$ was fitted to the x bins for each of five 0.005 wide $\cos\theta_e$ bins with a Gaussian G(t) fixed to that obtained in the primary fit. The results are shown in Table (C.1). The 50 measurements in the data sets contributing to the final results have $\chi^2_{49}=52.4$ (C.L.=33%). The combined data in Figure (7.6) are consistent ($\chi^2_4=1.4$, C.L.≈85%) with fitted $P_\mu A(\tilde{x})$ independent of reconstructed $\cos\theta_e$.

Thirdly, a common $P_\mu A(\tilde{x})$ was fitted to the x bins for individual runs with the Gaussian G(t) obtained in the primary fit for the corresponding data set. The results are tabulated in Table (C.2). Figure (7.7) displays the results as a histogram of the deviation of the individual run $P_\mu A(\tilde{x})$ from the data set mean in units of the individual run statistical error. The histogram is consistent ($\chi^2_{14}=11.6$, C.L.≈60%) with a normal distribution truncated at $\pm 4\sigma$. There is no evidence for 'bad' runs apart from those rejected for known

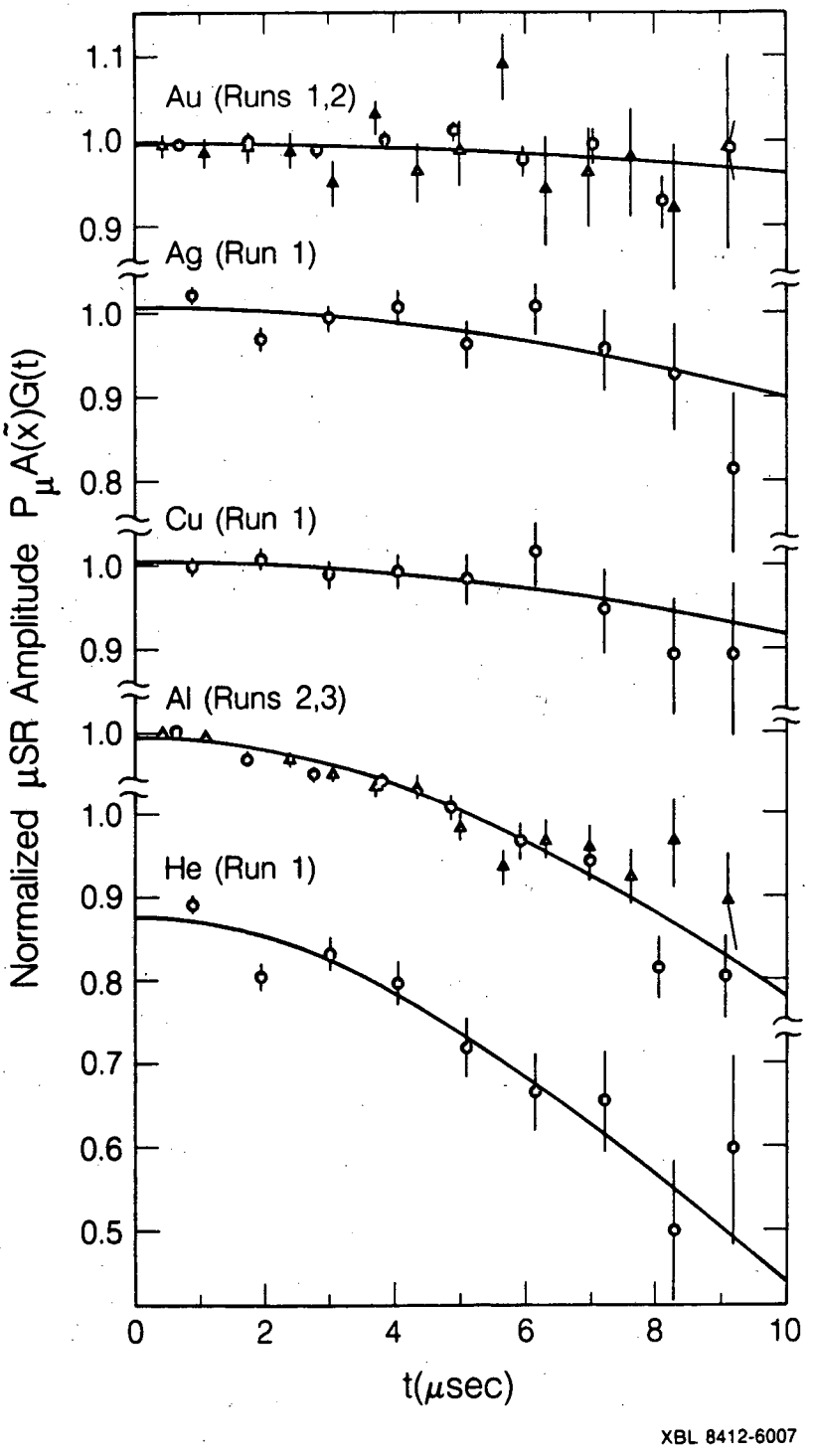

FIGURE (7.5). Values of $P_\mu A(\tilde{x})G(t)$ for each μ^+ spin precession cycle with B_T=70-G (circles) and B_T=110-G (triangles). The curves assume Gaussian μ^+ spin relaxation functions G(t).

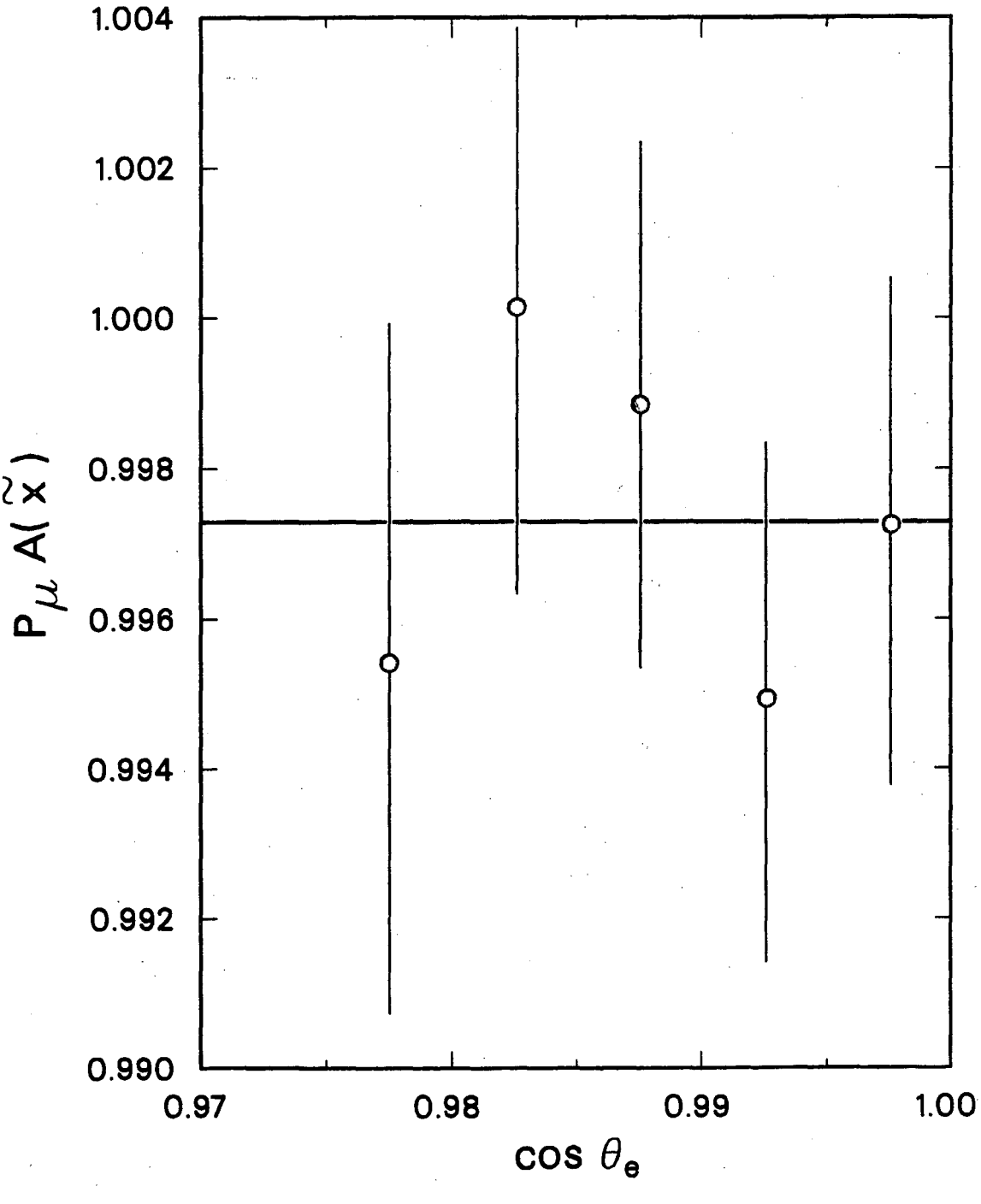

FIGURE (7.6). Weighted mean fitted $P_\mu A(\tilde{x})$ in each $\cos\theta_e$ bin for the metal targets excluding Run 2 Cu and Cu*.

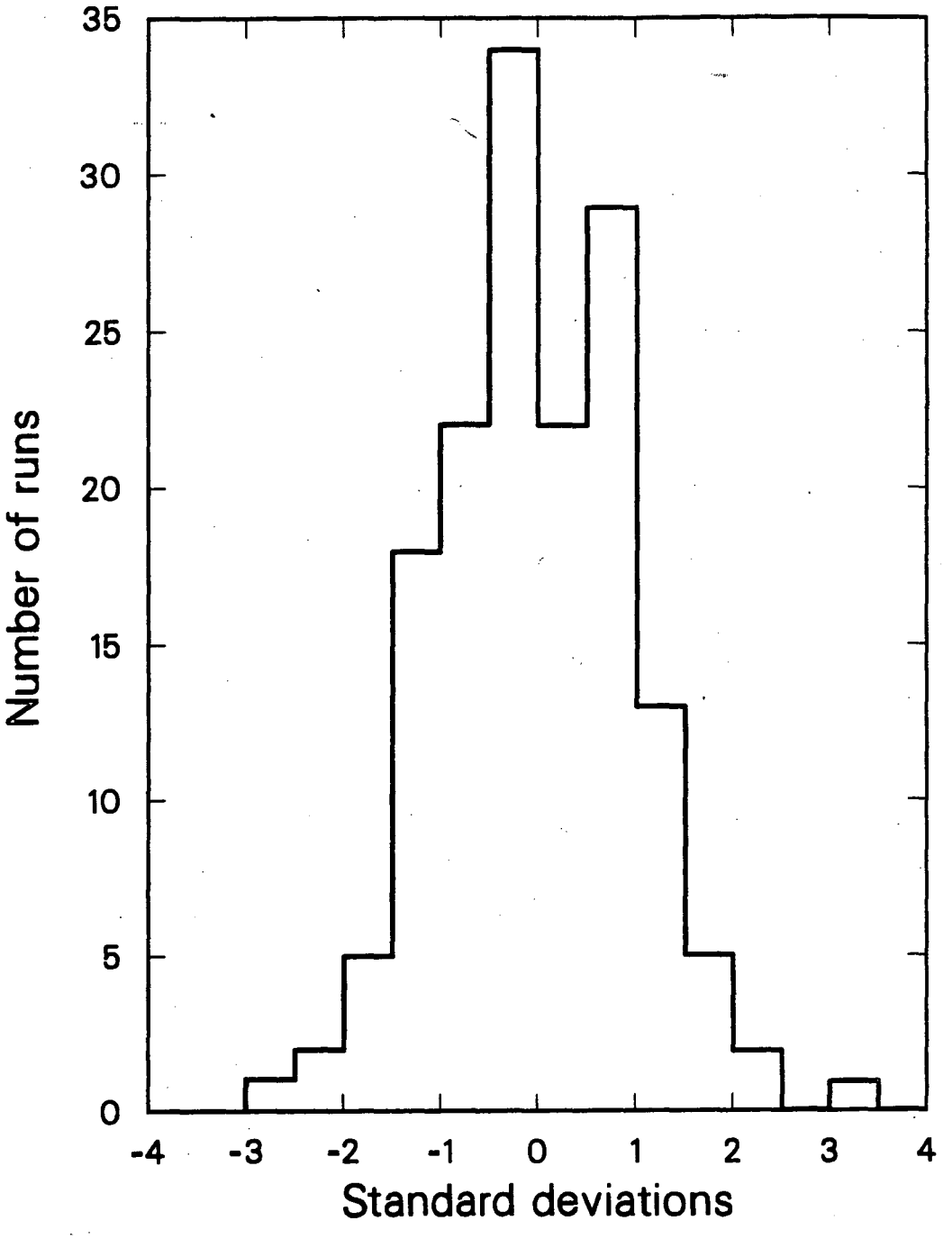

FIGURE (7.7). Histogram of the deviation of the individual run $P_\mu A(\tilde{x})$ from the corresponding data set mean in units of the individual run statistical error. All runs listed in Table (C.2) are included.

deficiencies prior to data fitting. The $P_\mu A(\tilde{x})$ of individual runs contributing to the final results are displayed in the Figure (7.8) histogram.

In each of the three auxiliary fits the μ^+ spin precession frequency, the initial time t_0 and the muon mean-life were fixed to the corresponding values determined in the primary fits. The statistical errors on $P_\mu A(\tilde{x})$ in the auxiliary fits have been increased by the 5% required to compensate for the fixed parameters.

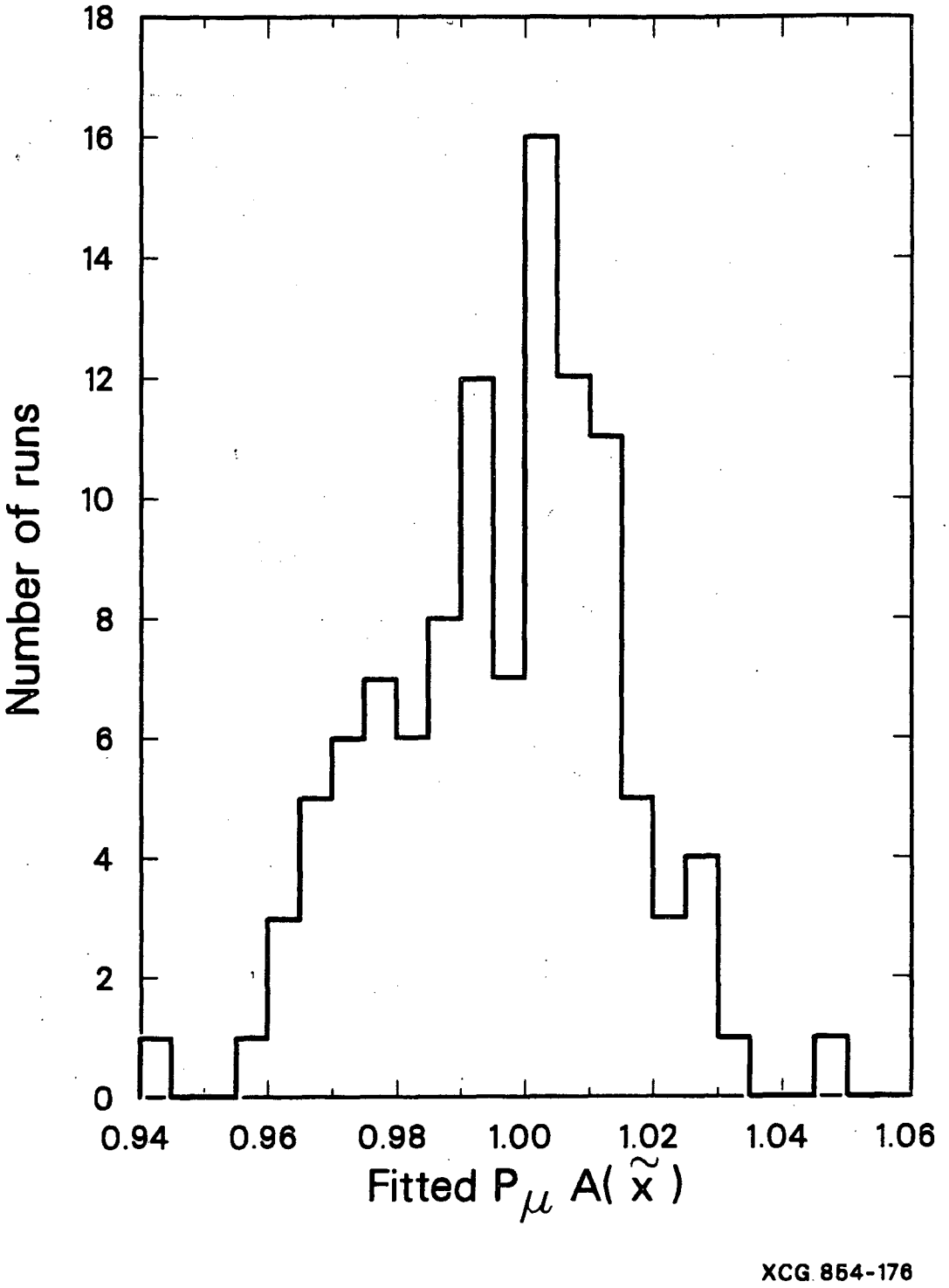

FIGURE (7.8). Histogram of the individual run $P_\mu A(\tilde{x})$ for the metal targets excluding Run 2 Cu and Cu*.

Chapter 8

Corrections and Systematics

8.1 Corrections

8.1.1 Muon Depolarization in Scattering with Electrons

The muon beam polarization is reduced by spin exchange effects in scattering with the unpolarized electrons of the medium[38]. Assuming that the muon energy-loss for E>3 keV is due entirely to scattering with electrons, the calculation in section (4.2) shows the polarization of the stopped beam is 0.9993 of the initial P_μ. A possible error of ±0.0002 is assigned to this estimated depolarization. The fitted values of $P_\mu A(\tilde{x})$ should therefore be corrected upwards by a factor of 1.0007±0.0002.

8.1.2 Coulomb Scattering

The method for obtaining the $\langle\cos\theta\rangle_t$ for each time bin was discussed in section (7.3). It was shown that if azimuthal symmetry applied

$$\langle\cos\theta\rangle_t = \langle\cos\theta_\mu\rangle\langle\cos\theta_e\rangle\cos\omega t$$

Coulomb scattering is relativistically helicity conserving and non-relativistically spin conserving. The non-relativistic limit is assumed to apply to the μ^+, which initially have β=0.27. The effect of multiple Coulomb scattering is to misalign the μ^+ spin and momentum directions, and to misalign the true and measured e^+ emission

directions. Consequently corrections must be made to both $\langle\cos\theta_\mu\rangle$ and $\langle\cos\theta_e\rangle$.

To a good approximation material upstream of the midpoint between proportional chambers P1 and P2, which measure the incoming muon direction, contributes to the misalignment of the μ^+ spin and momentum directions while material downstream of this point does not. However, scattering in the production target material and in the material near P1 require corrections of opposite sign to $\langle\cos\theta_\mu\rangle$. Consider an idealized beamline which admits only μ^+ with momenta along the beam axis after Coulomb scattering in the production target. Suppose the amount of material near P1 is negligibly small. Since the μ^+ spins and momenta are misaligned $|\langle\cos\theta_{\mu,spin}\rangle|<|\langle\cos\theta_\mu\rangle|=1$. Now suppose the amount of production target material is negligibly small so that the μ^+ leave the beamline with spins and momenta aligned along the beam axis. Scattering near P1 leaves the spins aligned along the beam axis and now $|\langle\cos\theta_\mu\rangle|<|\langle\cos\theta_{\mu,spin}\rangle|=1$.

The mean production target thickness traversed by the μ^+ was 6.2 mg/cm^2. The thickness of the other material upstream of the midpoint of P1 and P2 was 18.4 mg/cm^2. Scattering near P1 should therefore dominate, requiring a net upwards correction to $\langle\cos\theta_\mu\rangle$ and a downwards correction to $P_\mu A(\tilde{x})$. It should be noted that acceptance effects and software cuts preferentially reject potential events with the largest μ^+ scattering angles near P1. Detailed Monte Carlo studies using calculations of Moliere scattering[50,51] yield a correction for $\langle\cos\theta_\mu\rangle$ of +0.0003, and hence a correction factor for $P_\mu A(\tilde{x})$ of 0.9997. A possible error of ±0.0002 is assigned to the correction.

The e^+ scattering is more transparent. Events in which the e^+ is

scattered out of the angular acceptance, i.e. to $\cos\theta_e<0.975$, are lost while events in which the e^+ are scattered into the angular acceptance are gained. Thus $\langle\cos\theta_{e,true}\rangle < \langle\cos\theta_e\rangle$ and an upwards correction to $P_\mu A(\tilde{x})$ is required. Monte Carlo studies yield a correction factor, averaged over the various stopping targets, for $P_\mu A(\tilde{x})$ of 1.0002. A possible error of ±0.0001 is assigned to this correction.

8.1.3 Extra Muons

The number N of muons expected to be present in the stopping target is determined by the μ^+ beam rate λ and mean-life τ_μ :

$$\frac{dN}{dt} = \lambda - \frac{N}{\tau_\mu}$$

If the beam is turned on at t=0

$$N(t) = \lambda\tau_\mu[1-\exp(-t/\tau_\mu)]$$

Assuming an average proton current of 80 μA incident on the production target the μ^+ beam rate is estimated to be $\lambda=1.5\times10^4$ Hz from the observed μ-stop rate corrected for dead-time.

Events with extra μ^+ arriving up to 10 μs before the μ-stop are tagged as 'extra-befores' and are rejected. The residual admixture of extra-befores arriving before the 10 μs rejection period is therefore $\lambda\tau_\mu\exp(-10\mu s/\tau_\mu)=3.5\times10^{-4}$. The requirement of continuity between the μ^+ and e^+ tracks at the stopping target [section (6.4)] is estimated to reduce the admixture to 0.9×10^{-4}. Taking these extra-before μ^+ to be time-average unpolarized with respect to the μ-stop muons implies a correction factor of 1.0001 for the fitted $P_\mu A(\tilde{x})$. A possible error of

±0.0001 is assigned to this correction.

A similar calculation for extra-after μ^+ arriving unobserved during the 0-0.3 μs notch (Runs 2, 3) in extra-after-1 [section (5.3)] implies correction factors of 1.0005 for B_T=70-G and 1.0011 for B_T=110-G. However, the after-pulsing in P1 and P2 which necessitated the notch cause some extra-after μ^+ arriving within the notch to be observed as after-pulses after the notch. The above corrections are therefore too large. If extra-after-2, with a 0-0.5 μs notch (Runs 2, 3), is used instead of extra-after-1 the mean fitted $P_\mu A(\tilde{x})$ is reduced by 0.0009 whereas the calculated reduction is 0.0013. Thus 30% of the effect appears to be lost to after-pulsing. A larger proportion of extra-after μ^+ arriving within the shorter 0-0.3 μs notch should be observed as after-pulses. It is estimated that the calculated corrections should be reduced by 50%. Averaging over the two B_T values and including the effect of the longer 0.6 μs notch in Run 1 yields a correction factor of 1.0004 for the fitted $P_\mu A(\tilde{x})$. A possible error of ±0.0003 is conservatively assigned to this correction.

8.1.4 Cloud Muons

Figure (5.3) indicates that 98% of cloud μ^+ are eliminated by the rf time cuts. The fitted asymmetry is reduced by 0.015 when no rf time cuts are made. The residual 2% of cloud μ^+ therefore require an estimated correction factor of 1.0003±0.0002 for the fitted $P_\mu A(\tilde{x})$.

8.1.5 Longitudinal Field Component

Any residual longitudinal component in the μ^+ spin precessing field reduces the apparent μSR signal amplitude.

The methods used to null the ≈40-G longitudinal field in the stopping target region [section (5.2.1)] are estimated to leave an rms residual longitudinal field ≈1-G.

In addition the μ^+ experience the longitudinal components of the random local fields due to the nuclear magnetic dipoles. As noted in section (4.4) the local fields are a few Gauss for aluminum and copper. However, at room temperature the μ^+ are mobile and sample many different local fields in succession. The time-average local field seen by the μ^+ is therefore reduced. Assuming a uniform applied transverse field, the local field ΔB is related to the static linewidth σ by equation (4.3): $\langle \Delta B^2 \rangle = 2\sigma^2/\gamma_\mu^2$. Taking σ^2 from fits using the Gaussian spin relaxation function $G(t)=\exp(-\sigma^2 t^2)$ yields effective rms local fields ΔB_{rms} ranging from 0.2-G for the Au target to 1.0-G for the Al target. The rms longitudinal local field component is $\Delta B_{rms}/\sqrt{3}$.

After adding in quadrature to obtain the total longitudinal field B_ℓ, the correction factor for $P_\mu A(\tilde{x})$ is $1/\cos(B_\ell/B_T) = 1.0001$ when averaged over the B_T values. A possible error of ±0.0001 is assigned to this correction.

8.1.6 Timing Errors

Any random spreads in the times attributed to the μ-stop and μ-decay relative to the true times effectively smear the μSR signal, thereby reducing its apparent amplitude. The time spreads of signals

from the left and right photomutlipliers viewing S1 and S2 with respect to the mixed S1 and mixed S2 signals allow an estimate of 2 ns for the rms error on the lifetime of the individual muons. The μ^+ spin precession period is T=1.06 μs for B_T=70-G and T=0.65 μs for B_T=110-G, resulting in a correction factor for $P_\mu A(\tilde{x})$ of $1/\cos(2\pi \times 2ns/T) = 1.0001$ when averaged over B_T values. A possible error of ±0.0001 is assigned to this correction.

8.1.7 Summary

The corrections discussed in the preceding sections are summarized in Table (8.1). The combined correction factor is 1.0016±0.0006. The possible errors in the μ^+ and e^+ Coulomb scattering corrections have been added linearly, as have the possible errors in the extra-before and extra-after muon corrections, before being added in quadrature to the other possible errors.

Source of Correction	Correction Factor
Muon depolarization in scattering with e^-	1.0007 ± 0.0002
Coulomb scattering of muons	0.9997 ± 0.0002
Coulomb scattering of positrons	1.0002 ± 0.0001
Extra-before muons	1.0001 ± 0.0001
Extra-after muons	1.0004 ± 0.0003
Residual cloud muons	1.0003 ± 0.0002
Longitudinal field component	1.0001 ± 0.0001
Timing errors	1.0001 ± 0.0001
Total correction factor	1.0016 ± 0.0006

Table (8.1)

8.2 Systematic Errors

The major sources of possible systematic error, other than those associated with the corrections of section (8.1), are discussed in the following sections. Other possible systematic errors are estimated to be small compared to ±0.0001.

8.2.1 Reconstruction of θ_μ and θ_e

The main sources of possible systematic error in the reconstruction of $\cos\theta_\mu$ and $\cos\theta_e$ are longitudinal misalignment of the wire-chambers and the approximations involved in using the first-order optics formalism (Appendix A) to determine the e^+ track.

A possible error of ±2 mm in the relative longitudinal positions of P1 and P2, and of P3 relative to D1 and D2, correspond to errors of ±0.0002 in $\langle\cos\theta_\mu\rangle$ and $\langle\cos\theta_e\rangle$.

Monte Carlo studies show that the first-order optics formalism reconstructs the e^+ tracks, in the absence of scattering and chamber resolution effects, with an accuracy much better than ±0.0001 in $\langle\cos\theta_e\rangle$. A 10% change in the assumed field strength was shown to cause a change in the reconstructed $\langle\cos\theta_e\rangle$ small compared to 0.0001. In practice minimizing the wire-chamber rms residuals allowed the field scaling factor [95% of the Table (5.1) values] to be determined to ±5%. A more conservative estimate of ±0.0002 for the possible error associated with the first-order optics formalism is adopted here.

The μ^+ and e^+ have radii of curvature of ≈10 m and ≈15 m in the spin precessing field B_T. Ignoring their 5 cm path length through B_T causes a negligible error in the reconstructed $\langle\cos\theta_\mu\rangle$ and $\langle\cos\theta_e\rangle$.

The possible reconstruction errors are therefore estimated to be ± 0.0002 in $\langle \cos\theta_\mu \rangle$ and ± 0.0003 in $\langle \cos\theta_e \rangle$.

8.2.2 Momentum Calibration

The possible errors in the momentum calibration for the various x bins are shown in Table (6.1). Near the (V-A) limit an error Δx in momentum yields

$$\Delta[P_\mu A(\tilde{x})]/P_\mu A(\tilde{x}) = -4\Delta x/(1-4\tilde{x}^2)$$

The momentum calibration contributes a possible error of ± 0.0010 to the determination of the endpoint asymmetry $P_\mu A(0)=\xi P_\mu \delta/\rho$ [section (9.4)].

8.2.3 Definition of x=1

In order to fit the data to the theoretical momemtum spectra it is necessary for their endpoints to coincide. This was achieved by fitting the endpoint positions of both the data and 'events' generated from the theoretical spectra, and adjusting the data x to obtain agreement as discussed in section (6.5). Assigning a possible error of ± 0.0001 to the endpoint agreement yields an error of $\pm 0.04\%$ in the fitted asymmetries, i.e. ± 0.0004 for $P_\mu A(\tilde{x})\approx 1$.

8.2.4 Energy-Loss Straggling

An error of 10% in the amount of downstream material traversed by the e^+ corresponds to an average error of ± 0.0003 in the fitted $P_\mu A(\tilde{x})$.

8.2.5 Muon Mean-Life

The fits described in section (7.6) were performed with the μ^+ mean-life fixed to the mean value obtained for the corresponding run period. The combined mean-life from the three run periods, which used different clocks, is τ_μ=2.209±0.003 μs assuming zero background. The statistical error is ±0.006 μs for free background. A more conservative estimate of ±0.008 μs is adopted here for the possible error in τ_μ. This corresponds to an error of ±0.0003 in the fitted $P_\mu A(\tilde{x})$.

8.2.6 Summary

The possible systematic errors discussed in sections (8.1) and (8.2) are summarized in Table (8.2). The combined possible systematic error is ±0.0013 when averaged over x bins. Table (9.1) shows the possible systematic errors for the individual x bins, which differ due to the momentum calibration contribution.

Source of Possible Error	Error
Muon depolarization in scattering with e^-	±0.0002
Coulomb scattering of muons	±0.0002
Coulomb scattering of positrons	±0.0001
Extra-before muons	±0.0001
Extra-after muons	±0.0003
Cloud muons	±0.0002
Longitudinal field component	±0.0001
Timing errors	±0.0001
Reconstruction of θ_μ	±0.0002
Reconstruction of θ_e	±0.0003
Momentum calibration	±0.0010
Definition of x=1	±0.0004
Positron energy-loss straggling	±0.0003
Muon mean-life τ_μ	±0.0003
Total 1σ possible error	±0.0013

Table (8.2)

Chapter 9

Results and Conclusions

9.1 The Normalized Asymmetries

The weighted mean normalized asymmetries $P_\mu A(\tilde{x})$ of the data sets contributing to the final result are shown in Table (9.1). The corrections discussed in section (8.1) are included and the estimated possible systematic errors discussed in section (8.2) are also shown.

x Range	$P_\mu A(\tilde{x})$	Systematic Error
0.88-0.90	0.9964±0.0074	±0.0029
0.90-0.92	1.0109±0.0062	±0.0024
0.92-0.94	0.9948±0.0047	±0.0018
0.94-0.96	1.0019±0.0040	±0.0015
0.96-0.98	0.9939±0.0034	±0.0011
0.98-1.00	1.0002±0.0028	±0.0009

Table (9.1)

The systematic errors listed in Table (9.1) should be regarded as being completely correlated between the x bins. Thus if the results for N of the x bins are combined the chi-square is given by

$$\chi^2 = \sum_{ij}(p_i-d_i)[V^{-1}]_{ij}(p_j-d_j)$$

where $$V_{ij} = \delta_{ij}\sigma_i^{stat}\sigma_j^{stat} + \sigma_i^{sys}\sigma_j^{sys}$$

and p_i and d_i are the predicted and data values respectively.

9.2 Right-Handed Current Limits With Massless Neutrinos

In left-right symmetric models with massless neutrinos the mass-squared ratio $\varepsilon=M^2(W_1)/M^2(W_2)$ and mixing angle ζ are related to the normalized asymmetries by equation (3.5):

$$P_\mu A(\tilde{x}) = 1 - 2\{2\varepsilon^2 + 2\varepsilon\zeta + \zeta^2[1 + 6\tilde{x}/(1+2\tilde{x})]\}$$

The right-hand side is unchanged if the replacements $\varepsilon\to-\varepsilon$ and $\zeta\to-\zeta$ are made. Fitting the asymmetries in Table (9.1) to equation (3.5) therefore yields two minima of equal chi-square χ_0^2 in the real ε-ζ plane. The physical minimum, denoted by (ε_0,ζ_0), has $\varepsilon_0\geq 0$ whereas $\varepsilon<0$ implies imaginary $M(W_2)$. The 90% confidence limits ($\pm 1.645\sigma_0$) on ζ for $\varepsilon=\varepsilon_0$ correspond to the (ε_0,ζ) for which $\chi^2=\chi_0^2+2.706$. The contour in Figure (9.1) is a curve of constant $\chi^2=\chi_0^2+2.706$ and thus represents a 90% confidence limit in the above sense.

Limits on $M(Z_2)$ are implied by the relation [section (2.2)] $M(Z_2)=M(W_2)\cos\theta_W'/\sqrt{(\cos 2\theta_W')}$. Assuming $M(W_1)=81$ GeV/c^2 and $\sin^2\theta_W'=0.217$ [section (2.1)] the following special case 90% confidence limits are obtained: $M(W_2)>381$ GeV/c^2 and $M(Z_2)>448$ GeV/c^2 for any ζ; $M(W_2)>434$ GeV/c^2 and $M(Z_2)>510$ GeV/c^2 for $\zeta=0$; $|\zeta|<0.044$ for $M(W_2)=\infty$; and $-0.057<\zeta<0.044$ for any $M(W_2)$.

9.3 Limits On $M(W_2)$ With $M(\nu_{\mu R})\neq 0$

The limits obtained in the preceding section assumed massless neutrinos. As discussed in section (2.3) a popular model[15] with Majorana neutrinos has very heavy [$\approx M(W_2)$] right-handed neutrinos. In that case W_R is decoupled from muon decay and the present experiment

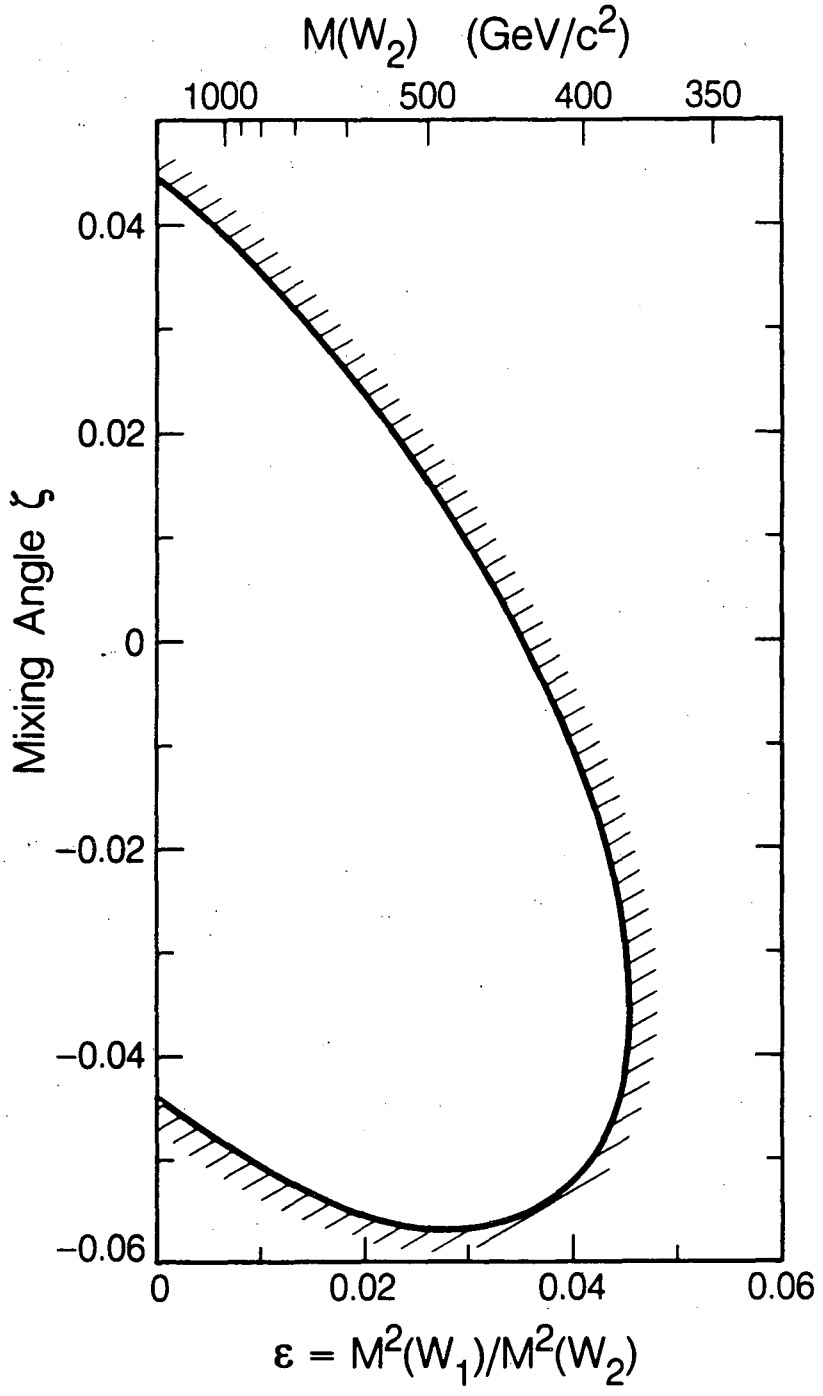

FIGURE (9.1). Contour representing 90% confidence limits on the $W_{1,2}$ mass-squared ratio ε and the left-right mixing angle ζ. The allowed region contains $\varepsilon=\zeta=0$.

sets no limits on right-handed currents. Here limits on $M(W_2)$ are obtained for another possible, if less appealing, scenario: that neutrinos are Majorana particles with $M(\nu_{eR})<<M(\nu_{\mu R})<40$ MeV/c^2 . For simplicity it is assumed that the mixing angle $\zeta=0$ so that $W_2\equiv W_R$.

According to Rekalo[52] the differential decay rate for μ^- via (V-A), and hence for μ^+ via (V+A), including finite ν_μ mass, but neglecting e^- mass and radiative corrections is

$$\frac{d^2\Gamma}{dx\,d(\cos\theta)} \sim (1-\nu^2/k^2)x^2\{(3-2x)+(3-x)\nu^2/k^2+\cos\theta[1-2x-(1+x)\nu^2/k^2]\} \quad (9.1)$$

where $\nu=M(\nu_\mu)$, $k^2=m_\mu^2-2m_\mu E_e$, and $x\equiv E_e/E_e(max)$ with $E_e(max)=(m_\mu^2-\nu^2)/2m_\mu$.

Limits on $M(W_2)$ as a function of $M(\nu_{\mu R})$ were determined from the normalized asymmetries in Table (9.1). $M(\nu_{\mu R})$=0,14.9,21.1,25.9,29.9, 33.4 and 36.6 MeV/c^2 yield W_R-mediated $E_e(max)$ at the W_L-mediated x=1,0.98,0.96,0.94,0.92,0.90, and 0.88 bin boundaries respectively. Considering only the Table (9.1) asymmetries lying below the W_R-mediated $E_e(max)$ the best fit (V+A) admixture to the (V-A) decay rate was determined for each of the above $M(\nu_{\mu R})$. The μ^+ from W_R-mediated π^+ decay have momenta too low to be accepted by the beamline for all the above $M(\nu_{\mu R})\neq 0$. Since it is assumed here that $\zeta=0$ it follows that the fitted (V+A) admixture is ε^2 for the above $M(\nu_{\mu R})\neq 0$, and $2\varepsilon^2$ for $M(\nu_{\mu R})=0$. The unphysical $\varepsilon^2<0$ region was excluded and 90% confidence lower limits on $M(W_2)$ were determined in the remaining physical region.

The result $M(W_2)>444$ GeV/c^2 for $M(\nu_{\mu R})=0$ is in close but not perfect agreement with the limit $M(W_2)>434$ GeV/c^2 for $\zeta=0$ and $m(\nu)=0$ obtained from the 90% confidence ε-ζ contour in section (9.2).

Accordingly the mass limits found here were reduced by 2% to establish agreement at $m(\nu)=0$. The resulting limits on $M(W_2)$ as a function of $M(\nu_{\mu R})$ are shown in Figure (9.2). The kink near $M(\nu_{\mu R})=5$ MeV/c^2 corresponds to the W_R-mediated π^+ decay μ^+ momentum decreasing below the beam-line setting as $M(\nu_{\mu R})$ increases.

The absence of radiative corrections in equation (9.1) introduces an error into the $M(W_2)$ limits when the (V-A) and (V+A) momentum spectra have different endpoints, i.e. when $M(\nu_{\mu R})\neq 0$. The radiative corrections in section (3.3) reduce the (V-A) decay rate for unpolarized muons by 8.2% at x=0.99 and by 3.5% at x=0.89. Consequently in the 'worst case' fit, where the x=0.978-1.00 W_R-mediated x bin coincides with the x=0.88-0.90 W_L-mediated x bin, the fitted ε^2 should be ≈5% too small. Increasing the central value of ε^2 by 5% for the $M(\nu_{\mu R})=33.4$ MeV/c^2 point reduces the corresponding 90% confidence limit on $M(W_2)$ by only 0.2%. Thus the error introduced by the absence of radiative corrections in equation (9.1) is negligible.

9.4 Limits On $\xi P_\mu \delta/\rho$

The normalized asymmetries $P_\mu A(\tilde{x})$ are related to the muon decay parameters ξ, δ, and ρ by equation (3.3):

$$P_\mu A(\tilde{x}) = (\xi P_\mu \delta/\rho)\{1 + 2\tilde{x}[\tilde{\delta}/(1-2\tilde{x}) - 3\tilde{\rho}/(1+2\tilde{x})]\}$$

The endpoint asymmetry $P_\mu A(0) = \xi P_\mu \delta/\rho$ was obtained by fitting the asymmetries in Table (9.1) by equation (3.3) using the world average value[31] of $\rho=0.7517\pm0.0026$, and $\delta=0.750\pm0.004$ which combines the previous world average value[31] $\delta=0.7551\pm0.0085$ with the preliminary

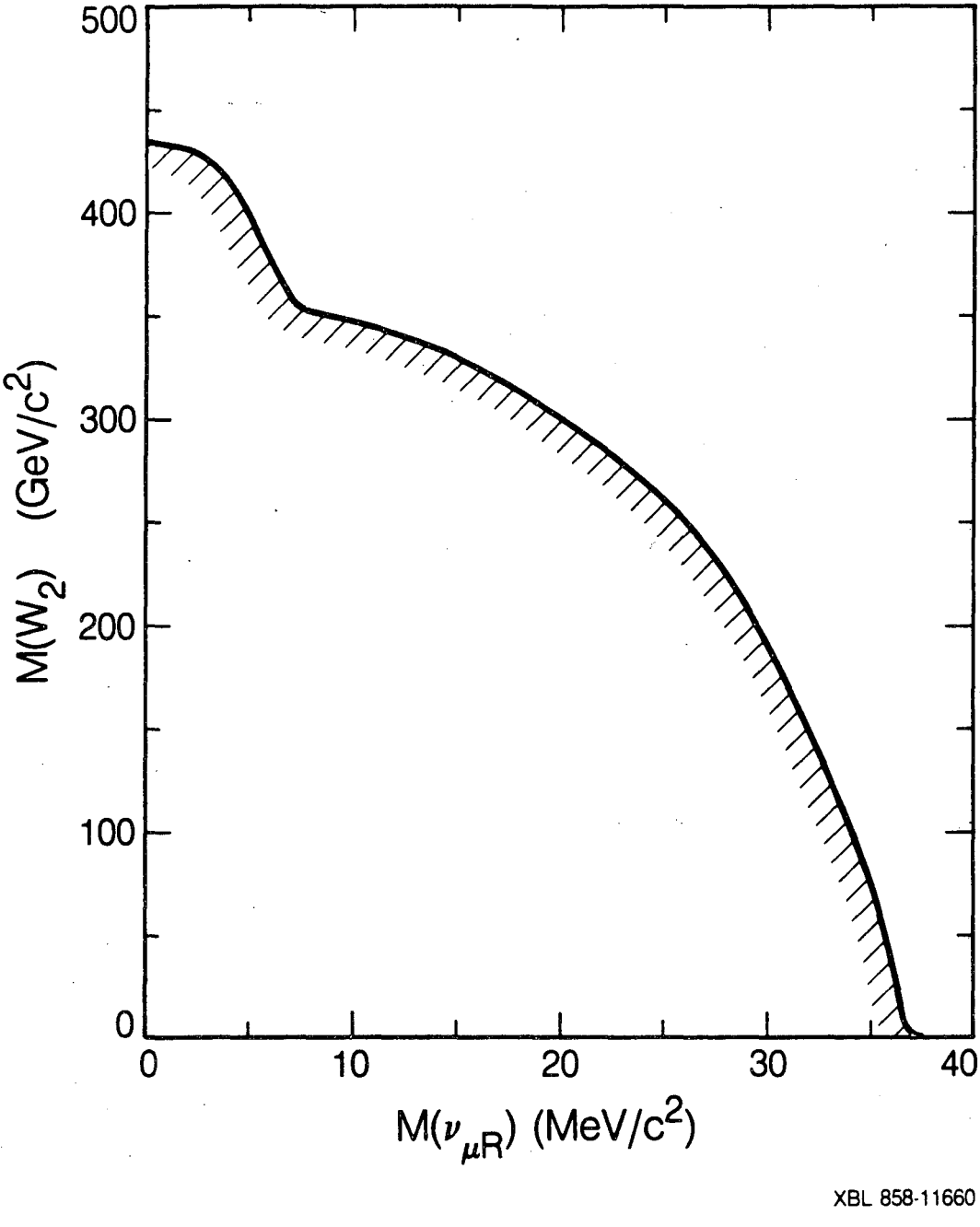

FIGURE (9.2). Contour representing 90% confidence limit on $M(W_2)$ versus the mass of any right-handed ν_μ assuming $M(\nu_{eR}) << M(\nu_{\mu R})$. For $M(\nu_{\mu R}) > 5$ MeV/c^2 surface muons from W_R-mediated π^+ decay have momenta below the beamline momentum acceptance. The allowed region lies above the contour.

result[53] $\delta=0.748\pm0.005$ from Run 3 of the present experiment. The fit to the asymmetries before making the correction of +0.0016 discussed in section (8.1) was shown in Figure (7.4). The uncertainties in δ and ρ introduce a possible systematic error of ±0.0009 into the determination of $\xi P_\mu \delta/\rho$. The fitted value is $\xi P_\mu \delta/\rho=0.9984\pm0.0016\pm0.0016$. Since any unknown sources of μ^+ depolarization or any neglected background can only decrease the apparent result, a lower limit for $\xi P_\mu \delta/\rho$ should be quoted. Excluding the unphysical ($\xi P_\mu \delta/\rho>1$) region the 90% confidence limit is $\xi P_\mu \delta/\rho>0.9951$.

9.5 Limits on $M(\nu_{\mu L})$ and $\nu_{\mu L}$ Helicity in π^+ Decay

Limits on the mass of the left-handed muon neutrino and its helicity in pion decay can be deduced from the 90% confidence limit $\xi P_\mu \delta/\rho>0.9951$. The weakest limits are obtained if it is assumed that right-handed currents are absent. In that case $\xi\delta/\rho=1$ and hence $P_\mu>0.9951$. The 90% confidence limit on the $\nu_{\mu L}$ helicity in π^+ decay is then $|h(\nu_{\mu L})|>0.9951$. The corresponding limit on the $\nu_{\mu L}$ velocity $\beta=v/c>0.9951$ in π^+ decay yields the 90% confidence limit $M(\nu_{\mu L})<3.0$ MeV/c^2. For comparison the world average value[31] $M(\nu_{\mu L})<0.5$ MeV/c^2 implies $P_\mu>0.99986$ in the absence of right-handed currents.

9.6 Lorentz Structure Restrictions

The couplings in the helicity projection form of the flavor retention interaction Hamiltonian due to Mursula and Scheck[36] are related to $\xi\delta/\rho$ by equation (3.12). If only one coupling other than the (V-A) coupling $g_{22}=1$ is non-zero the 90% confidence limit $\xi P_\mu \delta/\rho > 0.9951$ restricts $|g_{11}|, |f_{11}| < 0.050$ and $|h_{11}|, |h_{21}| < 0.10$. The relations among the couplings under the assumption of e-μ universality were discussed in section (3.5).

In the special case that the charged current weak interactions are mediated by one heavy spin 1 boson the μ^+ polarization in π^+ decay is given by $P_\mu = (g_{22}-g_{11})/(g_{22}+g_{11})$ and hence $g_{11} < 0.0025$ with 90% confidence.

Mursula and Scheck also considered the case of neutral Q^0 exchange in addition to $W_L^\pm$ exchange. The Q^0 would have total lepton number L=0 but $L_e = \pm 1$ and $L_\mu = \mp 1$. With the new scalar, vector, and tensor couplings denoted by η, γ, and ϕ instead of h, g, and f respectively they find:

$$\xi\delta/\rho \approx 1 - 2(|\gamma_{11}|^2 + |\gamma_{12}|^2 + 4|\phi_{11}|^2)$$

If only one coupling is non-zero the 90% confidence limits are $|\gamma_{11}|, |\gamma_{12}| < 0.050$ and $|\phi_{11}| < 0.025$.

9.7 Limits On Composite Leptons

The possibility that leptons and quarks are composite at some mass scale Λ has received considerable attention in recent years. Among the strongest experimental limits on Λ currently quoted[54,55] are those from Bhabba scattering (>750 GeV), muon (g-2) (>860 GeV), and a more

model-dependent estimate from ν-hadron scattering (>2.5 TeV).

The effects of compositeness may be analyzed in terms of new effective contact interactions. Following the analyses of Peskin[56], and Lane and Barany[57] the most general $SU(2)\times U(1)$ invariant contact interaction contributing to $\mu \to e\nu\bar{\nu}$ is

$$\begin{aligned} L_{cont} = (g^2/\Lambda^2)[&\eta_1(\bar{\nu}_{\mu L}\gamma^\kappa\mu_L)(\bar{e}_L\gamma_\kappa\nu_{eL}) + \eta_2(\bar{\nu}_{\mu R}\gamma^\kappa\mu_R)(\bar{e}_R\gamma_\kappa\nu_{eR}) \\ &+ \eta_3(\bar{\nu}_{\mu L}\gamma^\kappa\nu_{eL})(\bar{e}_R\gamma_\kappa\mu_R) + \eta_4(\bar{e}_L\gamma^\kappa\mu_L)(\bar{\nu}_{\mu R}\gamma_\kappa\nu_{eR}) \\ &+ \eta_5(\bar{\nu}_{\mu L}\mu_R)(\bar{e}_L\nu_{eR}) + \eta_6(\bar{\nu}_{\mu L}\nu_{eR})(\bar{e}_L\mu_R) \\ &+ \eta_7(\bar{\nu}_{\mu R}\mu_L)(\bar{e}_R\nu_{eL}) + \eta_8(\bar{\nu}_{\mu R}\nu_{eL})(\bar{e}_R\mu_L) \end{aligned} \tag{9.3}$$

where g is a coupling of hadronic strength; the η_i are of order unity and are normalized so that $|\eta_L|=1$ in the diagonal coupling

$$(g^2/2\Lambda^2)[\eta_L(\bar{e}_L\gamma^\kappa e_L)(\bar{e}_L\gamma_\kappa e_L) + \ldots\ ]$$

The first and second terms in equation (9.3) are purely left-handed and right-handed respectively, and hence are indistinguishable from the usual (V-A) and (V+A) interactions.

There are three special cases of interest:

1. If only left-handed (right-handed) leptons are composite then only the purely left-handed (right-handed) term survives, i.e. only η_1 (η_2) $\neq 0$.
2. If both left-handed and right-handed leptons are composite but contain quite different sets of constituents then the purely left-handed and right-handed terms dominate, i.e. $\eta_1, \eta_2 >>$ other η_i.
3. If there is no ν_R, or $M(\nu_R)$ is large, only $\eta_1, \eta_3 \neq 0$.

Assuming an effective interaction Lagrangian $L_{eff} = L_{V-A} + L_{cont}$ yields the endpoint decay rate:

$$1 - P_\mu A(0) = 2(620\text{GeV}/\Lambda)^4 (g^2/4\pi)^2 (\eta_2^2 + \eta_3^2 + \eta_5^2/4)$$

The limit $P_\mu A(0) = \xi P_\mu \delta/\rho > 0.9951$ then implies

$$\Lambda^2 > (2780\text{GeV})^2 (g^2/4\pi) \sqrt{(\eta_2^2 + \eta_3^2 + \eta_5^2/4)}$$

with 90% confidence. (If the not unreasonable assumptions $g^2/4\pi \approx 2.1$ and $\eta_i > 0.2$ are made, the limit $\Lambda > 2200$ GeV would be obtained.)

For the special cases discussed earlier the limit becomes

1. Only left-handed leptons composite: no limit.

   Only right-handed leptons composite: $\Lambda^2 > (2780\text{GeV})^2 (g^2/4\pi) \eta_2$

2. Left- and right-handed leptons have

   different sets of constituents: $\Lambda^2 > (2780\text{GeV})^2 (g^2/4\pi) \eta_2$

3. No ν_R, or $M(\nu_R)$ large: $\Lambda^2 > (2780\text{GeV})^2 (g^2/4\pi) \eta_3$

Appendix A

First-Order Optics of Solenoidal Fields

This Appendix follows closely a set of notes by K. Halbach[48]. The equation of motion for a particle of momentum $\underset{\sim}{p}$ and charge e in an external magnetic field $\underset{\sim}{B}$ is

$$\dot{\underset{\sim}{p}} = e(\dot{\underset{\sim}{x}} \times \underset{\sim}{B}) \tag{A.1}$$

Evaluation of $\underset{\sim}{\nabla}.\underset{\sim}{B}=0$ on the solenoid axis (z-axis) gives the first order off-axis field components

$$B_x = -xB_z'/2 \quad \text{and} \quad B_y = -yB_z'/2$$

where d/dz is denoted by '.

Then from (A.1)

$$\dot{p}_x = e(\dot{y}B_z + \dot{z}yB_z'/2) \tag{A.2}$$

$$\dot{p}_y = -e(\dot{z}xB_z'/2 + \dot{x}B_z) \tag{A.3}$$

$$\dot{p}_z = e(\dot{y}x - \dot{x}y)B_z'/2 \tag{A.4}$$

With $\dot{z}=v_o$ and $eB_z/mv_o = B_z/B\rho = k$, where $B\rho$ is the magnetic rigidity of the particle, (A.2) and (A.3) become

$$x'' = y'k + yk'/2$$

$$y'' = -(x'k + xk'/2)$$

which with the notation $w = x+iy$ may be written as

$$w'' = -i(kw' + k'w/2) \tag{A.5}$$

Introducing a new coordinate system $\zeta = \xi+i\eta$ in the w plane, but rotated by $-\alpha$ with respect to $w = x+iy$ gives

$$w = \zeta e^{i\alpha} \tag{A.6}$$

$$w' = (\zeta' + i\alpha'\zeta)e^{i\alpha} \tag{A.7}$$

$$w'' = (\zeta'' + 2i\alpha'\zeta' + i\alpha''\zeta - \alpha'^2\zeta)e^{i\alpha}$$

and from (A.5)

$$\zeta'' + i(2\alpha'+k)\zeta' + (i\alpha''-\alpha'^2-\alpha'k+ik'/2)\zeta = 0$$

Now setting $\alpha' = -k/2$, $\alpha = -(1/2B\rho)\int_0^z B_z(z)dz$ yields

$$\zeta'' + (k/2)^2\zeta = 0 \tag{A.8}$$

The particle motions in the ξ and η directions of the rotating ζ coordinate system are now decoupled:

$$\xi''+(k/2)^2\xi = 0 \quad \text{and} \quad \eta''+(k/2)^2\eta = 0$$

Equation (A.8) has solution

$$\zeta(z) = c_1\cos(kz/2) + c_2\sin(kz/2)$$

and hence $$\zeta'(z) = (k/2)[-c_1\sin(kz/2) + c_2\cos(kz/2)]$$

Choosing the initial conditions $\zeta(0)=\zeta_0$ and $\zeta'(0)=\zeta_0'$ implies $c_1=\zeta_0$ and $c_2=2\zeta_0'/k$. Thus (ζ,ζ') at $z+L$ are related to (ζ_0,ζ_0') at z by

$$\begin{bmatrix}\zeta \\ \zeta'\end{bmatrix} = \begin{bmatrix}\cos(kL/2) & (2/k)\sin(kL/2) \\ -(k/2)\sin(kL/2) & \cos(kL/2)\end{bmatrix}\begin{bmatrix}\zeta_0 \\ \zeta_0'\end{bmatrix} \tag{A.9}$$

where $k=\langle B_z \rangle / B\rho$.

The track vector in the laboratory (w) coordinate system is given by (A.6) and (A.7):

$$x+iy = (\xi+i\eta)(\cos\alpha+i\sin\alpha)$$

$$x'+iy' = [\xi'+i\eta'+(\eta-i\xi)k/2](\cos\alpha+i\sin\alpha)$$

Transport matrices between the stopping target and the wire planes of P3-D2 were formed by multiplying together the transport matrices of (A.9) corresponding to successive short steps along the solenoid axis using the field values in Table (5.1). The initial e^+ track vector at the stopping target may then be determined from a least squares fit to the wire chamber space points.

Appendix B

Positron Energy-Loss Straggling

The e^+ lose energy by ionization (including Bhabba scattering) and bremsstrahlung. The ionization energy-loss ΔE has a much shorter tail than the bremsstrahlung, falling as $1/(\Delta E)^2$ versus $1/\Delta E$ for the bremsstrahlung. Comparison of the formulae given by Tsai[49] shows that the ionization (bremsstrahlung) process dominates for ΔE less (greater) than about 20-MeV/(Z+2.5) where Z is the atomic number of the material. Since the μSR data x range of 0.88-1.00 corresponds to an energy range of 6.3 MeV both processes must be considered.

According to Tsai[49] the probability that an electron with initial energy E_0 has energy $E'>E_0-\Delta_0-\Delta E$ after traversing t radiation lengths, where Δ_0 is the most probable energy-loss due to ionization, is

$$P(E_0,E',t) \approx (1+0.5772bt)\left[\frac{\Delta E}{E_0}\right]^{bt}\left[1 - \frac{\Gamma}{(1-bt)\Delta E}\right] \qquad (B.1)$$

where $\Gamma = 0.154\text{MeV}(Z/A)g$

with g = number of g/cm^2 for t radiation lengths

and $b = (4/3)[1+(Z+1)/9(Z+\eta)\ln(183Z^{-1/3})]$

with $\eta = \ln(1440Z^{-2/3})/\ln(183Z^{-1/3})$

It follows from equation (B.1) that the probability of the straggled energy lying in the range $E_0-\Delta_0-\Delta E_1 < E'' < E_0-\Delta_0-\Delta E_2$ is

$$P(E_0,E'',t) \approx \frac{1+0.5772bt}{E_0{}^{bt}}\{[\Delta E_1{}^{bt}-\Delta E_2{}^{bt}] - \frac{\Gamma}{1-bt}[\Delta E_1{}^{bt-1}-\Delta E_2{}^{bt-1}]\} \qquad (B.2)$$

The radiatively corrected (V-A) differential decay rate [section

(3.3)] was evaluated for $\cos\theta=-1,0,1$ at momentum intervals of $\Delta x=0.0004$ in the range $x=0.88-1.00$. These three momentum spectra were straggled according to equation (B.2) ignoring the most probable ionization energy-loss Δ_0 which is essentially constant over the x range of interest. Equation (B.2) is valid for $\Delta E \geq 10\Gamma$. Consequently the stopping target material and the other material upstream of the spectrometer traversed by the e^+ were each divided into 10 steps and the straggling was performed by successive application of equation (B.2).

Appendix C

Tables of Data Fit Results

Run Period : 1
Target : Ag
B_T : 70-G
Events Fitted: 24457

x Range	$P_\mu A(\tilde{x})$ Gaussian	$P_\mu A(\tilde{x})$ Kubo-Tomita
0.92-0.94	$0.9796^{+0.0194}_{-0.0197}$	$0.9798^{+0.0194}_{-0.0198}$
0.94-0.96	$1.0144^{+0.0160}_{-0.0164}$	$1.0145^{+0.0161}_{-0.0165}$
0.96-0.98	$1.0125^{+0.0132}_{-0.0136}$	$1.0127^{+0.0132}_{-0.0137}$
0.98-1.00	$1.0085^{+0.0105}_{-0.0111}$	$1.0087^{+0.0105}_{-0.0112}$
Mean $P_\mu A(\tilde{x})$	$1.0068^{+0.0070}_{-0.0071}$	$1.0070^{+0.0070}_{-0.0071}$
	χ^2_{913}= 887.35	χ^2_{912}= 887.36

$\cos\theta_e$ Range	$P_\mu A(\tilde{x})$ (Gaussian)
0.975-0.980	$0.9978^{+0.0172}_{-0.0181}$
0.980-0.985	$0.9921^{+0.0159}_{-0.0166}$
0.985-0.990	$1.0272^{+0.0141}_{-0.0150}$
0.990-0.995	$1.0004^{+0.0143}_{-0.0151}$
0.995-1.000	$1.0156^{+0.0138}_{-0.0150}$

t(μs)	$P_\mu A(\tilde{x})G(t)$
0.89	$1.0211^{+0.0095}_{-0.0101}$
1.94	$0.9679^{+0.0145}_{-0.0150}$
3.00	$0.9941^{+0.0156}_{-0.0168}$
4.06	$1.0073^{+0.0193}_{-0.0214}$
5.11	$0.9632^{+0.0273}_{-0.0294}$
6.17	$1.0083^{+0.0272}_{-0.0342}$
7.22	$0.9582^{+0.0445}_{-0.0511}$
8.28	$0.9270^{+0.0587}_{-0.0684}$
9.20	$0.8137^{+0.0905}_{-0.1005}$

Table (C.1)...

Run Period : 1
Target : Al
B_T : 70-G
Events Fitted: 27410

x Range	$P_\mu A(\tilde{x})$ Gaussian	$P_\mu A(\tilde{x})$ Kubo-Tomita
0.92-0.94	$0.9928^{+0.0191}_{-0.0194}$	$0.9980^{+0.0211}_{-0.0205}$
0.94-0.96	$1.0006^{+0.0156}_{-0.0160}$	$1.0055^{+0.0182}_{-0.0172}$
0.96-0.98	$0.9842^{+0.0131}_{-0.0135}$	$0.9896^{+0.0173}_{-0.0151}$
0.98-1.00	$0.9743^{+0.0116}_{-0.0121}$	$0.9798^{+0.0168}_{-0.0138}$
Mean $P_\mu A(\tilde{x})$	$0.9849^{+0.0071}_{-0.0072}$	$0.9927^{+0.0089}_{-0.0087}$
	χ^2_{913}= 916.57	χ^2_{912}= 915.73

$\cos\theta_e$ Range	$P_\mu A(\tilde{x})$ (Gaussian)
0.975-0.980	$1.0024^{+0.0156}_{-0.0165}$
0.980-0.985	$1.0081^{+0.0140}_{-0.0148}$
0.985-0.990	$0.9701^{+0.0143}_{-0.0149}$
0.990-0.995	$0.9728^{+0.0150}_{-0.0156}$
0.995-1.000	$0.9699^{+0.0169}_{-0.0176}$

t(μs)	$P_\mu A(\tilde{x})G(t)$
0.89	$0.9867^{+0.0101}_{-0.0105}$
1.94	$0.9817^{+0.0128}_{-0.0134}$
3.00	$0.9585^{+0.0167}_{-0.0175}$
4.06	$0.9792^{+0.0194}_{-0.0209}$
5.11	$0.9184^{+0.0276}_{-0.0295}$
6.17	$0.9012^{+0.0388}_{-0.0416}$
7.22	$0.9325^{+0.0490}_{-0.0533}$
8.28	$0.9135^{+0.0561}_{-0.0624}$
9.20	$0.9754^{+0.0605}_{-0.0775}$

Table (C.1) cont.

Run Period : 1
Target : Au
B_T : 70-G
Events Fitted: 20174

x Range	$P_\mu A(\tilde{x})$ Gaussian	$P_\mu A(\tilde{x})$ Kubo-Tomita
0.92-0.94	$1.0051^{+0.0209}_{-0.0213}$	$1.0051^{+0.0209}_{-0.0214}$
0.94-0.96	$1.0357^{+0.0174}_{-0.0179}$	$1.0357^{+0.0175}_{-0.0180}$
0.96-0.98	$0.9957^{+0.0146}_{-0.0151}$	$0.9957^{+0.0146}_{-0.0151}$
0.98-1.00	$0.9951^{+0.0120}_{-0.0128}$	$0.9951^{+0.0120}_{-0.0128}$
Mean $P_\mu A(\tilde{x})$	$1.0040^{+0.0077}_{-0.0077}$	$1.0040^{+0.0077}_{-0.0077}$
	$\chi^2_{913} = 1015.16$	$\chi^2_{912} = 1015.18$

$\cos\theta_e$ Range	$P_\mu A(\tilde{x})$ (Gaussian)
0.975-0.980	$1.0223^{+0.0164}_{-0.0177}$
0.980-0.985	$0.9931^{+0.0165}_{-0.0174}$
0.985-0.990	$1.0046^{+0.0160}_{-0.0170}$
0.990-0.995	$1.0179^{+0.0167}_{-0.0176}$
0.995-1.000	$0.9839^{+0.0170}_{-0.0184}$

t (μs)	$P_\mu A(\tilde{x})G(t)$
0.89	$0.9815^{+0.0119}_{-0.0124}$
1.94	$1.0205^{+0.0122}_{-0.0135}$
3.00	$0.9797^{+0.0176}_{-0.0189}$
4.06	$1.0216^{+0.0218}_{-0.0238}$
5.11	$1.0357^{+0.0150}_{-0.0227}$
6.17	$0.9078^{+0.0431}_{-0.0464}$
7.22	$0.9075^{+0.0548}_{-0.0614}$
8.28	$0.9456^{+0.0723}_{-0.0800}$
9.20	$0.6744^{+0.1176}_{-0.1286}$

Table (C.1) cont.

Run Period : 1
Target : Cu*
B_T : 70-G
Events Fitted: 23734

x Range	$P_\mu A(\tilde{x})$ Gaussian	$P_\mu A(\tilde{x})$ Kubo-Tomita
0.92-0.94	$0.9930^{+0.0195}_{-0.0199}$	$0.9930^{-0.0195}_{-0.0199}$
0.94-0.96	$0.9904^{+0.0167}_{-0.0171}$	$0.9905^{+0.0167}_{-0.0171}$
0.96-0.98	$1.0004^{+0.0138}_{-0.0142}$	$1.0005^{+0.0138}_{-0.0143}$
0.98-1.00	$1.0145^{+0.0097}_{-0.0104}$	$1.0145^{+0.0097}_{-0.0104}$
Mean $P_\mu A(\tilde{x})$	$1.0040^{+0.0069}_{-0.0070}$	$1.0041^{+0.0069}_{-0.0070}$
	$\chi^2_{913} = 936.60$	$\chi^2_{912} = 936.60$

$\cos\theta_e$ Range	$P_\mu A(\tilde{x})$ (Gaussian)
0.975-0.980	$0.9916^{+0.0171}_{-0.0181}$
0.980-0.985	$1.0091^{+0.0155}_{-0.0164}$
0.985-0.990	$0.9968^{+0.0151}_{-0.0160}$
0.990-0.995	$0.9957^{+0.0144}_{-0.0154}$
0.995-1.000	$1.0341^{+0.0139}_{-0.0155}$

t (μs)	$P_\mu A(\tilde{x})G(t)$
0.89	$0.9988^{+0.0109}_{-0.0114}$
1.94	$1.0078^{+0.0126}_{-0.0135}$
3.00	$0.9890^{+0.0156}_{-0.0169}$
4.06	$0.9929^{+0.0201}_{-0.0218}$
5.11	$0.9841^{+0.0287}_{-0.0314}$
6.17	$1.0156^{+0.0359}_{-0.0395}$
7.22	$0.9471^{+0.0471}_{-0.0538}$
8.28	$0.8947^{+0.0644}_{-0.0717}$
9.20	$0.8932^{+0.0852}_{-0.0983}$

Table (C.1) cont.

Run Period : 1
Target : He
B_T : 70-G
Events Fitted: 28547

x Range	$P_\mu A(\tilde{x})$ Gaussian	$P_\mu A(\tilde{x})$ Kubo-Tomita
0.92-0.94	$0.8645^{+0.0209}_{-0.0212}$	$0.9124^{+0.0246}_{-0.0247}$
0.94-0.96	$0.8835^{+0.0183}_{-0.0184}$	$0.9321^{+0.0220}_{-0.0222}$
0.96-0.98	$0.8906^{+0.0160}_{-0.0162}$	$0.9396^{+0.0198}_{-0.0199}$
0.98-1.00	$0.8653^{+0.0153}_{-0.0156}$	$0.9147^{+0.0191}_{-0.0194}$
Mean $P_\mu A(\tilde{x})$	$0.8764^{+0.0087}_{-0.0087}$	$0.9252^{+0.0106}_{-0.0106}$
	χ^2_{913}= 910.98	χ^2_{912}= 906.92

$\cos\theta_e$ Range	$P_\mu A(\tilde{x})$ (Gaussian)
0.975-0.980	$0.8956^{+0.0196}_{-0.0202}$
0.980-0.985	$0.8715^{+0.0190}_{-0.0194}$
0.985-0.990	$0.8511^{+0.0186}_{-0.0189}$
0.990-0.995	$0.8900^{+0.0183}_{-0.0187}$
0.995-1.000	$0.8791^{+0.0201}_{-0.0206}$

t (μs)	$P_\mu A(\tilde{x})G(t)$
0.89	$0.8912^{+0.0115}_{-0.0118}$
1.94	$0.8042^{+0.0161}_{-0.0164}$
3.00	$0.8322^{+0.0202}_{-0.0207}$
4.06	$0.7975^{+0.0259}_{-0.0267}$
5.11	$0.7208^{+0.0359}_{-0.0370}$
6.17	$0.6660^{+0.0467}_{-0.0482}$
7.22	$0.6550^{+0.0589}_{-0.0614}$
8.28	$0.4992^{+0.0827}_{-0.0851}$
9.20	$0.5976^{+0.1107}_{-0.1168}$

Table (C.1) cont.

Run Period : 2
Target : Al
B_T : 70-G
Events Fitted: 143335

x Range	$P_\mu A(\tilde{x})$ Gaussian	$P_\mu A(\tilde{x})$ Kubo-Tomita
0.88-0.90	$1.0061^{+0.0139}_{-0.0140}$	$1.0089^{+0.0141}_{-0.0143}$
0.90-0.92	$1.0171^{+0.0118}_{-0.0119}$	$1.0200^{+0.0121}_{-0.0123}$
0.92-0.94	$0.9679^{+0.0103}_{-0.0103}$	$0.9707^{+0.0104}_{-0.0105}$
0.94-0.96	$0.9995^{+0.0086}_{-0.0087}$	$1.0025^{+0.0089}_{-0.0092}$
0.96-0.98	$0.9922^{+0.0074}_{-0.0075}$	$0.9952^{+0.0088}_{-0.0076}$
0.98-1.00	$1.0032^{+0.0062}_{-0.0064}$	$1.0064^{+0.0081}_{-0.0064}$
Mean $P_\mu A(\tilde{x})$	$0.9971^{+0.0036}_{-0.0036}$	$1.0004^{+0.0038}_{-0.0038}$
	χ^2_{1443} = 1529.28	χ^2_{1442} = 1528.77

$\cos\theta_e$ Range	$P_\mu A(\tilde{x})$ (Gaussian)
0.975-0.980	$0.9844^{+0.0109}_{-0.0112}$
0.980-0.985	$0.9925^{+0.0082}_{-0.0083}$
0.985-0.990	$1.0081^{+0.0074}_{-0.0076}$
0.990-0.995	$0.9992^{+0.0072}_{-0.0073}$
0.995-1.000	$0.9936^{+0.0071}_{-0.0072}$

t (μs)	$P_\mu A(\tilde{x})G(t)$
0.64	$1.0027^{+0.0051}_{-0.0052}$
1.70	$0.9685^{+0.0068}_{-0.0069}$
2.76	$0.9508^{+0.0088}_{-0.0090}$
3.82	$0.9427^{+0.0109}_{-0.0112}$
4.87	$0.9107^{+0.0146}_{-0.0149}$
5.93	$0.8707^{+0.0205}_{-0.0210}$
6.99	$0.8484^{+0.0251}_{-0.0260}$
8.05	$0.7220^{+0.0349}_{-0.0358}$
9.08	$0.7112^{+0.0477}_{-0.0492}$

Table (C.1) cont.

Run Period : 2
Target : Au
B_T : 70-G
Events Fitted: 111158

x Range	$P_\mu A(\tilde{x})$ Gaussian	$P_\mu A(\tilde{x})$ Kubo-Tomita
0.88-0.90	$1.0188^{+0.0150}_{-0.0152}$	$1.0195^{+0.0153}_{-0.0155}$
0.90-0.92	$1.0250^{+0.0124}_{-0.0125}$	$1.0257^{+0.0129}_{-0.0129}$
0.92-0.94	$0.9839^{+0.0108}_{-0.0109}$	$0.9846^{+0.0113}_{-0.0113}$
0.94-0.96	$0.9976^{+0.0092}_{-0.0093}$	$0.9983^{+0.0100}_{-0.0098}$
0.96-0.98	$0.9924^{+0.0078}_{-0.0080}$	$0.9931^{+0.0095}_{-0.0085}$
0.98-1.00	$0.9949^{+0.0063}_{-0.0066}$	$0.9957^{+0.0080}_{-0.0072}$
Mean $P_\mu A(\tilde{x})$	$0.9975^{+0.0037}_{-0.0037}$	$0.9989^{+0.0043}_{-0.0042}$
	$\chi^2_{1443} = 1510.97$	$\chi^2_{1442} = 1510.99$

$\cos\theta_e$ Range	$P_\mu A(\tilde{x})$ (Gaussian)
0.975-0.980	$0.9905^{+0.0114}_{-0.0117}$
0.980-0.985	$1.0129^{+0.0085}_{-0.0087}$
0.985-0.990	$0.9911^{+0.0080}_{-0.0082}$
0.990-0.995	$0.9922^{+0.0075}_{-0.0077}$
0.995-1.000	$0.9989^{+0.0074}_{-0.0076}$

t (μs)	$P_\mu A(\tilde{x})G(t)$
0.64	$0.9989^{+0.0057}_{-0.0058}$
1.70	$0.9944^{+0.0072}_{-0.0074}$
2.76	$0.9916^{+0.0089}_{-0.0092}$
3.82	$0.9981^{+0.0115}_{-0.0120}$
4.87	$0.9978^{+0.0138}_{-0.0147}$
5.93	$0.9888^{+0.0182}_{-0.0194}$
6.99	$1.0065^{+0.0213}_{-0.0240}$
8.05	$0.9231^{+0.0344}_{-0.0365}$
9.08	$1.0166^{+0.0343}_{-0.0395}$

Table (C.1) cont.

Run Period : 2
Target : Cu
B_T : 70-G
Events Fitted: 129820

x Range	$P_\mu A(\tilde{x})$ Gaussian	$P_\mu A(\tilde{x})$ Kubo-Tomita
0.88-0.90	$0.9977^{+0.0143}_{-0.0144}$	$0.9977^{+0.0142}_{-0.0144}$
0.90-0.92	$0.9838^{+0.0120}_{-0.0121}$	$0.9839^{+0.0119}_{-0.0121}$
0.92-0.94	$0.9928^{+0.0101}_{-0.0102}$	$0.9929^{+0.0101}_{-0.0102}$
0.94-0.96	$0.9819^{+0.0088}_{-0.0089}$	$0.9820^{+0.0088}_{-0.0089}$
0.96-0.98	$0.9851^{+0.0075}_{-0.0076}$	$0.9852^{+0.0075}_{-0.0076}$
0.98-1.00	$0.9796^{+0.0064}_{-0.0065}$	$0.9797^{+0.0064}_{-0.0065}$
Mean $P_\mu A(\tilde{x})$	$0.9844^{+0.0036}_{-0.0036}$	$0.9845^{+0.0036}_{-0.0036}$
	$\chi^2_{1443} = 1424.57$	$\chi^2_{1442} = 1424.54$

$\cos\theta_e$ Range	$P_\mu A(\tilde{x})$ (Gaussian)
0.975-0.980	$0.9865^{+0.0088}_{-0.0090}$
0.980-0.985	$0.9823^{+0.0082}_{-0.0084}$
0.985-0.990	$0.9915^{+0.0077}_{-0.0079}$
0.990-0.995	$0.9806^{+0.0075}_{-0.0076}$
0.995-1.000	$0.9866^{+0.0071}_{-0.0072}$

t (μs)	$P_\mu A(\tilde{x})G(t)$
0.64	$0.9841^{+0.0054}_{-0.0054}$
1.70	$0.9792^{+0.0071}_{-0.0072}$
2.76	$0.9792^{+0.0086}_{-0.0088}$
3.82	$0.9641^{+0.0114}_{-0.0117}$
4.87	$0.9799^{+0.0135}_{-0.0140}$
5.93	$0.9340^{+0.0192}_{-0.0200}$
6.99	$0.9289^{+0.0247}_{-0.0259}$
8.05	$0.9656^{+0.0283}_{-0.0304}$
9.08	$0.9123^{+0.0444}_{-0.0476}$

Table (C.1) cont.

Run Period 2; Target = Al; B_T = 110-G; Events Fitted = 58529

x Range	$P_\mu A(\tilde{x})$ Gaussian	$P_\mu A(\tilde{x})$ Kubo-Tomita
0.88-0.90	$0.9839^{+0.0212}_{-0.0214}$	$0.9940^{+0.0227}_{-0.0225}$
0.90-0.92	$1.0187^{+0.0178}_{-0.0180}$	$1.0290^{+0.0195}_{-0.0193}$
0.92-0.94	$1.0163^{+0.0154}_{-0.0157}$	$1.0260^{+0.0171}_{-0.0169}$
0.94-0.96	$1.0026^{+0.0130}_{-0.0133}$	$1.0117^{+0.0149}_{-0.0146}$
0.96-0.98	$0.9946^{+0.0110}_{-0.0113}$	$1.0033^{+0.0130}_{-0.0126}$
0.98-1.00	$0.9909^{+0.0096}_{-0.0100}$	$1.0000^{+0.0119}_{-0.0115}$
Mean $P_\mu A(\tilde{x})$	$0.9988^{+0.0054}_{-0.0054}$	$1.0090^{+0.0062}_{-0.0062}$
	χ^2_{1443}= 1525.59	χ^2_{1442}= 1522.12

$\cos\theta_e$ Range	$P_\mu A(\tilde{x})$ (Gaussian)
0.975-0.980	$0.9864^{+0.0170}_{-0.0176}$
0.980-0.985	$0.9844^{+0.0130}_{-0.0133}$
0.985-0.990	$1.0084^{+0.0114}_{-0.0118}$
0.990-0.995	$0.9956^{+0.0110}_{-0.0114}$
0.995-1.000	$1.0092^{+0.0105}_{-0.0109}$

t (μs)	$P_\mu A(\tilde{x})G(t)$
0.44	$0.9991^{+0.0092}_{-0.0095}$
1.09	$1.0004^{+0.0101}_{-0.0106}$
1.75	$0.9765^{+0.0130}_{-0.0135}$
2.40	$0.9729^{+0.0151}_{-0.0157}$
3.05	$0.9375^{+0.0191}_{-0.0198}$
3.71	$0.9461^{+0.0212}_{-0.0223}$
4.36	$0.9333^{+0.0252}_{-0.0265}$
5.01	$0.8778^{+0.0302}_{-0.0316}$
5.67	$0.7990^{+0.0388}_{-0.0404}$
6.32	$0.8596^{+0.0418}_{-0.0443}$
6.97	$0.8437^{+0.0488}_{-0.0520}$
7.63	$0.8129^{+0.0571}_{-0.0613}$
8.28	$0.8483^{+0.0619}_{-0.0751}$
9.10	$0.7861^{+0.0742}_{-0.0798}$

Table (C.1) cont.

Run Period 2; Target = Al*; B_T = 110-G; Events Fitted = 55445

x Range	$P_\mu A(\tilde{x})$ Gaussian	$P_\mu A(\tilde{x})$ Kubo-Tomita
0.88-0.90	$0.9701^{+0.0221}_{-0.0224}$	$0.9832^{+0.0230}_{-0.0245}$
0.90-0.92	$0.9857^{+0.0185}_{-0.0187}$	$0.9989^{+0.0222}_{-0.0193}$
0.92-0.94	$1.0046^{+0.0156}_{-0.0158}$	$1.0191^{+0.0243}_{-0.0166}$
0.94-0.96	$0.9929^{+0.0134}_{-0.0136}$	$1.0067^{+0.0208}_{-0.0166}$
0.96-0.98	$1.0034^{+0.0109}_{-0.0112}$	$1.0167^{+0.0120}_{-0.0143}$
0.98-1.00	$0.9991^{+0.0090}_{-0.0095}$	$1.0117^{+0.0181}_{-0.0103}$
Mean $P_\mu A(\tilde{x})$	$0.9968^{+0.0054}_{-0.0055}$	$1.0100^{+0.0067}_{-0.0064}$
	χ^2_{1443}= 1537.18	χ^2_{1442}= 1533.17

$\cos\theta_e$ Range	$P_\mu A(\tilde{x})$ (Gaussian)
0.975-0.980	$1.0116^{+0.0151}_{-0.0158}$
0.980-0.985	$0.9864^{+0.0122}_{-0.0127}$
0.985-0.990	$1.0070^{+0.0113}_{-0.0117}$
0.990-0.995	$0.9933^{+0.0112}_{-0.0115}$
0.995-1.000	$0.9938^{+0.0106}_{-0.0107}$

t (μs)	$P_\mu A(\tilde{x})G(t)$
0.44	$1.0011^{+0.0090}_{-0.0094}$
1.09	$1.0097^{+0.0104}_{-0.0110}$
1.75	$0.9606^{+0.0136}_{-0.0141}$
2.40	$0.9798^{+0.0153}_{-0.0160}$
3.05	$0.9592^{+0.0196}_{-0.0204}$
3.71	$0.9042^{+0.0239}_{-0.0247}$
4.36	$0.9359^{+0.0259}_{-0.0273}$
5.01	$0.8902^{+0.0324}_{-0.0338}$
5.67	$0.9028^{+0.0353}_{-0.0376}$
6.32	$0.9033^{+0.0419}_{-0.0449}$
6.97	$0.8621^{+0.0501}_{-0.0534}$
7.63	$0.7901^{+0.0632}_{-0.0669}$
8.28	$0.8946^{+0.0712}_{-0.0781}$
9.10	$0.8177^{+0.0829}_{-0.0895}$

Table (C.1) cont.

Run Period 2; Target = Au; B_T = 110-G; Events Fitted = 28456

x Range	$P_\mu A(\tilde{x})$ Gaussian	$P_\mu A(\tilde{x})$ Kubo-Tomita
0.88-0.90	$0.9756^{+0.0290}_{-0.0295}$	$0.9756^{+0.0290}_{-0.0295}$
0.90-0.92	$1.0264^{+0.0243}_{-0.0247}$	$1.0264^{+0.0243}_{-0.0247}$
0.92-0.94	$0.9886^{+0.0210}_{-0.0215}$	$0.9886^{+0.0211}_{-0.0214}$
0.94-0.96	$1.0144^{+0.0174}_{-0.0179}$	$1.0144^{+0.0174}_{-0.0179}$
0.96-0.98	$0.9698^{+0.0154}_{-0.0159}$	$0.9697^{+0.0155}_{-0.0159}$
0.98-1.00	$0.9969^{+0.0122}_{-0.0131}$	$0.9969^{+0.0123}_{-0.0131}$
Mean $P_\mu A(\tilde{x})$	$0.9939^{+0.0074}_{-0.0074}$	$0.9939^{+0.0074}_{-0.0074}$
	χ^2_{1443}= 1561.77	χ^2_{1442}= 1561.77

$\cos\theta_e$ Range	$P_\mu A(\tilde{x})$ (Gaussian)
0.975-0.980	$0.9664^{+0.0253}_{-0.0263}$
0.980-0.985	$1.0041^{+0.0159}_{-0.0169}$
0.985-0.990	$0.9774^{+0.0153}_{-0.0160}$
0.990-0.995	$1.0215^{+0.0136}_{-0.0146}$
0.995-1.000	$0.9854^{+0.0150}_{-0.0158}$

t (μs)	$P_\mu A(\tilde{x})G(t)$
0.44	$0.9955^{+0.0129}_{-0.0137}$
1.09	$0.9874^{+0.0169}_{-0.0175}$
1.75	$0.9936^{+0.0174}_{-0.0184}$
2.40	$0.9902^{+0.0203}_{-0.0217}$
3.05	$0.9517^{+0.0262}_{-0.0277}$
3.71	$1.0311^{+0.0167}_{-0.0228}$
4.36	$0.9655^{+0.0321}_{-0.0355}$
5.01	$0.9875^{+0.0354}_{-0.0409}$
5.67	$1.0901^{+0.0354}_{-0.0424}$
6.32	$0.9435^{+0.0611}_{-0.0667}$
6.97	$0.9614^{+0.0525}_{-0.0630}$
7.63	$0.9824^{+0.0561}_{-0.0713}$
8.28	$0.9185^{+0.0762}_{-0.0948}$
9.10	$0.9928^{+0.1075}_{-0.1224}$

Table (C.1) cont.

Run Period 2; Target = Cu; B_T = 110-G; Events Fitted = 41924

x Range	$P_\mu A(\tilde{x})$ Gaussian	$P_\mu A(\tilde{x})$ Kubo-Tomita
0.88-0.90	$0.9758^{+0.0245}_{-0.0248}$	$0.9838^{+0.0256}_{-0.0257}$
0.90-0.92	$0.9701^{+0.0211}_{-0.0214}$	$0.9779^{+0.0223}_{-0.0224}$
0.92-0.94	$0.9900^{+0.0180}_{-0.0183}$	$0.9982^{+0.0194}_{-0.0195}$
0.94-0.96	$1.0216^{+0.0143}_{-0.0146}$	$1.0298^{+0.0159}_{-0.0161}$
0.96-0.98	$0.9783^{+0.0129}_{-0.0132}$	$0.9866^{+0.0146}_{-0.0147}$
0.98-1.00	$0.9514^{+0.0120}_{-0.0124}$	$0.9594^{+0.0138}_{-0.0140}$
Mean $P_\mu A(\tilde{x})$	$0.9795^{+0.0064}_{-0.0064}$	$0.9882^{+0.0071}_{-0.0071}$
	χ^2_{1443}= 1478.43	χ^2_{1442}= 1477.57

$\cos\theta_e$ Range	$P_\mu A(\tilde{x})$ (Gaussian)
0.975-0.980	$0.9699^{+0.0156}_{-0.0162}$
0.980-0.985	$0.9590^{+0.0142}_{-0.0146}$
0.985-0.990	$0.9819^{+0.0131}_{-0.0136}$
0.990-0.995	$0.9758^{+0.0131}_{-0.0135}$
0.995-1.000	$0.9932^{+0.0117}_{-0.0122}$

t (μs)	$P_\mu A(\tilde{x})G(t)$
0.44	$0.9812^{+0.0114}_{-0.0117}$
1.09	$0.9991^{+0.0127}_{-0.0133}$
1.75	$0.9556^{+0.0157}_{-0.0164}$
2.40	$0.9530^{+0.0185}_{-0.0192}$
3.05	$0.9698^{+0.0198}_{-0.0210}$
3.71	$0.9393^{+0.0241}_{-0.0255}$
4.36	$0.9452^{+0.0277}_{-0.0298}$
5.01	$0.9481^{+0.0337}_{-0.0361}$
5.67	$0.9846^{+0.0301}_{-0.0346}$
6.32	$0.9768^{+0.0457}_{-0.0498}$
6.97	$0.9663^{+0.0470}_{-0.0551}$
7.63	$0.9420^{+0.0588}_{-0.0658}$
8.28	$0.9413^{+0.0614}_{-0.0732}$
9.10	$0.8869^{+0.0776}_{-0.0898}$

Table (C.1) cont.

Run Period 2; Target = Cu*; B_T = 110-G; Events Fitted = 39244

x Range	$P_\mu A(\tilde{x})$ Gaussian	$P_\mu A(\tilde{x})$ Kubo-Tomita
0.88-0.90	$0.9577^{+0.0258}_{-0.0262}$	$0.9680^{+0.0269}_{-0.0273}$
0.90-0.92	$0.9682^{+0.0216}_{-0.0220}$	$0.9795^{+0.0230}_{-0.0233}$
0.92-0.94	$0.9641^{+0.0189}_{-0.0192}$	$0.9747^{+0.0205}_{-0.0205}$
0.94-0.96	$0.9704^{+0.0159}_{-0.0162}$	$0.9813^{+0.0172}_{-0.0178}$
0.96-0.98	$0.9938^{+0.0129}_{-0.0133}$	$1.0053^{+0.0150}_{-0.0153}$
0.98-1.00	$0.9759^{+0.0114}_{-0.0119}$	$0.9873^{+0.0133}_{-0.0139}$
Mean $P_\mu A(\tilde{x})$	$0.9760^{+0.0065}_{-0.0066}$	$0.9865^{+0.0073}_{-0.0074}$
	χ^2_{1443}= 1521.30	χ^2_{1442}= 1519.18

$\cos\theta_e$ Range	$P_\mu A(\tilde{x})$ (Gaussian)
0.975-0.980	$0.9714^{+0.0164}_{-0.0170}$
0.980-0.985	$0.9794^{+0.0146}_{-0.0151}$
0.985-0.990	$0.9886^{+0.0140}_{-0.0145}$
0.990-0.995	$0.9793^{+0.0133}_{-0.0139}$
0.995-1.000	$0.9678^{+0.0130}_{-0.0134}$

t (μs)	$P_\mu A(\tilde{x})G(t)$
0.44	$1.0006^{+0.0114}_{-0.0119}$
1.09	$0.9491^{+0.0147}_{-0.0151}$
1.75	$0.9863^{+0.0149}_{-0.0158}$
2.40	$0.9584^{+0.0180}_{-0.0189}$
3.05	$0.9359^{+0.0227}_{-0.0238}$
3.71	$0.9724^{+0.0268}_{-0.0282}$
4.36	$0.9315^{+0.0317}_{-0.0334}$
5.01	$0.9338^{+0.0341}_{-0.0364}$
5.67	$1.0186^{+0.0295}_{-0.0358}$
6.32	$0.8217^{+0.0566}_{-0.0598}$
6.97	$0.9673^{+0.0533}_{-0.0598}$
7.63	$0.9587^{+0.0599}_{-0.0677}$
8.28	$0.9426^{+0.0674}_{-0.0800}$
9.10	$0.9246^{+0.0772}_{-0.0884}$

Table (C.1) cont.

Run Period 3; Target = Al; B_T = 110-G; Events Fitted = 98282

x Range	$P_\mu A(\tilde{x})$ Gaussian	$P_\mu A(\tilde{x})$ Kubo-Tomita
0.88-0.90	$0.9766^{+0.0169}_{-0.0171}$	$0.9837^{+0.0181}_{-0.0180}$
0.90-0.92	$0.9800^{+0.0143}_{-0.0144}$	$0.9864^{+0.0155}_{-0.0153}$
0.92-0.94	$1.0225^{+0.0118}_{-0.0120}$	$1.0295^{+0.0135}_{-0.0131}$
0.94-0.96	$0.9894^{+0.0104}_{-0.0105}$	$0.9963^{+0.0122}_{-0.0117}$
0.96-0.98	$0.9824^{+0.0088}_{-0.0090}$	$0.9894^{+0.0110}_{-0.0103}$
0.98-1.00	$1.0009^{+0.0069}_{-0.0071}$	$1.0080^{+0.0097}_{-0.0087}$
Mean $P_\mu A(\tilde{x})$	$0.9942^{+0.0042}_{-0.0042}$	$1.0014^{+0.0049}_{-0.0049}$
	χ^2_{1220}= 1241.78	χ^2_{1219}= 1239.12

$\cos\theta_e$ Range	$P_\mu A(\tilde{x})$ (Gaussian)
0.975-0.980	$0.9994^{+0.0105}_{-0.0108}$
0.980-0.985	$1.0095^{+0.0097}_{-0.0099}$
0.985-0.990	$0.9918^{+0.0093}_{-0.0096}$
0.990-0.995	$0.9820^{+0.0090}_{-0.0092}$
0.995-1.000	$0.9916^{+0.0086}_{-0.0088}$

t (μs)	$P_\mu A(\tilde{x})G(t)$
0.44	$0.9996^{+0.0072}_{-0.0074}$
1.09	$0.9884^{+0.0085}_{-0.0087}$
1.75	$0.9763^{+0.0100}_{-0.0103}$
2.40	$0.9579^{+0.0120}_{-0.0123}$
3.05	$0.9565^{+0.0140}_{-0.0144}$
3.71	$0.9400^{+0.0169}_{-0.0174}$
4.36	$0.9360^{+0.0193}_{-0.0200}$
5.01	$0.8937^{+0.0234}_{-0.0243}$
5.67	$0.8192^{+0.0298}_{-0.0308}$
6.32	$0.8626^{+0.0326}_{-0.0339}$
6.97	$0.8783^{+0.0402}_{-0.0420}$
7.63	$0.8546^{+0.0437}_{-0.0457}$

Table (C.1) cont.

Run	Target	B_T(G)	χ^2_{919}	$P_\mu A(\tilde{x})$	Statistical Error	
194	Ag	70	851.1	1.0172	+0.0213	-0.0235
206	Ag	70	888.4	1.0022	+0.0178	-0.0192
214	Ag	70	910.7	0.9728	+0.0191	-0.0202
228	Ag	70	893.7	1.0013	+0.0170	-0.0178
316	Ag	70	841.3	1.0484	+0.0156	-0.0181
340	Ag	70	924.9	1.0007	+0.0178	-0.0190
352	Ag	70	962.7	1.0158	+0.0153	-0.0165
183	Al	70	846.8	1.0029	+0.0161	-0.0174
199	Al	70	839.8	1.0089	+0.0289	-0.0315
200	Al	70	836.1	0.9813	+0.0232	-0.0250
209	Al	70	872.1	0.9696	+0.0191	-0.0202
234	Al	70	941.9	0.9671	+0.0190	-0.0198
292	Al	70	923.2	1.0078	+0.0192	-0.0205
308	Al	70	867.8	0.9890	+0.0215	-0.0230
317	Al	70	890.5	0.9603	+0.0213	-0.0226
347	Al	70	899.7	0.9866	+0.0178	-0.0192
186	Au	70	896.8	0.9449	+0.0225	-0.0237
210	Au	70	950.9	1.0053	+0.0191	-0.0203
220	Au	70	916.8	1.0093	+0.0149	-0.0162
312	Au	70	976.3	1.0169	+0.0186	-0.0208
324	Au	70	908.4	1.0317	+0.0151	-0.0172
348	Au	70	905.4	1.0065	+0.0173	-0.0186
191	Cu*	70	862.0	1.0079	+0.0247	-0.0269
205	Cu*	70	870.9	0.9972	+0.0180	-0.0194
213	Cu*	70	936.1	0.9922	+0.0184	-0.0196
227	Cu*	70	930.9	1.0268	+0.0131	-0.0146
313	Cu*	70	868.9	1.0038	+0.0180	-0.0196
339	Cu*	70	916.2	0.9898	+0.0196	-0.0207
353	Cu*	70	849.7	1.0023	+0.0176	-0.0185
233	He	70	887.2	0.8509	+0.0228	-0.0233
235	He	70	911.2	0.8924	+0.0215	-0.0222
240	He	70	952.7	0.8838	+0.0237	-0.0245
241	He	70	882.4	0.8575	+0.0244	-0.0251
245	He	70	812.0	0.8609	+0.0410	-0.0427
251	He	70	903.1	0.8467	+0.0255	-0.0262
301	He	70	947.0	0.8645	+0.0253	-0.0261
325	He	70	943.3	0.9561	+0.0229	-0.0240
362	He	70	838.7	0.8728	+0.0350	-0.0363

Table (C.2)...

Run	Target	B_T(G)	χ^2_{1451}	$P_\mu A(\tilde{x})$	Statistical Error	
409	Al	70	1478.1	1.0126	+0.0147	-0.0154
411	Al	70	1542.3	1.0186	+0.0145	-0.0151
419	Al	70	1444.5	1.0138	+0.0180	-0.0191
434	Al	70	1541.5	0.9559	+0.0187	-0.0193
435	Al	70	1487.7	0.9794	+0.0185	-0.0192
442	Al	70	1512.2	0.9723	+0.0185	-0.0192
443	Al	70	1530.0	0.9998	+0.0193	-0.0202
454	Al	70	1514.8	0.9789	+0.0172	-0.0180
468	Al	70	1544.3	0.9801	+0.0198	-0.0207
469	Al	70	1435.4	1.0254	+0.0184	-0.0194
492	Al	70	1515.0	0.9959	+0.0133	-0.0138
503	Al	70	1499.9	0.9914	+0.0149	-0.0154
504	Al	70	1394.3	0.9932	+0.0140	-0.0146
517	Al	70	1512.4	1.0027	+0.0153	-0.0160
518	Al	70	1494.6	0.9953	+0.0182	-0.0189
529	Al	70	1557.4	1.0095	+0.0173	-0.0181
530	Al	70	1535.2	0.9931	+0.0167	-0.0174
541	Al	70	1424.7	1.0091	+0.0167	-0.0174
542	Al	70	1507.2	1.0131	+0.0175	-0.0183
549	Al	70	1489.3	0.9912	+0.0171	-0.0177
550	Al	70	1544.7	0.9856	+0.0171	-0.0181
561	Al	70	1470.5	1.0068	+0.0149	-0.0156
562	Al	70	1444.4	0.9723	+0.0173	-0.0180
579	Al	110	1557.1	1.0074	+0.0149	-0.0159
580	Al	110	1532.1	1.0249	+0.0166	-0.0173
592	Al	110	1412.0	1.0186	+0.0131	-0.0141
593	Al	110	1522.8	0.9752	+0.0161	-0.0167
619	Al	110	1489.9	0.9784	+0.0181	-0.0188
620	Al	110	1373.0	0.9748	+0.0190	-0.0197
716	Al	110	1487.7	0.9887	+0.0172	-0.0178
717	Al	110	1479.2	1.0202	+0.0149	-0.0159
723	Al	110	1474.6	0.9821	+0.0174	-0.0182
724	Al	110	1534.0	0.9948	+0.0165	-0.0173
663	Al*	110	1425.1	1.0222	+0.0150	-0.0163
664	Al*	110	1502.8	0.9605	+0.0185	-0.0191
673	Al*	110	1464.3	1.0014	+0.0160	-0.0170
674	Al*	110	1523.2	0.9804	+0.0168	-0.0175
691	Al*	110	1472.2	1.0020	+0.0164	-0.0172
692	Al*	110	1464.5	1.0148	+0.0160	-0.0170
699	Al*	110	1572.1	0.9673	+0.0183	-0.0189
700	Al*	110	1440.6	0.9977	+0.0174	-0.0183
707	Al*	110	1518.7	1.0043	+0.0159	-0.0167
708	Al*	110	1549.9	0.9844	+0.0160	-0.0167

Table (C.2) cont.

Run	Target	B_T(G)	χ^2_{1451}	$P_\mu A(\tilde{x})$	Statistical Error	
418	Au	70	1390.3	0.9686	+0.0201	-0.0210
430	Au	70	1409.2	0.9790	+0.0156	-0.0165
431	Au	70	1445.2	1.0137	+0.0150	-0.0162
446	Au	70	1443.8	1.0001	+0.0162	-0.0171
447	Au	70	1510.7	1.0090	+0.0132	-0.0143
472	Au	70	1425.3	1.0137	+0.0175	-0.0188
473	Au	70	1421.5	1.0138	+0.0172	-0.0189
495	Au	70	1576.2	1.0020	+0.0143	-0.0150
507	Au	70	1399.5	0.9933	+0.0172	-0.0182
508	Au	70	1474.7	0.9937	+0.0150	-0.0162
521	Au	70	1401.2	1.0115	+0.0139	-0.0147
522	Au	70	1454.3	0.9890	+0.0148	-0.0152
533	Au	70	1414.5	1.0116	+0.0153	-0.0165
534	Au	70	1412.4	0.9682	+0.0183	-0.0190
545	Au	70	1495.5	0.9877	+0.0160	-0.0168
546	Au	70	1529.2	0.9927	+0.0153	-0.0163
553	Au	70	1412.5	1.0017	+0.0165	-0.0174
554	Au	70	1461.5	0.9759	+0.0176	-0.0184
565	Au	70	1538.2	0.9798	+0.0146	-0.0152
566	Au	70	1410.1	0.9999	+0.0170	-0.0181
567	Au	70	1273.9	1.0264	+0.0264	-0.0289
583	Au	110	1535.3	1.0254	+0.0125	-0.0131
584	Au	110	1485.9	0.9834	+0.0147	-0.0152
596	Au	110	1512.4	0.9910	+0.0146	-0.0153
597	Au	110	1448.6	0.9742	+0.0146	-0.0152
414	Cu	70	1356.3	0.9940	+0.0219	-0.0231
415	Cu	70	1515.9	0.9838	+0.0172	-0.0180
426	Cu	70	1457.1	0.9837	+0.0169	-0.0176
427	Cu	70	1456.5	0.9765	+0.0160	-0.0167
440	Cu	70	1400.1	0.9871	+0.0163	-0.0171
441	Cu	70	1526.2	0.9630	+0.0180	-0.0187
450	Cu	70	1445.7	0.9691	+0.0187	-0.0194
451	Cu	70	1458.4	0.9786	+0.0181	-0.0189
464	Cu	70	1448.7	0.9796	+0.0166	-0.0175
465	Cu	70	1500.4	0.9940	+0.0174	-0.0185
487	Cu	70	1531.3	1.0075	+0.0117	-0.0123
488	Cu	70	1462.8	0.9740	+0.0174	-0.0182
489	Cu	70	1497.0	0.9933	+0.0138	-0.0143
499	Cu	70	1409.1	0.9658	+0.0234	-0.0247
500	Cu	70	1531.3	0.9954	+0.0154	-0.0162
513	Cu	70	1421.6	0.9909	+0.0146	-0.0152
514	Cu	70	1430.2	0.9985	+0.0143	-0.0150

Table (C.2) cont.

Run	Target	B_T(G)	χ^2_{1451}	$P_\mu A(\tilde{x})$	Statistical Error	
525	Cu	70	1437.6	0.9686	+0.0156	-0.0164
526	Cu	70	1458.8	0.9755	+0.0185	-0.0192
537	Cu	70	1412.3	0.9984	+0.0162	-0.0171
538	Cu	70	1511.5	0.9830	+0.0169	-0.0178
557	Cu	70	1473.8	0.9769	+0.0173	-0.0181
558	Cu	70	1474.8	0.9945	+0.0169	-0.0176
575	Cu	110	1520.0	0.9920	+0.0118	-0.0122
576	Cu	110	1612.0	0.9629	+0.0165	-0.0171
588	Cu	110	1442.1	0.9903	+0.0140	-0.0147
589	Cu	110	1531.7	0.9711	+0.0144	-0.0149
712	Cu	110	1446.6	0.9705	+0.0162	-0.0169
713	Cu	110	1503.2	0.9587	+0.0166	-0.0172
600	Cu*	110	1481.2	0.9683	+0.0158	-0.0164
601	Cu*	110	1473.0	0.9747	+0.0172	-0.0180
669	Cu*	110	1533.0	0.9993	+0.0159	-0.0167
695	Cu*	110	1507.4	0.9529	+0.0183	-0.0190
696	Cu*	110	1497.5	0.9869	+0.0182	-0.0189
703	Cu*	110	1433.1	0.9744	+0.0156	-0.0163
704	Cu*	110	1520.9	0.9858	+0.0163	-0.0170

Run	Target	B_T(G)	χ^2_{1229}	$P_\mu A(\tilde{x})$	Statistical Error	
883	Al	110	1305.1	1.0018	+0.0175	-0.0183
884	Al	110	1271.9	0.9703	+0.0153	-0.0158
890	Al	110	1353.9	1.0101	+0.0144	-0.0151
896	Al	110	1400.9	1.0033	+0.0132	-0.0139
903	Al	110	1325.9	1.0038	+0.0150	-0.0156
909	Al	110	1303.9	0.9900	+0.0140	-0.0145
914	Al	110	1285.5	1.0112	+0.0149	-0.0155
921	Al	110	1197.7	0.9859	+0.0163	-0.0169
928	Al	110	1357.0	1.0074	+0.0128	-0.0133
934	Al	110	1359.3	0.9908	+0.0126	-0.0131
940	Al	110	1346.3	0.9957	+0.0135	-0.0140
947	Al	110	1363.6	0.9620	+0.0149	-0.0153

Table (C.2) cont.

References

1. S.L. Glashow, Nucl. Phys. 22, 579 (1961).
2. S. Weinberg, Phys. Rev. Lett. 19, 1264 (1967).
3. A. Salam, Proc. 8th Nobel Symposium, Aspenasgarden (Almqvist and Wiskell, Stockholm, 1968).
4. E.M. Lipmanov, Yad. Fiz. 6, 541 (1967) [Sov. J. Nucl. Phys. 6, 395 (1968)].
5. J.C. Pati and A. Salam, Phys. Rev. Lett. 31, 661 (1973) and Phys. Rev. D10, 275 (1974).
6. R.N. Mohapatra and J.C. Pati, Phys. Rev. D11, 566, 2588 (1975).
7. G. Senjanovic and R.N. Mohapatra, Phys. Rev. D12, 1502 (1975).
8. A.E. Pifer et al., Nucl. Instr. Meth. 135, 39 (1976).
9. J. Carr et al., Phys. Rev. Lett. 51, 627 (1983).
10. G. Arnison et al., Phys. Lett. 122B, 103 (1983) and 126B, 398 (1983).
11. M. Banner et al., Phys. Lett. 122B, 476 (1983).
12. W.J. Marciano and A. Sirlin, Phys. Rev. D29, 945 (1984).
13. G. Senjanovic, Nucl. Phys. B153, 334 (1979).
14. M. Gell-Mann, P. Ramond and R. Slansky, unpublished.
15. R.N. Mohapatra and G. Senjanovic, Phys. Rev. Lett. 44, 912 (1980) and Phys. Rev. D23, 165 (1981).
16. H. Abramowicz et al., Z. Phys. C12, 225 (1982).
17. Primary input to the world average is V.V. Akhmanov et al., Yad. Fiz. 6, 316 (1967) [Sov. J. Nucl. Phys. 6, 230 (1968)].
18. Primary input to the world average is J. Peoples, Nevis Cyclotron Report No. 147 (1966).

19. J. Van Klinken, Nucl. Phys. 75, 145 (1966).

20. J. Van Klinken et al., Phys. Rev. Lett. 50, 94 (1983).

21. D. Schreiber and F.T. Calaprice, private communication; D. Schreiber, Ph.D. thesis, Princeton University, 1983 (unpublished); F.T. Calaprice et al., Phys. Rev. Lett. 35, 1566 (1975).

22. T. Vitale et al. (unpublished) quoted by B.R. Holstein and S.B. Treiman, Phys. Rev. D16, 2369 (1977).

23. L. Wolfenstein, Phys. Rev. D29, 2130 (1984).

24. J. Donahue and B. Holstein, Phys. Lett 113B, 382 (1982). See also I.I. Bigi and J.M. Frere, Phys. Lett. 110B, 255 (1982).

25. G. Beall et al., Phys. Rev. Lett. 48, 848 (1982).

26. F.J. Gilman and M.H. Reno, Phys. Lett. 127B, 426 (1983).

27. P. DeForcrand, Ph.D. thesis, Univ. of Calif., Berkeley (1982), Lawrence Berkeley Laboratory Report No. LBL-14692.

28. T.D. Lee and C.N. Yang, Phys. Rev. 108, 1611 (1957).

29. F. Scheck, Phys. Lett. C44, 187 (1978).

30. A.M. Sachs and A. Sirlin, in Muon Physics, Vol. II, V. Hughes and C.S. Wu, eds. (Academic Press, N.Y., 1975), p.50.

31. C.G. Wohl et al. (Particle Data Group), Rev. Mod. Phys. 56, S1 (1984). Primary input to ρ is Ref. 18; primary input to η is F. Corriveau et al., Phys. Lett. 129B, 260 (1983) and S.E. Derenzo, Phys.Rev. 181, 1854 (1969); primary input to ξP_μ is Ref. 17; primary input to $\xi P_\mu \delta/\rho$ is Ref. 9; primary input to δ is D. Fryberger, Phys. Rev. 166, 1379 (1968).

32. M.A.B. Beg et al., Phys. Rev. Lett. 38, 1252 (1977).

33. W.E. Fischer and F. Scheck, Nucl. Phys. B83, 25 (1974).

34. V. Florescu and O. Kamei, Nuovo Cimento 61A, 967 (1968).

35. M.A.B. Beg and A. Sirlin, Ann. Rev. Nucl. Sci. 24, 579 (1974).

36. K. Mursula and F. Scheck, Nucl. Phys. B253, 189 (1985).

37. J.H. Brewer et al., in Muon Physics, Vol. III, V. Hughes and C.S. Wu eds. (Academic Press, N.Y., 1975), p.4.

38. G.W. Ford and C.J. Mullin, Phys. Rev. 108, 477 (1957).

39. V. Hughes, Phys. Rev. 108, 1106 (1957).

40. Proceedings of recent μSR conferences are contained in Hyperfine Interactions 6 (1979) and 17-19 (1984).

41. D. Richter, in Neutron Scattering and Muon Spin Rotation, Springer Tracts in Modern Physics 101 (Springer-Verlag 1983) p.85.

42. R. Kubo and K. Tomita, J. Phys. Soc. Jpn 9, 888 (1954).

43. J.H. van Vleck, Phys. Rev. 74, 1168 (1948).

44. K.W. Kehr et al., Z. Phys. B32, 49 (1978).

45. A.P. Mills, Proc. 6th Int. Conf. on Positron Annihilation, P.G. Coleman, S.C. Sharma, and L.M. Diana eds. (North-Holland, Amsterdam 1982) p.121.

46. C.J. Oram et al., Nucl. Instr. Meth. 179, 95 (1981).

47. R. Sagane et al., Phys. Rev. 95, 863 (1954).

48. K. Halbach, private communication.

49. Y.S. Tsai, SLAC-PUB-848 (1971).

50. B.P. Nigam et al., Phys. Rev. 115, 491 (1959).

51. J.B. Marion and B.A. Zimmerman, Nucl. Instr. Meth. 51, 93 (1967).

52. A.P. Rekalo, Ukr. Fiz. Zh. 16(12), 1937 (1971) and Yad. Fiz. 13(6), 1288 (1971) [Sov. J. Nucl. Phys. 13(6) 741 (1971)].

53. B. Balke et al., Lawrence Berkeley Laboratory Report No. LBL-18320.

54. M. Abolins et al., Proc. 1982 DPF Summer Study Elem. Part. Phys. and Future Facilities p.274 (Snowmass, 1982).

55. E.J. Eichten et al., Phys. Rev. Lett. 50, 811 (1983).

56. M.E. Peskin, private communication.

57. K.D. Lane and E. Barany, private communication.

This report was done with support from the Department of Energy. Any conclusions or opinions expressed in this report represent solely those of the author(s) and not necessarily those of The Regents of the University of California, the Lawrence Berkeley Laboratory or the Department of Energy.

Reference to a company or product name does not imply approval or recommendation of the product by the University of California or the U.S. Department of Energy to the exclusion of others that may be suitable.

LAWRENCE BERKELEY LABORATORY
TECHNICAL INFORMATION DEPARTMENT
UNIVERSITY OF CALIFORNIA
BERKELEY, CALIFORNIA 94720